FAILURE PREDICTION OF HYDROFORMING ALUMINUM TUBULAR BLANKS

WANG GUO DONG

M.Phil

The Hong Kong Polytechnic University

2014

The Hong Kong Polytechnic University

Department of Industrial and Systems Engineering

FAILURE PREDICTION OF HYDROFORMING ALUMINUM TUBULAR BLANKS

WANG GUO DONG

A thesis submitted in partial fulfillment of the requirements for the degree of Master of Philosophy

October 2011

Certificate of Originality

I hereby declare that this thesis is my own work and that, to the best of my knowledge and belief, it reproduces no material previously published or written, nor material that has been accepted for the award of any other degree or diploma, except where due acknowledgment has been made in the text.

_____ (Signed)

___WANG GUO DONG_____ (Name of student)

Abstract

Aiming for weight and product cost reduction as well as structure enhancement, different industries have been embarking on the development of new manufacturing processes and materials to produce different lightweight components and structures. The applications of lightweight aluminum tubular components / structures have been under development for many years. The industry's increasing requirements for the utilization of aluminum tubes in hydroforming processes indicate the industry's demands for lightweight metals, low energy consumption and effective methods for reducing the whole weight of components. However, the production of extremely thin and economical aluminum alloy tubes is still a challenging task. The formability of aluminum tubes in the hydroforming process is an important factor and was thus the focus of this study to offer an effective evaluation method for predicting the failure of alloy tubes.

The objective of this study was to develop a failure criterion to predict the failure of hydroforming of aluminum tubular blanks. This was achieved by developing a testing method for the tube formability and a new damage-based failure criterion for the tubular component under investigation, as well as the fracture behavior of aluminum tubular

blanks during the hydroforming process. The aluminum seam welded alloy tubes AA6063 were selected as the specimens in this study. An experimental platform for the hydroforming process was utilized in the study to obtain both material properties and damage parameters. A new analytic method in deriving damage rule has been proposed as a result of the study. Together with the experiment, a damage-coupled shear criterion was developed for the failure prediction of aluminum tubes in the hydroforming process. The criterion was computed using FORTRAN codes and compared to the experimental results and two other results obtained from published articles. The damage-coupled constitutive and failure models were implemented in a finite element analysis and then validated by the experimental results in order to establish a reliable failure prediction method for hydroforming aluminum tubular blanks. With the aid of the predictive capability of a damage-based material and failure models coded in a finite element package, new insights into the material failure behaviors in the hydroforming operation have been realized. The establishment of the predictive method will enable design and process engineers to produce high-quality tubular structures/components at a considerably reduced cost and weight.

Acknowledgment

First of all, I would like to express my thanks to The Hong Kong Polytechnic University for providing research funding to support this project. The work described in this report was fully supported by a grant from RPL1.

My deepest gratitude goes to my supervisor, Dr. L. C. Chan, for his continuous encouragement and guidance during this study. Sincere appreciation also goes to my co-supervisors, Prof. T. C. Lee and Prof. C. L. Chow, for their invaluable advices and suggestions in carrying out the research.

Special thanks are extended to Dr. L. Wang, Dr. C. H. Cheng, Dr. TF Kong, Miss C.P. Lai, Dr. J. Lin and Mr. W. Chen, and all technicians and colleagues in Net Shape Manufacturing Technology Unit and the Department of Industrial and Systems Engineering for their great assistance and valuable advice in the study.

List of Publications

A. Journal papers

G. D. Wang and L. C. Chan, (2011) Hydroformability of bulge forming light-weight tubes via micro-hardness dependence, Key Engineering Materials, Vol. 465, pp. 149-152

B. Conference papers

1. G. D. Wang and L. C. Chan, (2009) Experimental Study on the Relationship between Hardness and Principal Strain in Tube Hydroforming Process. Third Manufacturing Engineering Society International Conference: MESIC-09, pp. 633-637
2. G. D. Wang and L. C. Chan, (2009) Experimental study and simulation of hydroforming tubular stainless steel components, International Deep Drawing Research Group (IDDRG) (CD-Format)
3. G. D. Wang, L. C. Chan, J. Lin, (2009) Forming limit measurement in tube hydroforming: hardness distribution approach, The 2009 Joint ASCE-ASME-SES Conference on Mechanics and Materials (CD-Format)

Table of Contents

List of Figures

List of Tables

Nomenclature

α	Strain increment ratio
E	Young's modulus
$\overline{E}$	Effective Young's modulus
$C(Z)$	Increment of the plastic damage strengthening threshold
C_0	Initial plastic damage strengthening threshold
$\overline{C}^e$	Effective elastic modulus tensor
C^{ep}	Hardening modulus tensor
$\overline{C}^{ep}$	Effective hardening modulus tensor
D	Damage tensor
D_i	Principal damage values
D_{ij}	Damage tensor
e	Engineering strain
ε	Strain tensor
ϕ_d	Damage dissipative potential function
σ	Stress tensor
$\bar{\sigma}$	Effective stress tensor
σ_{eq}	Equivalent stress
$\bar{\sigma}_{eq}$	Effective equivalent stress

σ_u	Ultimate stress
σ_y	Yield stress
$M(D)$	Damage effective tensor
η	Damage hardening coefficient
p	Accumulative plastic strain
θ	Inclined angle of the localized band
R	Anisotropic plasticity parameter
T_0	Initial yield limit
$T(p)$	Strain hardening increment
W^e	Elastic strain energy
Y	Elastic strain energy release rate
Y_{eq}	Equivalent damage strain energy release rate
Z	Overall equivalent damage
τ_{cr}	Critical shear stress
n	Normal direction of the pure shear plane,
ψ	Angle between **n** and coordinate axis 2
θ	Angle between direction 1 and projection of **n** in plane 1-3
φ	Angle between direction 1 and projection of **n** in plane 2-3,
τ	Shear stress

σ_n	Normal stress on the plane
σ_{ij}	The components of the stress of material element with the selected coordinate directions
β	Strain ratio
$d\varepsilon_1$	Major strains
$d\varepsilon_2$	Minor strains
$Y(p)$	Strain hardening function
p	The equivalent plastic strain
σ_r	Radical stress
σ_θ	Hoop stress

Chapter 1 Introduction

In order to reduce size, weight and production cost as well as to produce stronger structures, different industries have been embarking on the development of new manufacturing processes and materials to produce varies lightweight components and structures (Lang et al. 2004a, Koc and Altan 2001, Lang et al. 2004b, Ray and Mac Donald 2005, Kang, Kang and Kim 2005). The applications of aluminum AA 6063 in industrial tubular components / structure shave been under development for many years (Kang et al. 2005, Subhash, Imaninejad and Loukus 2005). Obviously, to produce extremely thin and economical alloy tubes is a very difficult and challenging task.

Conventionally, In order to reduce the time and economic consumption prediction methods have been applied widely to analyze the failure of sheet and tube hydroforming. Failure theory based on forming limit diagram has been used in research. Numerical simulation methods on the hydroforming process and related failure have been investigated using various commercial finite element analysis (FEA) packages.

However, due to considerable differences hydrofoming process and conventional sheet metal forming process the conventional failure criteria for the normal sheet metal forming are considered unsatisfied in predicting the failure of hydroformed alloy sheets and tubes. Furthermore, the mechanical properties, such as stress-strain relation,

hardening rule, strain-rate sensitivity and flow stress also have some different features compared with sheet metals. As such, there is a practical need to carry out comprehensive studies on both the hydroforming process and the appropriate failure models for alloy Aluminum AA6063 tubes in hydroforming process. Relevant studies of the damage mechanics based theoretical analysis of AA 6063 tubular blanks and the related failure diagrams or hydroformability seem to be extraordinarily rare. Therefore, the study of hydroforming AA 6063 tubular blanks is one of the areas to be explored for the research and development of tubular components / structures in industry (Kang et al. 2005). Obviously, another potential research area is the development of process simulations and their predictive modeling techniques, which includes the formulation of constitutive equations and new effective failure prediction models, for hydroforming AA 6063 tubular blanks (Kang et al. 2005). Thus, this study is focused on these two critical areas.

1.1 Hydroforming process

Sheet metal forming has been a conventional manufacturing process since ancient when it existed in artisan workshops. In modern industry, it is also an important manufacture

technology which is widely used in automobile, aerospace and packaging industries. In the automotive industry, about one third of the weight of a vehicle comes from sheet metals.

The advantage of sheet metal forming material is the lightweight and the low consumption. The sheet products can be used to reduce the overall weight of a vehicle and thus can obtain economical aims. Nowadays, the major types of sheet metal forming processes include the bending, deep drawing, combined bending and tension, and hydroforming (Vukota 2004).

The hydroforming process, which has been used widely since 1920 , utilizes mainly fluid pressure and hollow blank material to produce complex shaped parts such as exhaust system pipes , side rails, engine cradles, camshafts, crankshafts, differential casings and support panels, etc (Hill 2001, Kim and Kim 2002).

The hydroforming process as a developing technology can be divided into three stages of use based on its products (Asnafi and Skogsgårdh 2000).

(a) 1900-1950: steam boilers, musical instruments, artificial limbs. In this period, the basic process of the hydroforming was achieved and the related equipments was designed and produced in detail.

(b) 1950-1985: plumbing industry copper T fittings, branched bicycle frame joints.

(c) 1985-1990: auto industry, the various components in the automobile including the fore and rear bridge structures, the base frame, and some pipes were produced via hydroforming process.

The integration of these components meets the light requirement for reducing the whole weight of related products. At the same time the required processes for these products can also be reduced obviously.

In the 1990s, the hydroforming process became an important process that spread widely in the industry engineering and an important research topic for researchers in sheet metal forming fields.

With the coming financial and energy crisis, the need to lower energy consumption has become an important goal for the auto industry. An increasing acceptance and application of the hydroforming process in the automotive industry demands a full

understanding of the interactions between the elements of this process as well as their boundaries for a sound and defect-free component. An overall review of the hydroforming process, important aspects, and recent developments can be found in various publications (Kim and Kim 2002, Kulkarni et al. 2004, Graf and Hosford 1993).

In tube hydroforming process, a blank tube with a uniform shape is used to be hydroformed into a complex die cavity with a designed complex shape. The tube should be formed without any kind of failures such as bursting, folding, wrinkling or buckling. In order to attain this goal successfully, some measures and alterations need to be conducted during the design procedure and trials. These measures can provide useful information for alerting part design, and changing original components and the process design (Koc and Altan 2002).

The loading condition of tube hydroforming is a combination of axial feeding and internal pressure; any unsuitable parameters of these will lead to failure of products. If the axial feeding force is applied excessively at the beginning of the process, buckling may be generated. On the contrary, if the internal pressure is loaded excessively, bursting may occur. Meanwhile, if the axial feeding is insufficient to compensate the thinning at large expansion regions of the tube, the product wall may become

dis-uniform and may have less strength. Hence, after the material shape and size have being determined correctly, it is important to determine the failure and forming limits of the hydroforming process and the process parameters then can be designed within safety region to avoid the occurrence of these failure. (Koc and Altan 2002).

1.2 Failure prediction

Different unsuitable factors in the tube hydroforming process may lead to different types of tube failure. Instability modes, which limit the extent of formability in the THF process, occur when the stress and strain state in one part reach a critical level such that equilibrium cannot be sustained any longer between the applied external forces and the internal resistance of the material (i.e. strength). There are certain limitations on the deformation degree of the material, and if these limitations are exceeded, product defects may form in certain parts or certain areas. Depending on the defect type observed, the failure types, known as instability modes are usually grouped as (a) Wrinkling, (b) Buck-ling and (c) Bursting (Necking, Fracture) which shown in Fig. 1.1.

The buckling and wrinkling which can be regarded as a local buckling come from an unsuitable combination of excessive axial feed and less internal pressure, and both of

them may be modified with high internal pressure in some cases. At the same time, the bursting failure is an un-repairable failure. Consequently, the research on the FLD is also an important task in hydroforming process research.

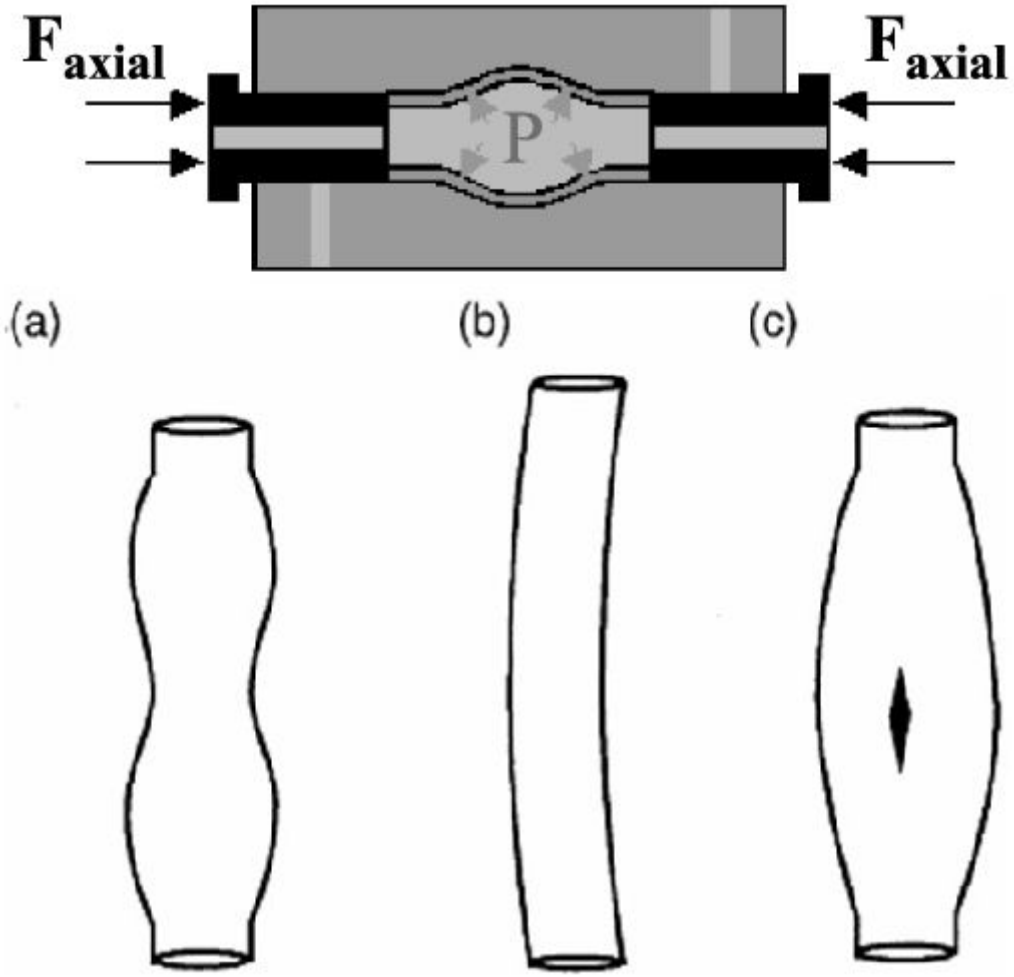

Fig. 1.1 Common failure modes that limit the THF process

(a) Wrinkling; (b) Buckling; (c) Bursting

(Kulkarni et al. 2004, Guan, Y., F. Pourboghrat et al.2006)

Bursting is a popular failure mode produced by excessive tensile forces. The busting is initialized from localized necking; when the localized necking starts the deformation of the components will be concentrated in the localized necking area and will lead to the eventual fracture of the component. (Kang 1990, Koc and Altan 2002) (Koc and Altan 2002). Unlike wrinkling and buckling which are uniform failures of the component and sometime can even be used in the process to obtain more material feeding (Lang et al. 2004c), bursting always leads to the complete failure of components. Thus the failure prediction on localized necking has been an important research focus for many researchers (Keeler 1963, Graf and Hosford 1993, Bressan and Williams 1983b, Marciniak 1967, Chow and Yang 2002, Chan, Lin and Wang 2010).

1.3 Objectives

The primary objective of this study is to develop a failure criterion to predict the failure of hydroforming of aluminum AA 6063 tubular blanks. This can be achieved by developing a new damage-based failure criterion for the AA 6063 tubes under investigation, as well as the fracture behavior of aluminum tubular blanks under hydroforming (HF). The proposed damage-coupled failure models were computed and then compared to the experimental result in order to establish a more reliable prediction

method of hydroforming failure diagrams (HFD) for aluminum AA 6063 tubular blanks .

The specific tasks of the project were:

1. Development of shear failure criterion to be capable of determining the failure behavior of specific material under a negative strain ratio process.
2. Formulation of a damage coupled shear failure criterion for hydroforming Aluminum tubular blanks based on the emerging theory of damage mechanics.
3. Experimental acquisition of specific material such as the construction of failure diagrams, measurement of the hydroformability and damage parameters of the base material.
4. Prediction of failure diagrams based on the proposed damage-coupled constitutive and failure models
5. Validation of the damage-based failure model by means of the measured and predicted failure diagrams.

In order to achieve the objectives, the work was divided into three categories: theoretical work, experiments, and numerical simulations. The theoretical work includes a development of damage coupled shear criterion. An anisotropic damage mechanics

model was used to couple with a newly proposed criterion to obtain a new localized necking criterion. The numerical method was used to calculate the predicted failure diagram of the components. The experiments were divided into two categories: those from which the material properties and various parameters of the failure criterion could be obtained; and those from which the hydroformability of components in the hydroforming could be obtained. The whole process can be summarized in the following chart which is shown in Fig. 1.2.

This study aimed to develop a reliable damage-coupled localized necking failure criterion. The aim was to realize new insights into the material behaviors in the hydroforming operation with the aid of the predictive capability of a damage-based material and failure models coded in a finite element package. The establishment of an accurate predictive method could enable design and process engineers to produce high-quality AA 6063 tubular structures/components at a considerably reduced cost and weight, which was expected to benefit various related industries.

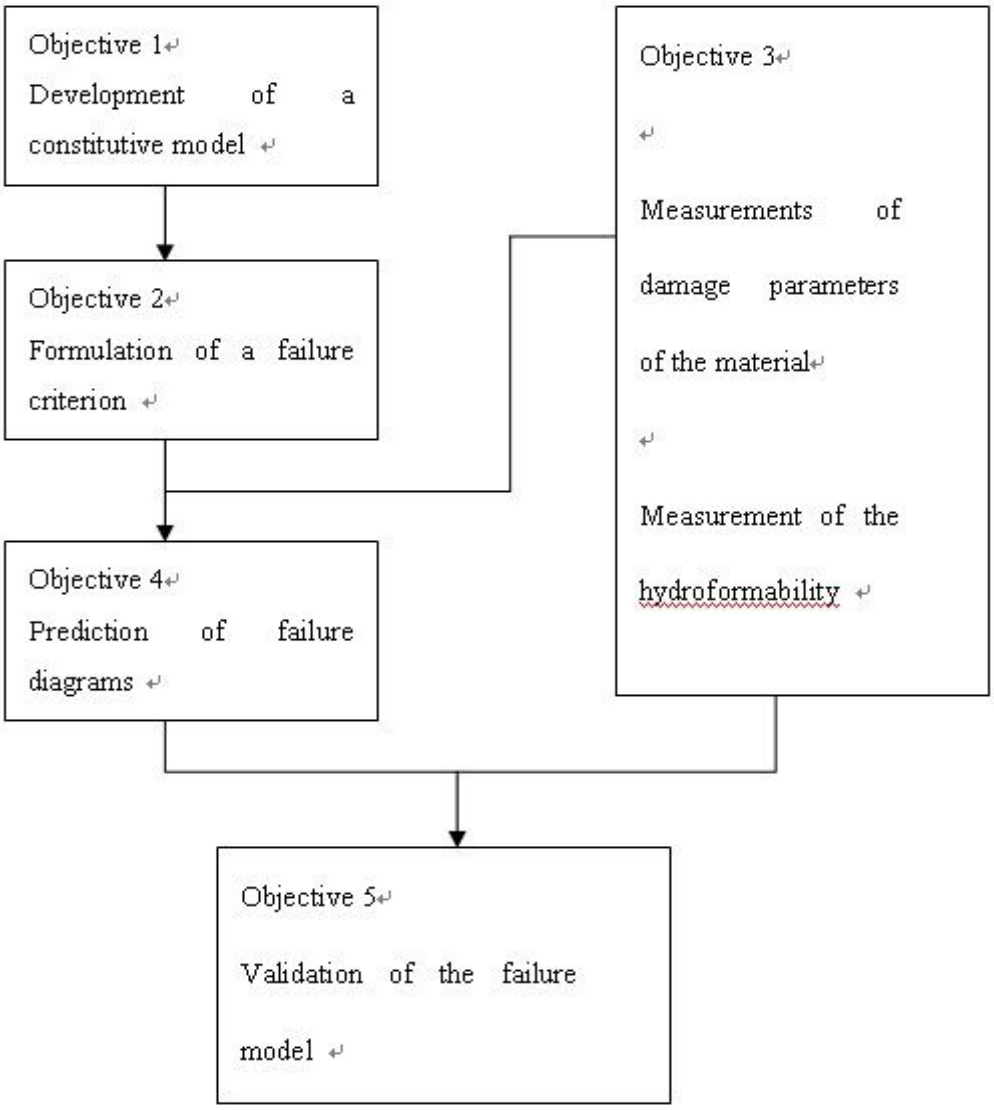

Fig. 1.2 Objectives and work steps of the study.

1.4 Outline of the thesis

This thesis is composed of seven chapters. Chapter 1 shows the background, objectives, significance and contributions of the study. Chapter 2 describes details of previous studies, including hydroforming, forming limit analysis in sheet metal forming

especially in hydroforming forming process, shear failure criterion, damage mechanics and its application in FLD prediction. The objectives of the study are also identified in this chapter. The theoretical development of this study is described in Chapter 3. Further descriptions of the improvement of shear failure criterion as well damage coupled failure model are introduced. The numerical simulation of the study is introduced in Chapter 4. The overall experimental plan and details of the methodology are illustrated in Chapter 5. Some experiment results are presented and discussed in Chapter 6. Chapters 7 and 8 describe the conclusions and future work respectively. Finally, correlative references and appendices are attached at the end of this thesis.

Chapter 2 Literature Review

In this chapter, a brief literature review about the research topic will be presented. In Section 2.1, the research on the formability during sheet metal forming process will be introduced. Then, the problems of the research on hydroforming will also be noted. In Section 2.2, the research on the damage mechanics will be introduced. A comprehensive understanding of the development of the formability research on the hydroforming process based on damage mechanics can be studied. Finally, in Section 2.3 the problem investigated in the present study will be introduced.

2.1 Formability analysis in sheet metal forming and hydroforming process

In sheet metal forming process, a stretchable limitation is existed in sheet metal. If it is exceeded, the material and the components will be ruptured. The formability of sheet metals in metal forming process is the key to design an optimum manufacturing process. Apart from the flow curve and plastic anisotropy, the formability of a material includes the capability to undergo plastic deformation to a given shape without defects.

Sheet metal formability has become a research topic since the end of nineteenth century, due to the rapid development of the sheet metal forming technology (Z. Marciniak 2002). From then on varied methods for evaluating sheet metal formability have been developed. These methods can be subdivided into four classes:

1. Simulating tests.
2. Methods based on mechanical tests.
3. Method of the limiting dome height.
4. Methods based on forming limit diagrams.

The research methods of sheet metal formability are shown in Fig. 2.1.

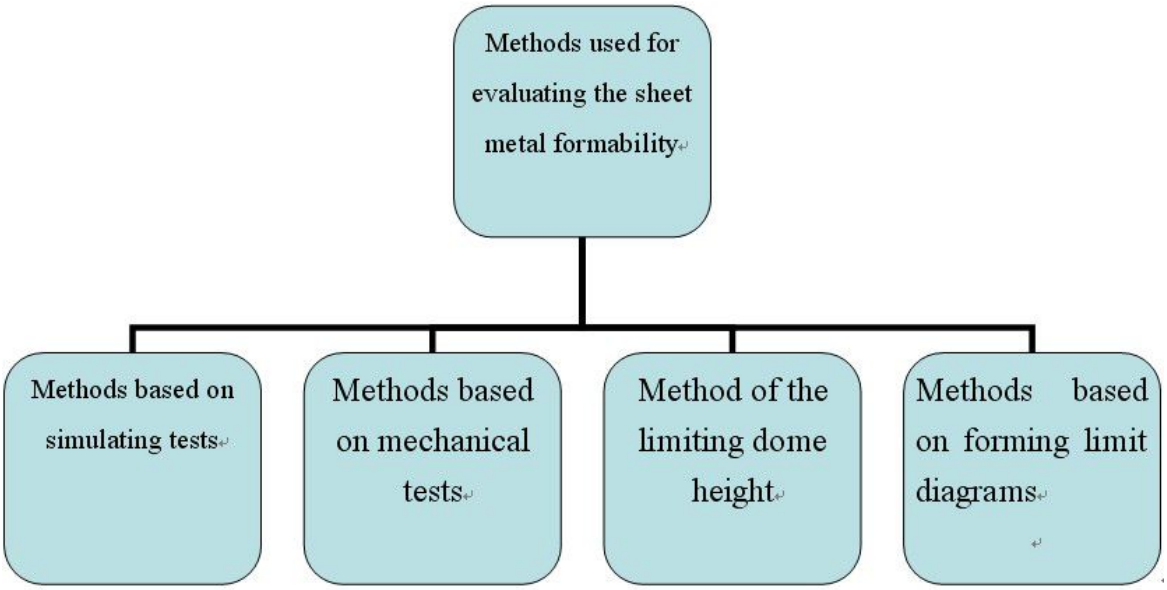

Fig. 2.1 Sheet metal formability research methods

The forming limit diagram is also named the K-G diagram, dedicated to the contribution of two pioneer researchers, Keeler and Goodwin. It has been said by some researchers that Keeler and Goodwin took formability research from an art into a science (Lu 1994).

The maximum values of the principal strains ε_1 and ε_2 can be determined by measuring the strains at the fracture region on the sheet components covered with certain shape grids. Based on the observations of Gensamer (Gemeamer 1946), the local deformation has to be considered instead of using global indices. During the sheet metal forming process the initial circles of the grid become ellipses. Keeler plotted the maximum principal strain against the minimum principal strain obtained from such ellipses at fracture of parts after biaxial stretching ($\varepsilon_1 \geq 0$, $\varepsilon_2 \geq 0$). In this way, a curve limiting the tolerable range can be obtained (Keeler 1965). Later, Goodwin performed similar work for the tension/compression domain ($\varepsilon_1 \geq 0$, $\varepsilon_2 \leq 0$) by using different mechanical tests (Goodwin 1968).

The diagrams of Keeler and Goodwin together give the values of ε_1 and ε_2 at fracture. This is currently called the forming limit diagram (FLD). For numerous materials the critical area between the domains has been detected both by means of laboratory tests and by the forming of industrial components. These measurements have been conducted

for various materials. The excellent correlation of the results is a proof that the forming limits in sheet metal forming can be evaluated very well by determining the forming limit curve in laboratory tests. How eve, the forming limit test on different material should be conducted in standard condition and consume much time. Meanwhile some factors such as grid sizes and shapes and grids measure method always influence the results greatly. In order to reduce the time consumption on tests and avoid test errors occurred in these tests, various theoretical models have been developed for the calculation of forming limit diagrams. The diffuse necking and the localized necking are explained by these theories, separately from different angles.

The Swift model addresses the problem of plastic instability in uniaxial tension. In the case of ductile materials, two domains may be distinguished in the region of plastic straining. In the first domain the hardening influence on the traction force is stronger than the influence of the cross-section reduction. This is called “domain of stable plastic strain”, and is characterized by the fact that an increase of the traction force is needed in order to obtain an additional deformation of the specimen. In the second domain, material hardening cannot compensate for the decrease of the traction force due to the reduction of the specimen’s cross-section. This is the so-called “domain of unstable

plastic straining", characterized by a decrease of the traction force, although the stress continues to increase.

Swift used Considere's criterion (Considere 1885) to determine the limit strains in biaxial tension (Swift 1952). He analysed a sheet element by using Considere's criterion for two perpendicular directions. The evaluation of limit strain can be achieved by using different yield functions. The limit strain can be functions of the loading ratio α and the mathematical parameters of the material (hardening coefficient n, anisotropy coefficient r, strain-rate sensitivity m etc.).

In the case of uniaxial tension, the localized necking develops along one direction, which is inclined with respect to the loading direction. Hill assumed that the necking direction is coincident with the direction of zero-elongation. The strain in the localized necking is only because of the material thinning (Hill 1952b). Hill's theory can be used to predict the failure diagram on the left side of FLD (Fig. 2.2), but it cannot be used to predict the localized necking which occurred in a sheet metal subjected to positive biaxial stretching.

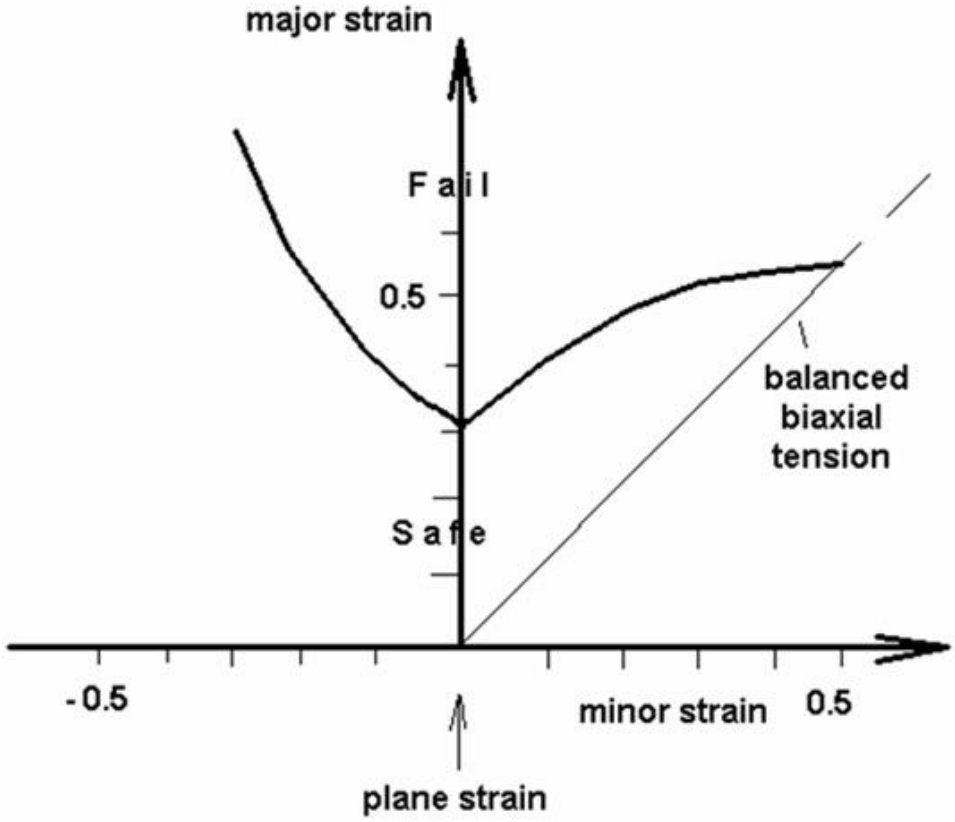

Fig. 2.2. FLC curve of steel (Lu 1994)

Marciniak proposed a theory on the initiation of localized necking on the basis of the experimental investigations concerning the strain localization of some specimens subjected to hydraulic bulging or punch stretching. The proposed theory takes a geometrical or structural non-homogeneity of the material as the initiation points of localized necking (Marciniak 1967). Such non-homogeneity may indicated by a thickness variation on the metal sheet.

The analysis of the necking process has been conducted under the assumption that the defect of the material will form a geometrical non-homogeneity in a certain area, which leads to less thickness value in the region. This defect may be brought from the technological procedure used to obtain the sheet metal. The gradual variations of the thickness are then assumed as a sudden variation, with which the calculation can be simplified.

By varying the strain ratio, different points on the FLD are obtained. By scrolling the range, the FLD for biaxial tension is obtained. In this range the orientation of the geometrical non-homogeneity, with respect to the principal directions, is assumed to be the same during the entire forming process. M-K theory can be used to predict the right side of the FLDs, but the initial geometric non-uniformity of sheet metal which is needed in the model should be selected arbitrary, and the prediction results are sensitive to such an arbitrary selection.

The prediction of forming limits in tubular hydroforming is still a developing field of study. In an early study, experimental research and numerical analysis were conducted by Larsson et al. (Bontcheva 1994) on the bulging of aluminum alloy and pure copper tubes. The localized necking of the tubular samples was detected to occur at a point

where the pressure value is the maximum pressure. Several studies have been carried out in order to analytically predict the bursting and wrinkling of tubes (Benallal and Comi 1996, Schreyer and Neilsen 1996). The roles of plastic anisotropy and strain hardening on burst pressure were examined, assuming that the tube experienced proportional strain histories.

Free hydroforming, which has no contact with external die, was performed by Asnafi and Skogsgardh (Schreyer and Neilsen 1996), and the results of their experiment were compared with the finite element analysis. Their research concluded that the strain path of the material during the hydroforming is non-proportional. However, the exact strain paths of the tubes were not recorded in their experiment. The relationships between the strain history and the tube failure still have not been identified.

The above issues were addressed in some more recent work by Kulkarni et al. (Lemaitre 2000). They performed free hydroforming experiments using aluminum alloy tubes. A novel feature of their work was that special purpose (post-yield) strain gauges were employed to record continuously the strain histories experienced by the tubes at the mid-length. The limit strains corresponding to failure by localized necking of the tube wall were determined from circle grids etched on the surface of the tube specimens.

The work conducted by Kulkarni et al showed that the strain paths in some complex shaped tubular hydroforming are extremely non-proportional. At the same time, they made a significant contribution with their finding that not only the forming limit but also the maximum pressure the tubular sheet can be endured. In this connection, it must be mentioned that the influence of strain paths on sheet FLCs has also been demonstrated in other experimental studies such as Ref. (Kulkarni et al. 2004). However, despite this path dependence, strain-based FLCs are used in assessing the material formability, optimizing material conditions and process parameters for both sheet and tube components.

Although a considerable amount of work has been done on the formability of tubes in the hydroforming process, a comprehensive investigation of the special loading condition of hydroforming and its influence on hydroformability has not yet been undertaken.

The observations introduced in Refs.(Graf and Hosford 1993, Lu 1994) investigated the roles of strain paths; however it was limited to combined fluid pressure with stroke. The effect of other types of loading conditions, such as fluid volume flow rate in conjunction with axial end displacement or force, on the formability of tubes has not been examined.

It is important to address this issue because it will enable better design of dies and other associated tools. Also, the nature of stress and strain histories experienced by the tubes and their influence on the operative failure processes such as localized necking or wrinkling can be ascertained..

In tube hydroforming, circular components are bulged or formed from tubular blanks with internal pressure and simultaneous axial loading. Thus the tube can be fed into the deformation zone during the bulge operation, allowing more expansion and less thinning so that the parts with the desired specifications can be formed without any defects such as wrinkling, bulking, and bursting. The modes of the tubes' hydroformability are the same as the sheet metal formability, but the unique load conditions of the hydroforming process create some differences between them.

In the hydroforming process, the stress states are complicated and cannot be categorized as tensile stress (koc 1999). At the same time, the thickness variation is also a considerable factor that will influence the hydroformability, so the 3-D stress state should be considered as some occasions during the process. Such a complicated stress state makes the plane stress assumption unsuitable in some cases, and the methods of analysis should then be different. The main failure mode in the present study is

localized necking which comes from thinning of the material. Plane stress is assumed in the related analyze.

Kulkarni et al. performed free hydroforming experiments using aluminum alloy tubes (Kulkarni et al. 2004). They demonstrated from these experiments that the strain paths corresponding to the particular type of loading conditions employed in their work were strongly non-proportional. Further, they showed that the nature of strain path can have a profound effect on hydroformability.

It has been noted by many researchers that a systematic study of the influence of loading conditions on the mechanics of tube hydroforming, as well as failure brought about by localized necking, must be undertaken. There also needs to be an examination of the effects of some other types of load conditions which exist in the hydroforming process on the hydroformability of tubes, such as friction in the process and evaluation of lubricants, preforming of tubes, and fluid volume flow rate in conjunction with axial end displacement or force.

Based on the facts mentioned above, Nader and Anders (2003) concluded that only the Forming Limit Curve determined by hydroforming (hydroformability) can be used as a

completely reliable aid in component and process design (Asnafi and Skogsgårdh 2000).

2.2 Shear failure criterion

The shear failure criterion is based on the mechanism of plastic slip. The plastic deformation in metal is considered initiated in certain slip bands, and generated from shear plane on these preferred slip systems. Luder's lines, which result from the development of intense shear bands in the direction of pure shear, can be the evidence of the slips (Bressan and Williams 1983b). Some fracture experimental observations on sheet metal have shown that the fracture plane is located near the maximum shear plane (Bressan and Williams 1983b, Keeler 1963, Painter 1974). Based on the above facts, the shear criterion has been considered as a useful localised necking criterion (Bressan and Williams 1983b).

The shear criterion was first proposed by Bressan and Williams (1983) and has usually been named as the Bressan-Williams criterion (BW). There are two advantages of this criterion. First, it can be solved analytically with a simple expression, and can be used to obtain acceptable results with reasonable precision. Second, there are no proportional

assumptions used in its derivation, which make it available in studying complex loading path process. Based on above discussion it is utilized in present study to research the hydroformability of AA6063 tubes, which are processed mainly under nonproportional loading path.

However, the aim of the original shear criterion was to investigate the RHS of FLDs, which cannot be predicted using Hill's criterion. In order to extend its utilization, different efforts have been made by later researchers. An combination criterion was proposed by Alsos, Hopperstad, Tornqvist and Amdahl (Alsos et al. 2008). The criterion which they referred to as the BWH instability criterion used Hill's local necking criterion to predict LHS and used shear criterion to predict RHS. Another achievement was proposed by Lin, Chan and Wang (Chan et al. 2010). The criterion were extended to be utilized in both the RHS and LHS, based on the original assumption proposed by Bressan and Williams. However, there were some mistakes made in determining the angles of the shear plane and these led to some incorrect results.

2.3 Damage mechanics and its application in FLD prediction

Damage in solid materials can be used to describe the creation and growth of different defects in a medium, and such a medium is considered as continuous on a large scale. The concept of damage mechanics was introduced by Kachanov in 1958 . He proposed a scalar damage variable to describe the fact of the non-homogeneity of materials. This material non-homogeneity exists in many engineering materials. The forms of such non-homogeneity include inclusions, micro-voids, and micro-cracks.

In the general, material non-homogeneity is studied within two frameworks, one is the continuum damage mechanics (CDM, Hult use this term first in 1972), and another one is the meso-scale damage mechanics (MDM). When material non-homogeneity is considered by accounting the average effect of all micro-defects mentioned above, such a method is named CDM. By calibrating the variation of apparent mechanical properties such as Young's module and the Poisson ratio, the damage factor can be calculated and used to describe the degradation of the material (Leckie and Hayhurst, 1974; Lemaitre and Chaboche, 1974; Hult, 1979; Horii and Nemat-Nasser, 1983; Murakami, 1983; Krajcinovic, 1985; Lemaitre, 1985; Krajcinovic et al., 1991; Lundmark and Varna, 2005). In MDM, researchers take account of the nucleation, growth, and coalescence process of all the individual microvoids, microcracks and inclusions.

In the 1970s the MDM was used by several researchers to analysis the forming limit of sheet metal. Gurson's model (Gurson 1977) has been adopted by Needleman and Triantafyllidis to describe the growth of micro defects in the ductile metals (Needleman and Triantafyllidis 1978, Gurson 1977). The analytic method describing the variation and evolution of the micro voids have made Gurson's model a classic theory in MDM research.

The thickness ratio of the M-K model is regarded as an index to describe the void concentration ratio between the localized necking area and the uniform deformation area. The FLDs are calculated with different initial void concentration and various strain hardening exponents. The research on this model has demonstrated that the void growth and the localized necking initiation come into being at nearly the same time, which shows that the micro void concentration has a direct relationship with the localized necking, and the void concentration can be a reasonable interpretation for the localized necking. Chu et al. calculated the sheet metal forming with the microstructrual features, based on Gurson's model (C.C 1984). The result they obtained showed a significant effect of the void nucleation on the forming limit in the plane stretching state.

Many other efforts have also been performed in the prediction of FLDs. Kang et al. (1990) used the Gurson model combined with the M-K model to predict FLD, (Kang, Kim and Kobayashi, 1990 and Doege et al. 1995) combined Hill's equivalent stress model with Gurson's yield model, to calculate the anisotropy of material damage (Doege, Eldsoki and Seibert 1995). Jeong and Pan (1995) used Gurson's model combined with Coulomb's to yield a modified yield criterion which can be used to examine the toughness of rubber-modified plastics under large plastic condition (Jeong and Pan 1995). The related numerical results showed that the strain softening and the moderate amount of void volume non-homogeneity is the main factor on the localized necking. Such a result is valid for the general condition of sheet metals.

Another study was done by Parmar and Mellor, who observed the void increase via the density changes in a biaxial tension condition (Parmar and Mellor, 1980). They found that the changes of density were related to the amount of plastic deformation, and not connected with the applied strain ratio.

The damage in sheet metal forming was observed with the SEM and TEM by Schmitt and Jalinier in 1982. Their results showed that the damage in the cold work was initiated by de-cohesion at the interface of the second phase particles and the base

material or the rupture of the particles. The damage was described by the variation of material density. The relationship between the internal damage and the defects could then be established, and the simulated FLD was found to be comparable with the experimental results.

The Cocks-Ashby model was also used in the 1990s to investigate the growth of spherical voids in a rate dependent plastic material (Horstemeyer et al., 2000, Ashby, Shea and Howard, 1980, Horstemeyer, 1994,Beaudoin et al., 1994, Hu, Chandra and Huang, 1993) The void fraction was also taken as a damage scalar. The results showed that such work can give a more accurate estimate of FLDs.

Since the 1990s, some researchers have begun to use CDM to investigate the FLD in the sheet metal forming process. To study different material properties, different damage models include isotropic and anisotropic are considered to be appropriate in describing the damage existed in these materials.

In the early work conducted by Bontcheva et al. (1994), Beanllal et al. (1996), and Schreyer et al. (1996), the isotropic damage model is used with scalar damage factors. The localization analysis was studied theoretically based on these damage models. The

microcrack closure and reopening effect in the isotropic damage model were considered by Ekh et al., from which the FLD was calculated. Their results showed little influence on the critical localized necking angle by the damage evolution. (Ekh and Runesson, 2000). Some later findings were brought forth by Voyiadjis et al., who used the gradient theory to modify the damage model and performed the numerical simulation method to study localized necking (Abu Al-Rub and Voyiadjis, 2006). A series critical damage values about the initiation of localized necking were obtained by Lemaitre et al. The isotropic damage critical value was about 1.0 and the anisotropic damage critical value was about 0.5 (Lemaitre, 2000, Lemaitre, 1985). These critical values were found to be somewhat higher than the experimental results.

An anisotropic damage model was developed to indicate the anisotropic property of damage exist in materials by using the proposed second-order tensor **D** (Chow, C. L.. and Wang, J. 1987a, 1987b). The anisotropic damage model is a rapidly developed theory which is used to investigate the FLDs in the hydroforming process. In the following, the main theory of damage mechanics, as it is used to study the forming limit research, will be introduced.

The effective stress is defined by using a proposed damage effective tensor **M(D)** as follows

$$\bar{\sigma} = M(D) : \sigma \tag{2.2}$$

Where, **M**(**D**) is defined within the principal coordinate system as (Chow, C. L.. and Wang, J. 1987a, 1987b ,Chow 1989)

M(**D**)=

$$\begin{bmatrix} \frac{1}{1-D_1} & 0 & 0 & 0 & 0 & 0 \\ 0 & \frac{1}{1-D_2} & 0 & 0 & 0 & 0 \\ 0 & 0 & \frac{1}{1-D_3} & 0 & 0 & 0 \\ 0 & 0 & 0 & \frac{1}{\sqrt{(1-D_2)(1-D_3)}} & 0 & 0 \\ 0 & 0 & 0 & 0 & \frac{1}{\sqrt{(1-D_3)(1-D_1)}} & 0 \\ 0 & 0 & 0 & 0 & 0 & \frac{1}{\sqrt{(1-D_1)(1-D_2)}} \end{bmatrix} \tag{2.3}$$

where D_i (i=1, 2, 3) are principal damage values.

When the principal directions is not coincide with stress state, coordinate transformation is required (Chow, C. L.. and Wang, J. 1987a, 1987b ,Chow 1989).

The effective elastic modulus tensor $\bar{C}^{e}$ is derived based on the hypothesis of elastic energy equivalence as follows (Chow 1989)

$$\bar{C}^{e-1} = M^{T}(D) : C^{e-1} : M(D) \tag{2.4}$$

where C^{e} is the elastic modulus tensor.

The damage evolution equation is,

$$\dot{D} = \frac{\partial \phi_{d}}{\partial Y} \tag{2.5}$$

Where ϕ_{d} is the damage dissipative potential function and Y is the elastic strain energy release rate.

The damage elastic strain energy release rate is expressed as:

$$\mathbf{Y} = \frac{\partial W^{e}(\sigma, D)}{\partial D} \tag{2.6}$$

Where W^{e} is elastic strain energy.

The equivalent damage strain energy release rate Y_{eq} is defined as:

$$Y_{eq} = (\frac{1}{2} Y^{T} : N : Y)^{1/2} \tag{2.7}$$

where, N is a fourth-order isotropic tensor used to describe the characteristics of damage surface as follows.

$$N_{ijkl} = \eta \delta_{ik} \delta_{jl} + \frac{1}{2}(1-\eta)(\delta_{ik}\delta_{jl} + \delta_{il}\delta_{jk}) \tag{2.8}$$

Where, η is the damage hardening coefficient.

The damage surface is defined as

$$F_d = Y_{eq} - [C_0 - C(Z)] = 0 \tag{2.9}$$

Where, Z is the overall equivalent damage. C_0 is the initial plastic damage strengthening threshold and C(Z) is the threshold increment.

The damage evolution equation is written as (Chow, C. L.. and Wang, J. 1987a, 1987b ,Chow 1989)

$$\dot{D} = \dot{\lambda}_d \frac{\partial F_d}{\partial Y} \tag{2.10}$$

Where λ_d is a parameter. The damage evolution equations are derived as (Chow, C. L.. and Wang, J. 1987a, 1987b)

$$\dot{Z} = \alpha \frac{\partial F_d}{\partial \sigma^T} : \dot{\sigma} \tag{2.11}$$

And

$$\dot{D} = \alpha \frac{\partial F_d}{\partial \sigma^T} : \dot{\sigma} \frac{\partial F_d}{\partial (-Y)} \tag{2.12}$$

where

$$\alpha = \left[\frac{\partial C}{\partial Z} - \frac{\partial F_d}{\partial D^T} : \frac{\partial F_d}{\partial (-Y)} \right]^{-1} = \left[\frac{\partial C}{\partial Z} - \frac{\partial F_d}{\partial (-Y^T)} : \frac{\partial (-Y^T)}{\partial D^T} : \frac{\partial F_d}{\partial (-Y)} \right]^{-1} \tag{2.13}$$

The elastic strain energy release rate **Y** is derived by Chow and Lu (Chow 1989), Chen and Chow (Chen, X.F. and Chow, C.L. 1995), and Jie (2003),

The plastic yield surface with respect to effective equivalent stress is as follows

$$F_P(\bar{\sigma}, p) = \bar{\sigma}_{eq} - [T_0 + T(p)] = 0 \tag{2.14}$$

Where T_0 is the initial yield limit and $T(p)$ is the strain-hardening increment; p is the accumulative plastic strain..

The constitutive equation of material when using anisotropic damage theory can be expressed in a rate form as follows (Wang and Chow, 1990)

$$\dot{\sigma} = \bar{C}^{ep} : \dot{\varepsilon} \tag{2.15}$$

Where $\bar{C}^{ep}$ is effective hardening modulus tensor. It can be expressed as (Jie, 2003

$$\bar{C}^{ep} = M^{-1} : A^{-1} : C^{ep} : M^{-1} \tag{2.16}$$

Where,

$$A = I + \alpha \left\{ \frac{\partial M}{\partial D^T} : \frac{\partial F_d}{\partial (-Y)} : M^{-1} + \left[C^{ep} : M^{-1} : \frac{\partial M}{\partial D^T} : \frac{\partial F_d}{\partial (-Y)} \right] : C^{e-1} \right\} : \sigma \frac{\partial F_d}{\partial \sigma^T} \tag{2.17}$$

Where C^{ep} is the hardening modulus tensor as follows,

$$C^{ep} = C^e - \beta (C^e : \frac{\partial F_p}{\partial \bar{\sigma}}) : (\frac{\partial F_p}{\partial \bar{\sigma}}^T : C^e) \tag{2.18}$$

Where

$$\beta = \left(\frac{\partial T}{\partial p} + \frac{\partial F_P}{\partial \bar{\sigma}}^T : C^e : \frac{\partial F_p}{\partial \bar{\sigma}} \right)^{-1} \tag{2.19}$$

The anisotropic damage theory is first utilized to research the forming limit of VDIF steel and Al 6111-T4 sheets by Chow et al. (1996, 1997). The material is considered damage anisotropy as well as material orthotropy. The localized necking is indicated with two different damage criteria. Which are used to predict the forming limit strain in negative and positive strain ratio region of the FLDs respectively In the left hand side (LHS) of FLDs, the critical damage is assumed to be determined by a direction which is satisfied the condition as follows:

$$D_1 \cos^2 \theta + D_2 \sin^2 \theta = D_{1dcr} \tag{2.20}$$

Where θ is the inclined angle of the localized band (Figure 2.4), D_1 and D_2 is the maximum and intermediate principal damage values, respectively.

In the right hand side (RHS) of FLDs, the localized necking is determined by the principal damage deviators on the condition that,

$$D_1 - \frac{1}{3}(D_1 + D_2 + D_3) = D_{1dcr} \tag{2.21}$$

Where D_3 is the minimum principal damage value.

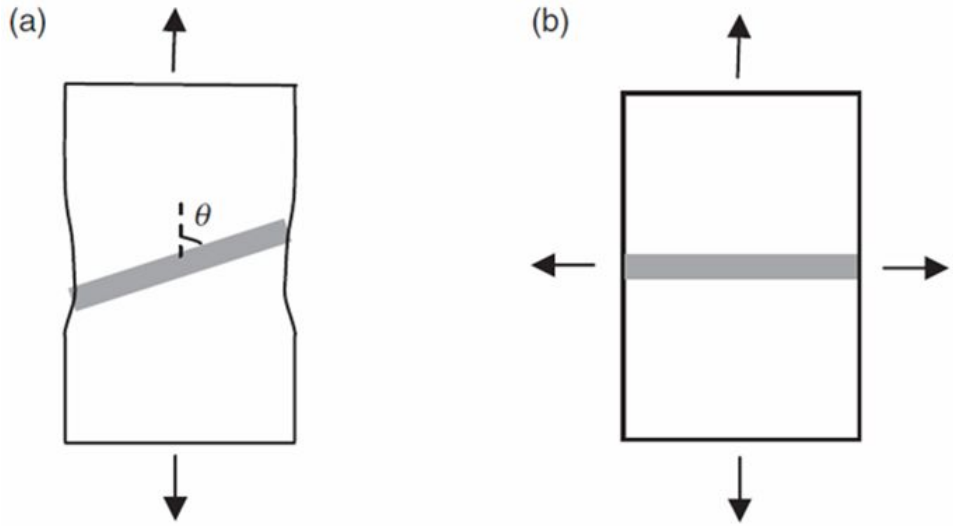

Fig. 2.4 Localized necking in sheet metals (Chow and Yang 2004)
(a) Uniaxial to plane strain(b) Biaxial tension

An accumulated damage instability criterion is adopted to determine the localized necking by later works of Chow et al. (Chow and Yang, 2004; Chow et al., 2001a, 2001b) as follows:

$$Z_1 = Z_{1c} \tag{2.22}$$

$$dZ_1 = dZ - \beta\zeta(dD_{11} + dD_{22} + dD_{33}) \tag{2.23}$$

Where Z_{1c} and ζ are material constants, Z is the overall equivalent damage; β is the strain increment ratio, i.e., $\beta = d\varepsilon_2 / d\varepsilon_1$

The critical value D_{1cr} used in equations (2.20) and (2.21), and Z_{1c} and ζ used in equation (2.23) are all regarded as intrinsic material constants. When using these forming limit criteria, these critical damage values should be determined accurately.

Generally the critical damage value is the ultimate point of damage evolution associated with the failure of a certain material. There is different critical damage values have been used in different damage theories. In Kachanov's creep damage model, the critical damage value is defined as 1. But most damage values cannot reach 1.0 when the metals rupture. Some critical values of metals corresponding to the fracture have been presented by Lemaitre Lemaitre, J. and J.L. Chaboche, (1990). These critical values extend across a wide range, from 0.85 (for pure copper) to 0.17 (for E24 steel). Further experimental efforts are called for to determine the critical damage value accurately.

Some theoretical studies have also been conducted to improve accuracy in determining material damage. The above anisotropic damage is based on the accurate measurement of the variation of Young's modulus. Loading and unloading experiments are usually used to obtain such variations of Young's modulus. The CDM theory is used to describe the influence of micro-voids and micro-defects that exist in the materials. Such micro structures will lead to the degrading of material properties. But in this experiment, the influence of the cyclic hardening will also influence the strain-stress relationship. Cyclic hardening will lead to an increase of Young's modulus (Chaboche, J.L., 1989). To decoupe the influence of cyclic hardening, the Chaboche law is used as follows:

$$\sigma = \sigma_y + Q(1 - \exp(-b\varepsilon_p)) + \frac{C}{\nu}(1 - \exp(-\nu\varepsilon_p)) \tag{2.24}$$

The alternative method of using damage mechanics to study failure criterion is to implement the damage effect into a general forming limit theory to obtain a localized necking criterion including damage (Jie M, and Chow C. L., 2009). In these theories, the critical damage is no longer a constant. The localized necking depends on the combination of damage variable, stress state and strain path. Due to the literature review suggestion that anisotropic damage theory is an effective method in dealing with the problem on formability study, because the material degradations which are existed in much materials can be taken into consideration. Moreover, it can be feasibly coupled with other formability criterion and from which both of damage and other mechanism in the material can be included in the analysis.

2.4 Problems formulation

The formability of tubes in the hydroforming process displays different features from sheet metal forming or sheet hydroforming. The complicated loading path makes it unsatisfactory to use popular forming limit theories. The shear failure criterion as a stress based localized necking criterion has no assumption on proportional loading. Therefore, it is more suitable to be used in studying the formability of tubes in hydroforming.

The degradation of metals during the loading condition has been observed by many researchers. Damage mechanics have been used in many engineering areas, such as building engineering, civil and structural engineering and mechanical engineering, so it is quite reasonable to take damage effect into consideration when using the shear failure criterion.

For the purpose of this study, the shear failure criterion will be modified and developed to be available in both RHS and LHS of the strain diagram. After this, the damage mechanics will be used to obtain the damage coupled shear failure criterion and corresponding predicted FLDs. Experiments will be conducted to obtain material properties, damage rules and the FLDs in the hydroforming process. The experimental results will be compared with the related theoretical predicted results to validate the proposed criterion.

Chapter 3 Development of the Damage Coupled Shear Criterion

3.1 Anisotropic damage constitution coupled shear criterion

On the view of the metal physics, slip bands will initiate on certain slips system which is referred as combinations of crystallographic plane and slipping directions. When the stretch of material reaches a criterion slip will arise. The shear criterion then had been proposed by in solving bursting failure of sheet metals (BRESSAN and WILLIAMS 1983) as introduced in chapter 2. In a recent publication, a extension work has been conducted by Chan, L. C. et al. How ever some mistake exist in their work, in the present study a modified dedution is performed to extend the criterion to be used in both RHS and LHS in strain diagram. After then, damage is taken into consideration. Finally, a damage coupled shear criterion is deduced.

The direction of the shear band and the maximum shear stress in a plane stress condition metal sheet are determined in section 3.1.1 and 3.1.2 in left side and right side of FLC individually, with which the shear failure criterion is obtained in both sides of FLC. After then, anisotropic damage theory will be used to take the degrade of the materials

during loading processes into consideration and the damage coupled shear criterion is obtained in section 3.1.3. The proposed criterion is calculated using numerical method and the predicted forming limit curve is obtained in section 3.3.

The maximum shear are always occurs in a specified shear band which is a plane with comparable small thickness located in a specific direction. Using vector **n** to define the normal direction of the pure shear plane, and the n_1, n_2, n_3 is the directional cosines of **n,** the maximum shear is

$$\tau = \sqrt{\left(\sigma_{11}n_1 + \sigma_{12}n_2 + \sigma_{13}n_3\right)^2 + \left(\sigma_{21}n_1 + \sigma_{22}n_2 + \sigma_{23}n_3\right)^2 + \left(\sigma_{31}n_1 + \sigma_{32}n_2 + \sigma_{33}n_3\right)^2 + {\sigma_n}^2} \tag{3.1}$$

Where σ_n is normal stress on the plane and can be expressed as

$$\sigma_n = \sigma_{11}{n_1}^2 + \sigma_{22}{n_2}^2 + \sigma_{33}{n_3}^2 + 2\sigma_{12}n_1n_2 + 2\sigma_{13}n_1n_3 + 2\sigma_{23}n_2n_3 \tag{3.2}$$

Where σ_{ij} in the equation are the components of the stress of material element with the selected coordinate directions.

In the present study the bursting of tubes in hydroforming process is found to be always connected with material thinning. The thickness to radius ratio of as received AA6063 tubes is 0.054, which will be decreased gradually during the process. As the thickness is

far smaller than radius, the plane stress condition can be taken as a basic assumption, then (3.1) becomes follows

$$\tau = \sqrt{{\sigma_{11}}^2\left({n_1}^2 - {n_1}^4\right) + {\sigma_{22}}^2\left({n_2}^2 - {n_2}^4\right) - 2\sigma_{11}\sigma_{22}n_1^2n_2^2} \tag{3.3}$$

In order to determine the maximum shear stress, the related directional cosines should be determined in advance. The related directions are shown in Fig. 3.1, the coordinate directions are defined as direction **1**, **2** and **3** separately, and two angles are used to determine the normal direction of the shear plane. Angles ψ is defined as the angle between **n** and direction **2**, meanwhile Angles θ is defined as the angle between direction **1** and the direction of the projection of n in plane **1-3**. Then, the directional cosines of normal direction along **1**, **2** and **3** can be obtained based on the defined angles

$$n_1 = \cos\theta \sin\psi \tag{3.4}$$

$$n_2 = \cos\psi \tag{3.5}$$

$$n_3 = \sin\theta \sin\psi \tag{3.6}$$

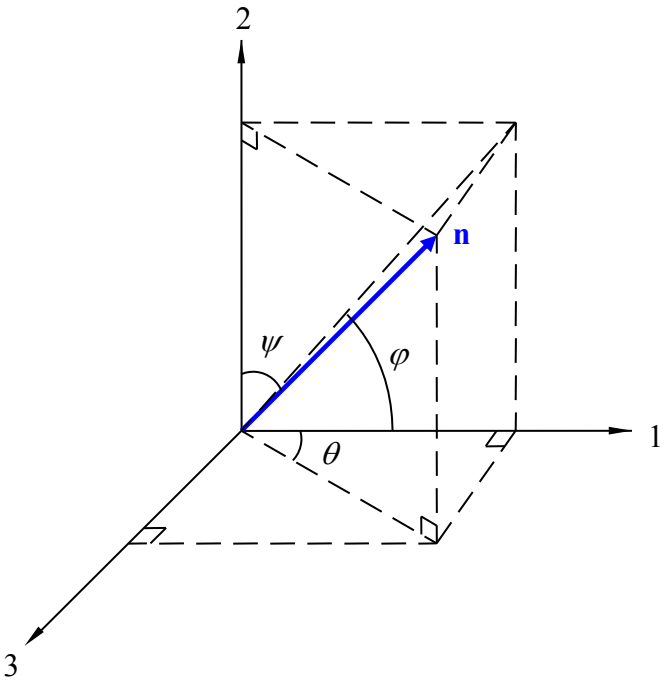

Fig. 3.1 The definition of three angles in 1-2-3 coordinate

When define angle φ as the angle between direction **1** and the direction of the projection of **n** in plane **2-3**, the following equations can be obtained based on the geometric relationships among ψ, θ and φ

$$tg\varphi = \frac{\cos\psi}{\sin\psi\cos\theta} = \frac{1}{tg\psi\cos\theta} \tag{3.7}$$

From (3.7) the angle ψ can be expressed using angle θ and angle φ

$$tg\psi = \frac{1}{tg\varphi\cos\theta} \tag{3.8}$$

From which the following is obtained

$$\frac{\sin^2\psi}{\cos^2\psi} = \frac{1}{tg^2\varphi\cos^2\theta} \tag{3.9}$$

The variables of angle ψ used in the (3.4)-(3.6) then can be expressed as follows

$$\sin\psi = \frac{1}{(1+tg^2\varphi\cos^2\theta)^{\frac{1}{2}}} \tag{3.10}$$

$$\cos\psi = \frac{tg\varphi\cos\theta}{(1+tg^2\varphi\cos^2\theta)^{\frac{1}{2}}} \tag{3.11}$$

Input the equations (3.10) and (3.11) into (3.4)-(3.6), the directional cosines of pure shear plane can be obtained with the independent variables directional angle θ and angle φ as follows

$$n_1 = \frac{\cos\theta}{\sqrt{1+tg^2\varphi\cos^2\theta}} \tag{3.12}$$

$$n_2 = \frac{tg\varphi\cos\theta}{\sqrt{1+tg^2\varphi\cos^2\theta}} \tag{3.13}$$

$$n_3 = \frac{\sin\theta}{\sqrt{1+tg^2\varphi\cos^2\theta}} \tag{3.14}$$

3.1.1 Determination of shear criterion in the right side of FLC

The assumption of proportional loading path is utilized in most FLD theory. The strain ratio β is defined as

$$\beta = \frac{d\varepsilon_2}{d\varepsilon_1} \tag{3.15}$$

Where $d\varepsilon_1$ and $d\varepsilon_2$ are major strain and minor strains individually of the sheet plane.

When $d\varepsilon_2 \geq 0$ or $\beta \geq 0$, the deformation of the material is stretched in both sides of major and minor directions. The localized necking plane of the metal sheet in this situation is perpendicular to the major tensile direction in the sheet plane. Meanwhile, the necking plane will pass throng the thickness direction with a certain angle.

Let the coordinate direction system on the material main directions, direction **1** is the major direction of the sheet metal, direction **2** is the minor direction of the sheet metal and direction **3** is the thickness direction of the sheet metal. The related angles with the definitions mentioned above under the condition $\beta \geq 0$ are shown in Fig.3.2, here $\varphi = 0^\circ$. The related directional cosines of **n** in such situation are follows:

$$n_1 = \cos\theta \tag{3.16}$$

$$n_2 = 0 \tag{3.17}$$

$$n_3 = \sin\theta \tag{3.18}$$

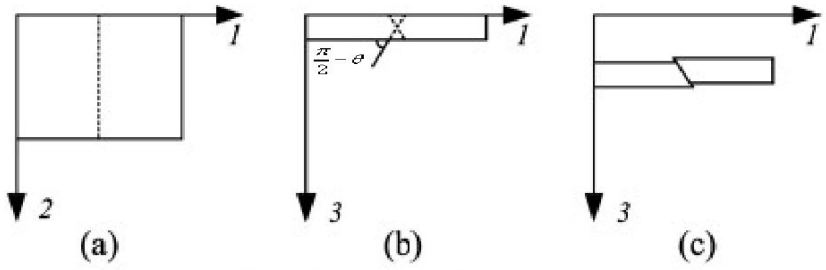

Fig. 3.2 Shear failure in the positive strain ratio region (Lin, Chan and Wang 2010)

Then the maximum shear stress can be obtained using the equation (3.1)

$$\tau = \sigma_{11}\sqrt{n_1^{\,2} - n_1^{\,4}} = \frac{1}{2}\sigma_{11}\sin 2\theta \tag{3.19}$$

In order to determine θ, a Mohr's circle was utilized by J. D. Bressan and J. A. Williams (1983), from which the pure shear point was characterized by angle θ. The variable of θ can be expressed with the related strain increment $d\varepsilon_1$ and $d\varepsilon_2$ as follows

$$\cos 2\theta = \frac{-\dfrac{d\varepsilon_1 + d\varepsilon_3}{2}}{\dfrac{d\varepsilon_1 - d\varepsilon_3}{2}} \tag{3.20}$$

It is assumed that the volume is constant, i.e.

$$d\varepsilon_1 + d\varepsilon_2 + d\varepsilon_3 = 0 \tag{3.21}$$

Then (3.20) can be expressed as

$$\cos 2\theta = \frac{d\varepsilon_2}{2d\varepsilon_1 + d\varepsilon_2} \tag{3.22}$$

According to the equation (3.15), the (3.22) can be obtained as follows

$$\cos 2\theta = \frac{\beta}{2+\beta} \tag{3.23}$$

The corresponding stress can be illustrated in the Mohr's stress circle, and the following equation can be obtained based on the related geometric relationships.

$$\sin 2\theta = \frac{2\tau_{cr}}{\sigma_{11}} \tag{3.24}$$

Where, τ_{cr} is shear criterion of the material and σ_{11} is the major stress.

From the equation (3.23) and (3.24), the follows exist (BRESSAN and WILLIAMS 1983a)

$$\sigma_{11} = \frac{2+\beta}{\sqrt{1+\beta}}\tau_{cr} \tag{3.25}$$

3.1.2 Determination of shear criterion in the left side of FLC

When $d\varepsilon_2 < 0$ or $\beta < 0$, the major strain and minor strain will locate in the left side of the FLC. Unlike in the situation $\beta > 0$, the shear planes in this situation usually locate in the sheet metal cross section randomly and pass through the thickness plane and sheet

surface plane with random angles. The inclined plane of local necking area which will pass through the thickness direction is shown in Fig.3.3, the plane will make two cross lines on plane **1-2** and **1-3** individually, the angles between the cross lines and the direction **1** are illustrated in the Fig.3.1, the coordinate in which is defined as the same as it is in $\beta > 0$.

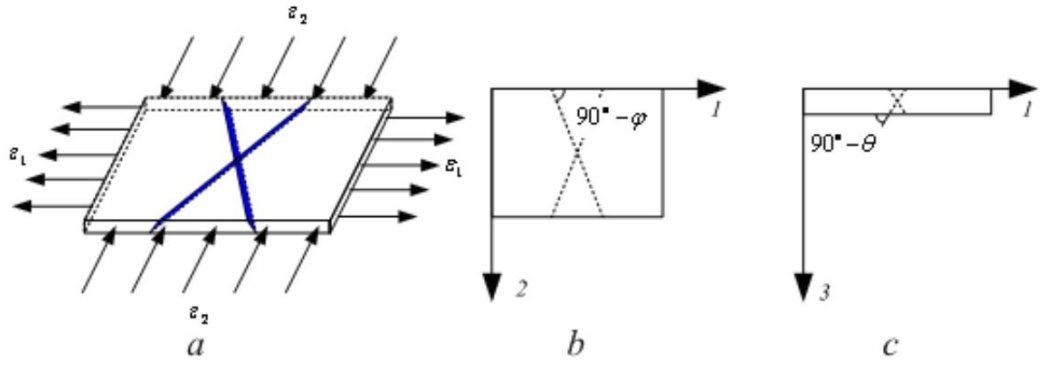

Fig. 3.3 Shear failure in the negative strain ratio region (L.C. Chan et al., 2011)
a, sketch of shear plane b, the location of shear localization in 1-2 plane;
c, the location of shear localization in 1-3 plane;

Because the LHS had been predicted by Hill (Hill 1952a) and the theory can not be used in the RHS due to its basic physical assumption, the shear failure criterion had been first proposed by BRESSAN and WILLIAMS (1983) to study the RHS of FLC. Chan Lin and Wang had extended the criterion to the LHS recently (Chan et al. 2010), however,

some unreasonable deductions exist in their article in determining the relationship between the cross directions of shear plane locate in sheet surfaces and normal direction. These mistakes influenced the results directly. In the present study, a detailed discussion of shear criterion on the LHS will introduced as follows.

The shear plane in such condition will cross the metal sheet, and produce 2 pairs of parallel cross lines in four surfaces. When define the same coordinate directions as introduced above. Surface **1-2** is used to name the out surface of the sheet, which parallels to the coordinate plane composed of coordinate axis **1** and coordinate axis **2**. Surface **1-3** is used to name the sheet surface on the thickness direction, which parallels to the coordinate plane composed of coordinate axis **1** and coordinate axis **3**.

The normal direction of the shear plane is **n,** The angle between **n** and coordinate axis **2** is defined as ψ, the angle between coordinate axis **1** and the direction of the projection of **n** in plane **1-3** is defined as θ. Such definition is similar to the definitions used in Fig. 3.1 then the results obtained in previous section can also be used here. The directional cosines of **n** of the shear plane in condition $\beta < 0$ follow equations (3.12)-(3.14)

Based on the definitions of angles of the normal direction **n,** the angle between the cross line in surface **1-2** and the coordinate axis **1** is $\frac{\pi}{2}-\theta$, the angle between the cross line in surface **1-3** and the coordinated axis **1** is $\frac{\pi}{2}-\varphi$. The related angles are shown in Fig 3.3.

n_1^{1-2} is used to define the directional cosines of cross lines in surface **1-2** in direction **1** and n_2^{1-2} is used to define the directional cosines of cross lines in surface **1-2** in direction **2**, the similar definition is given to n_1^{1-3} and n_2^{1-3}.

Apparently, the directional cosines of the cross lines in surface **1-2** is

$$n_1^{1-2}=\cos(\frac{\pi}{2}-\varphi) \tag{3.26}$$

$$n_2^{1-2}=\sin(\frac{\pi}{2}-\varphi) \tag{3.27}$$

The directional cosines of the cross lines in surface **1-3** is

$$n_1^{1-3}=\cos(\frac{\pi}{2}-\theta) \tag{3.28}$$

$$n_3^{1-3}=\sin(\frac{\pi}{2}-\theta) \tag{3.29}$$

Under the shear condition, the grains of the material experience slip between different slip planes, and only space slip movement is endured of the slip plane when they move toward each other. Meanwhile, constant geometric shapes are kept by them when they

are in moving. So any strain of the shear plane among the plane surface can be regarded as zero. $d\varepsilon_t$ and $d\varepsilon_t$ are defined as the strains along cross lines of shear plane in surface **1-2** and surface **1-3**, then the following equation can be obtained

$$d\varepsilon_c = 0 \tag{3.30}$$

$$d\varepsilon_t = 0 \tag{3.31}$$

The strain increments in direction **1**, **2** and **3** are defined as $d\varepsilon_1$, $d\varepsilon_2$ and $d\varepsilon_3$. Using the results of (3.30) and (3.31), the following relationships can be obtained to determine the angle θ in the plane **1-3**, (Hill 2001)

$$d\varepsilon_1 \cos^2(\frac{\pi}{2} - \theta) + d\varepsilon_3 \sin^2(\frac{\pi}{2} - \theta) = 0 \tag{3.32}$$

Based on the equation (3.31) following relationship can be used to determined the angle φ in the plane **1-2**,

$$d\varepsilon_1 \cos^2(\frac{\pi}{2} - \varphi) + d\varepsilon_2 \sin^2(\frac{\pi}{2} - \varphi) = 0 \tag{3.33}$$

From equation (3.32) and noticed (3.21) the variable of θ can be obtained

$$\sin\theta = \sqrt{\frac{1+\beta}{2+\beta}} \tag{3.34}$$

$$\cos\theta = \frac{1}{\sqrt{2+\beta}} \tag{3.35}$$

From equation (3.33) the variable of φ can be obtained

$$tg\varphi = \sqrt{-\beta} \tag{3.36}$$

Put equations (3.34)-(3.36) into (3.12)-(3.14), the directional cosines of the **n** can be obtained as follows

$$n_1 = \sqrt{\frac{1}{2}} \tag{3.37}$$

$$n_2 = \sqrt{-\frac{\beta}{2}} \tag{3.38}$$

$$n_3 = \sqrt{\frac{1+\beta}{2}} \tag{3.39}$$

Put equations (3.37)-(3.39) into (3.1), the maximum shear stress on the sheet when $\beta < 0$ can be obtained

$$\tau = \frac{\sqrt{\sigma_{11}^2 - \sigma_{22}^2\beta(2+\beta) + 2\beta\sigma_{11}\sigma_{22}}}{2} \tag{3.40}$$

The localized necking will occur when the maximum shear stress reaches the shear stress criterion, then the localized necking condition is following

$$\frac{\sqrt{\sigma_{11}^2 - \sigma_{22}^2\beta(2+\beta) + 2\beta\sigma_{11}\sigma_{22}}}{2} = \tau_{cr} \tag{3.41}$$

When $\beta = 0$, the minor strain is zero and the FLC will cross the horizontal coordinate axis. The metal sheet is under the plane strain condition, and the maximum shear stress in this situation can be obtained from (3.40)

$$\tau = \frac{\sigma_{11}}{2}$$

The same result can also be obtained from (3.25), when putting $\beta = 0$ in it, accordance of the FLC criterion in both LHS and RHS can be shown. Some extended discussion on combined criterion and the determination of critical plane strain had be conducted by author and his group colleagues in their later work.

3.2 Damage model for shear failure criterion

In order to take the degradation of the material during the process into considerations, anisotropic damage theory is utilized in the present study. The tubes used in the THF possess a distinguished difference between axial direction and hoop direction. It is reasonable to assume orthotropic plasticity to be the property of the material. Meanwhile, material and damage are assumed to be coincided with each other. The effective equivalent stress can be obtained based on Hill's quadratic yield criterion.

$$\bar{\sigma}_{eq} = (\frac{1}{2}\bar{\boldsymbol{\sigma}}^{T}\boldsymbol{H}\bar{\boldsymbol{\sigma}})^{\frac{1}{2}} \tag{3.42}$$

Where $\bar{\sigma}$ is two dimensional effective stress effective stress tensor, follows (2.1).

The matrix form of **H** is

$$\mathbf{H} = \begin{bmatrix} 2 & -H \\ -H & F+H \end{bmatrix} \tag{3.43}$$

where

$$H = \frac{2r_0}{1+r_0} \tag{3.44}$$

$$F = \frac{2r_0}{r_{90}(1+r_0)} \tag{3.45}$$

Where r_0 and r_{90} are orthotropic plasticity parameters.

Using the plastic flow rule

$$d\boldsymbol{\varepsilon} \approx d\boldsymbol{\varepsilon}^p = d\lambda \frac{\partial F_p}{\partial \boldsymbol{\sigma}} \tag{3.46}$$

As

$$F_p = \bar{\sigma}_{eq} - (T + T(p)) \tag{3.47}$$

Put (3.47) into (3.46), the (3.46) becomes

$$\begin{aligned} d\boldsymbol{\varepsilon} &\approx d\lambda \frac{\partial \bar{\sigma}_{eq}}{\partial \boldsymbol{\sigma}} \\ &= d\lambda \left(\frac{\partial \bar{\sigma}_{eq}}{\partial \bar{\boldsymbol{\sigma}}}^T \frac{\partial \bar{\boldsymbol{\sigma}}}{\partial \boldsymbol{\sigma}} \right)^T \end{aligned} \tag{3.48}$$

From the equation (3.42) the following equation can be deduced.

$$\frac{\partial \bar{\sigma}_{eq}}{\partial \bar{\boldsymbol{\sigma}}} = \frac{\boldsymbol{H}\bar{\boldsymbol{\sigma}}}{2\bar{\sigma}_{eq}} \tag{3.49}$$

From the equation (2.1) the following equation is deduced

$$\frac{\partial \bar{\boldsymbol{\sigma}}}{\partial \boldsymbol{\sigma}} = \boldsymbol{M}^T \tag{3.50}$$

Put (3.49) and (3.50) into (3.48)

$$d\boldsymbol{\varepsilon} \approx \frac{d\lambda}{2\bar{\sigma}_{eq}} \boldsymbol{M}^T \boldsymbol{H} \bar{\boldsymbol{\sigma}} \tag{3.51}$$

Using the energy equivalent principal, the following is obtained

$$\boldsymbol{\sigma}^T d\boldsymbol{\varepsilon} = \bar{\sigma}_{eq} d\bar{\varepsilon}_{eq} \tag{3.52}$$

Put (3.51) into (3.52), and noted the equation (3.42)

$$\boldsymbol{\sigma}^T d\lambda \boldsymbol{M}^T \boldsymbol{H} \bar{\boldsymbol{\sigma}} = \bar{\boldsymbol{\sigma}}^T \boldsymbol{H} \bar{\boldsymbol{\sigma}} d\bar{\varepsilon}_{eq} \tag{3.53}$$

$$= \boldsymbol{\sigma}^T \boldsymbol{M}^T \boldsymbol{H} \bar{\boldsymbol{\sigma}} d\bar{\varepsilon}_{eq}$$

The follows is obtained

$$d\lambda = d\bar{\varepsilon}_{eq} \tag{3.54}$$

Put (3.54) into (3.51)

$$d\boldsymbol{\varepsilon} \approx \frac{d\bar{\varepsilon}_{eq}}{2\bar{\sigma}_{eq}} \boldsymbol{M}^T \boldsymbol{H} \bar{\boldsymbol{\sigma}} \tag{3.55}$$

As $d\boldsymbol{\varepsilon}$, $\boldsymbol{M}$ and $\bar{\boldsymbol{\sigma}}$ are defined as follows (Chow 1989)

$$d\boldsymbol{\varepsilon} = \begin{bmatrix} d\varepsilon_1 \\ d\varepsilon_2 \end{bmatrix} \tag{3.56}$$

$$\boldsymbol{M} = \begin{bmatrix} \dfrac{1}{1-D_1} & 0 \\ 0 & \dfrac{1}{1-D_2} \end{bmatrix} \tag{3.57}$$

$$\bar{\boldsymbol{\sigma}} = \begin{bmatrix} \overline{\sigma_1} \\ \overline{\sigma_2} \end{bmatrix} \tag{3.58}$$

Put (3.56), (3.57) and (3.58) into (3.55)

$$\begin{bmatrix} d\varepsilon_1 \\ d\varepsilon_2 \end{bmatrix} = \frac{d\bar{\varepsilon}_{eq}}{2\bar{\sigma}_{eq}} \begin{bmatrix} \dfrac{1}{1-D_1} & 0 \\ 0 & \dfrac{1}{1-D_2} \end{bmatrix} \begin{bmatrix} 2 & -H \\ -H & F+H \end{bmatrix} \begin{bmatrix} \overline{\sigma_1} \\ \overline{\sigma_2} \end{bmatrix}$$

$$= \frac{d\bar{\varepsilon}_{eq}}{2\bar{\sigma}_{eq}} \begin{bmatrix} \dfrac{2}{1-D_1} & -\dfrac{H}{1-D_1} \\ -\dfrac{H}{1-D_2} & \dfrac{F+H}{1-D_2} \end{bmatrix} \begin{bmatrix} \bar{\sigma}_1 \\ \bar{\sigma}_2 \end{bmatrix} \tag{3.59}$$

Then, the effective stress can be expressed with strain increment as follows

$$\begin{bmatrix} \bar{\sigma}_1 \\ \bar{\sigma}_2 \end{bmatrix} = \frac{2\sigma_{eq}(1-\bar{D}_1)(1-D_2)}{d\bar{\varepsilon}_{eq}} \begin{bmatrix} B_1 & B_2 \\ B_3 & B_4 \end{bmatrix} \begin{bmatrix} d\varepsilon_1 \\ d\varepsilon_2 \end{bmatrix} \tag{3.60}$$

where

$$
\begin{aligned}
B_1 &= \frac{1}{2} + \frac{H^2}{2(2F + 2H - H^2)} \\
B_2 &= \frac{H}{2F + 2H - H^2} \\
B_3 &= \frac{H}{2F + 2H - H^2} \\
B_4 &= \frac{2}{2F + 2H - H^2}
\end{aligned}
\tag{3.61}
$$

So, according to hypothesis of stress equivalence, for the RHS of the FLD, the criterion can be expressed from (3.25) as follows

$$
\overline{\sigma_1} = \frac{2\tau_{cr}}{\sin 2\theta} = \frac{2+\beta}{\sqrt{1+\beta}}\tau_{cr} \tag{3.62}
$$

With the equation (3.60) the localized necking condition on the RHS is obtained as follows when considering the material damage

$$
\frac{2\bar{\sigma}_{eq}}{d\bar{\varepsilon}_{eq}} \frac{\sqrt{1+\beta}(B_1 + B_2\beta)(1-D_1)(1-D_2)}{2+\beta} d\varepsilon_1 = \tau \tag{3.63}
$$

The critical damage for forming limit at the RHS is defined as

$$
S_{cr1} = 1 - (1-D_1)(1-D_2) = 1 - \frac{d\bar{\varepsilon}_{eq}(2+\beta)}{2\sigma_{eq} d\varepsilon_1 \sqrt{1+\beta}(B_1 + B_2\beta)}\tau_{cr} \tag{3.64}
$$

It is noted that the damage criterion here is not a constant. It is determined by both of damage variables and stress strain conditions.

For the left hand-side of the FLD

$$\tau_{cr} = \frac{\sqrt{\bar{\sigma}_{11}^2 - \bar{\sigma}_{22}^2\beta(2+\beta) + 2\beta\sigma_{11}\sigma_{22}}}{2} \tag{3.65}$$

The equation (3.60) can be used to obtain the effective stress components. Then, the critical localized necking condition on the LHS of FLC can be explicitly expressed with strain and damage parameters as the following

$$\frac{2\bar{\sigma}_{eq}\, d\varepsilon_1 (1-D_1)(1-D_2)}{d\bar{\varepsilon}_{eq}} \sqrt{F_4\beta^4 + F_3\beta^3 + F_2\beta^2 + F_1\beta + F_0} = \tau_{cr} \tag{3.66}$$

Where

$$\begin{aligned} F_0 &= B_1^2 \\ F_1 &= 4B_1B_2 - 2B_3^2 \\ F_2 &= 3B_2^2 - B_3^2 + 2B_1B_4 - 4B_3B_4 \\ F_3 &= -2B_4^2 \\ F_4 &= -B_4^2 \end{aligned} \tag{3.67}$$

The critical damage for forming limit at the RHS is defined as

$$S_{cr2} = 1 - (1-D_1)(1-D_2) = 1 - \frac{\tau_{cr} d\bar{\varepsilon}_{eq}}{2\bar{\sigma}_{eq}\, d\varepsilon_1 \sqrt{F_4\beta^4 + F_3\beta^3 + F_2\beta^2 + F_1\beta + F_0}} \tag{3.68}$$

The shear criterion is concerned mainly with the maximum shear stress of a slip system that exists in sheet metals. The degradation of materials has been observed in many metals. The theoretical fundamental of the shear criterion includes plastic mechanics

and anisotropic damage mechanics. Consequently, the criterion is able to predict different kinds of sheet metals; that is, there is no limitation with most metallic sheet materials to use the proposed shear criterion. In other words, it is capable for other materials aside from aluminum alloy.

A brief mathematical analysis on the tubular hydroforming is given in this section, with which the failure condition of the components in the process is discussed using main process parameters. The damage coupled shear criterion is used in the failure analysis to identify the safety loading region and bursting loading region.

The deformation of tubular components in THF process is determined by material properties, geometry of tubes and the loading condition. The loading path is composed of two loading parameters including axial feeding force F and internal pressure p. The material of tubular components will yield at first and then deformed under certain plastic flow rules. The tubes are reasonably assumed as anisotropic material. When using incremental plasticity model for anisotropic materials, the yield potential are follows

$$F(\boldsymbol{\sigma}) = \sigma_{eq} - Y(p) \tag{3.69}$$

Where σ_{eq}, $Y(p)$ and p are the equivalent stress, the strain hardening function and the equivalent plastic strain respectively.

Some assumptions are usually utilized when considering the analytic study of the hydroformed tubular components. The following relationship is exist because of the force balance in the tube section

$$\sigma_r = \frac{2t}{D}\sigma_\theta \tag{3.70}$$

Where σ_r and σ_θ are the radical stress and hoop stress.

Usually $t << D$, which means

$$\sigma_r << \sigma_\theta \tag{3.71}$$

The plane stress condition is reasonably used in characterizing the stress state of tubes during the hydroforming due to the small ratio of thickness to radius.

Then the stress vector of the material can be expressed as follows:

$$\boldsymbol{\sigma} = (\sigma_x, \sigma_\theta, \sigma_{r\theta})^T \tag{3.72}$$

Where σ_x and $\sigma_{r\theta}$ are the axial stress and shear stress. When the material main direction is the same as the stress main direction $\sigma_{r\theta} = 0$.

The equivalent stress then can be obtained when using R-value to represent normal anisotropy as follows

$$\sigma_{eq} = \sqrt{\sigma_x^{\,2} + \sigma_\theta^{\,2} - \frac{2R}{R+1}\sigma_x\sigma_\theta} \tag{3.73}$$

The corresponding strain vector of the material can expressed as follows

$$\varepsilon = (\varepsilon_x, \varepsilon_\theta, \varepsilon_{r\theta})^T \tag{3.74}$$

When using associated flow rule the plastic strain increments can be given

$$d\varepsilon_x^{\ p} = \frac{\sigma_x - R\sigma_\theta / 1+R}{Y(p)} dp \tag{3.75}$$

$$d\varepsilon_\theta^{\ p} = \frac{\sigma_\theta - R\sigma_x / 1+R}{Y(p)} dp \tag{3.76}$$

$$dp = \frac{1+R}{\sqrt{1+2R}} \sqrt{(d\varepsilon_x^p)^2 + (d\varepsilon_\theta^p)^2 + \frac{2R}{1+2R} d\varepsilon_x^p d\varepsilon_\theta^p} \tag{3.77}$$

Where $d\varepsilon_x^{\ p}$ and $d\varepsilon_\theta^{\ p}$ are the plastic part of the strain increment components along axial and loop directions.

Under the THF process, the material will flow in yield state, so the loading condition of the state can be expressed as (Xia 2001)

$$F(\boldsymbol{\sigma}) = 0 \tag{3.78}$$

$$dF(\boldsymbol{\sigma}) \geq 0 \tag{3.79}$$

From the above the follows can be obtained

$$\frac{\partial F}{\partial \sigma_x} d\sigma_x + \frac{\partial F}{\partial \sigma_\theta} d\sigma_\theta \geq 0 \tag{3.80}$$

In the THF process, consider a bulge experiment. Assume the die provide sufficient space for the extension of the tube. The original length, thickness and radius of the tube is set as l_0 , t_0 and r_0 , which are all measured from the mid-surface across tube thickness. After the experiment, the tube will be bulged to certain shape characterized as length l, thickness t and radius r.

The true strains of the tubes can be expressed as follows:

$$\varepsilon_x = \ln(\frac{l}{l_0}) \tag{3.81}$$

$$\varepsilon_\theta = \ln(\frac{r}{r_0}) \tag{3.82}$$

The thickness strain is assumed average and obtained using incompressibility property of the material as follows:

$$\varepsilon_r = -(\varepsilon_x + \varepsilon_\theta) \tag{3.83}$$

Then the effective strain can be deduced as,

$$\varepsilon_{eq} = \frac{1+R}{\sqrt{1+2R}} \sqrt{\varepsilon_x{}^2 + \varepsilon_\theta{}^2 + \frac{2R}{1+R}\varepsilon_x\varepsilon_\theta} \tag{3.84}$$

The relationship between effective stress and the effective strain is,

$$\sigma_{eq} = f(\varepsilon_{eq}) \tag{3.85}$$

The material used in the present study is AA 6063, the main material properties of it are: Young's modulus $E = 70GPa$, Poisson's ratio $\nu = 0.3$, yield stress $\sigma_s = 150MPa$, anisotropy value $R = 0.68$. The strain stress relationship of the material is,

$$\sigma_{eq} = 489.31\varepsilon_{eq}^{0.233} \tag{3.86}$$

The loading feed on the tubes can be set as axial feed force F and internal pressure P , the proportional loading path is assumed in the following discussion. With which the deformation plasticity theory can be utilized in the study, and the following expression can be obtained,

$$\sigma_\theta = \frac{(1+R)^2}{1+2R}\frac{\sigma_{eq}}{\varepsilon_{eq}}(\varepsilon_\theta + \frac{R}{1+R}\varepsilon_x) \tag{3.87}$$

$$\sigma_x = \frac{(1+R)^2}{1+2R}\frac{\sigma_{eq}}{\varepsilon_{eq}}(\varepsilon_x + \frac{R}{1+R}\varepsilon_\theta) \tag{3.88}$$

The internal pressure p is derived from the force equilibrium in the tube section,

$$p = \frac{\sigma_\theta t}{r} \tag{3.89}$$

And t can be obtained from the volume conservation as

$$t = \frac{r_0 t_0 l_0}{rl} \tag{3.90}$$

The tube wall will become thinner during the process due to stretching on its hoop direction. The deformation of the tube is influence by the loading path provided on it.

When the internal pressure is beyond certain peak value, the tube will burst. The onset of bursting can be give by (Xia 2001)

$$\frac{dp}{dr} = 0 \tag{3.91}$$

The discussion above are all based assumption that there are no material variation during the THF process, however, in a bulge hydroforming process the material will be fed into the die cavity and compensate the thinner rate of the tube. Then the bulging part of the tube will be increased gradually on a designed rate.

3.3 Forming limit curve from prediction

3.3.1 FLDs calculation program

The forming limit curve based on the proposed damage coupled shear criterion is calculated using a self-developed FORTRAN program. The material properties and the damage parameters of AA6063 tubes are required in the calculation. These parameters are obtained from experiments or referred from published articles

In order to determine FLC, the values of forming limit strains should be calculated out in a wide range of strain ratio and displayed in the 1- 2 relationship diagram. Each strain ratio represents a proportional loading path. The values of strain ratios are selected from -0.5 to 1 in the present study. This strain ratios are corresponding to different sheet metal forming deformation modes which include: uniaxial tension, plain strain, equal biaxial stretch et al. (Z. Marciniak, J.L. Duncan and S.J. Hu 2002).

In each strain ratio shear failure criterion are calculated using method introduced in section 3.2. Strain of the material is increased using a fixed step as 0.000001 which correspond to gradually increased deformation.

The first strain value is as 0 represent as received material, after then, major strain is added with 0.000001 and minor strain then can be obtained by the strain ratio and major strain. In each step, major strain and minor strain are put into the anisotropic damage constitution to calculate corresponding stress. The stress then used to compare with the shear failure criterion. If it is larger than the criterion, the values of the major strain and minor strain then can be regarded as the forming limit strain in this strain ratio. It indicates that when the material is loaded under a proportional strain path with this strain ratio and deformed reach this strain value, localized necking will occur and

material cannot processed after then. If the stress less than the criterion it indicates that the material is well in this deformation stage and can endure more loading to produce more deformation. The strain then is added an increment to reach next step, stress is calculated and compared again like above. Repeat this calculation until the stress reaches the criterion. The major strain and minor strain in the last step are then recorded as the strain limit of this strain ratio.

Calculation begins with strain ratio equal to -0.5 which is corresponding to uniaxial tension. When the strain limit of a strain ratio is determined, 0.00075 will be added to the strain ratio to indicate another loading path. The limit strain in the new strain ratio is calculated again. Repeat this process till the strain ratio reaches 1 which corresponds to equal biaxial stretching.

There are totally 200 points of strain limit are calculated in this study, the values of these limit strains are then marked in the strain diagram. Then a smooth FLC can be obtained. The flow chart of the FLDs calculation program is shown in Fig. 3.2.

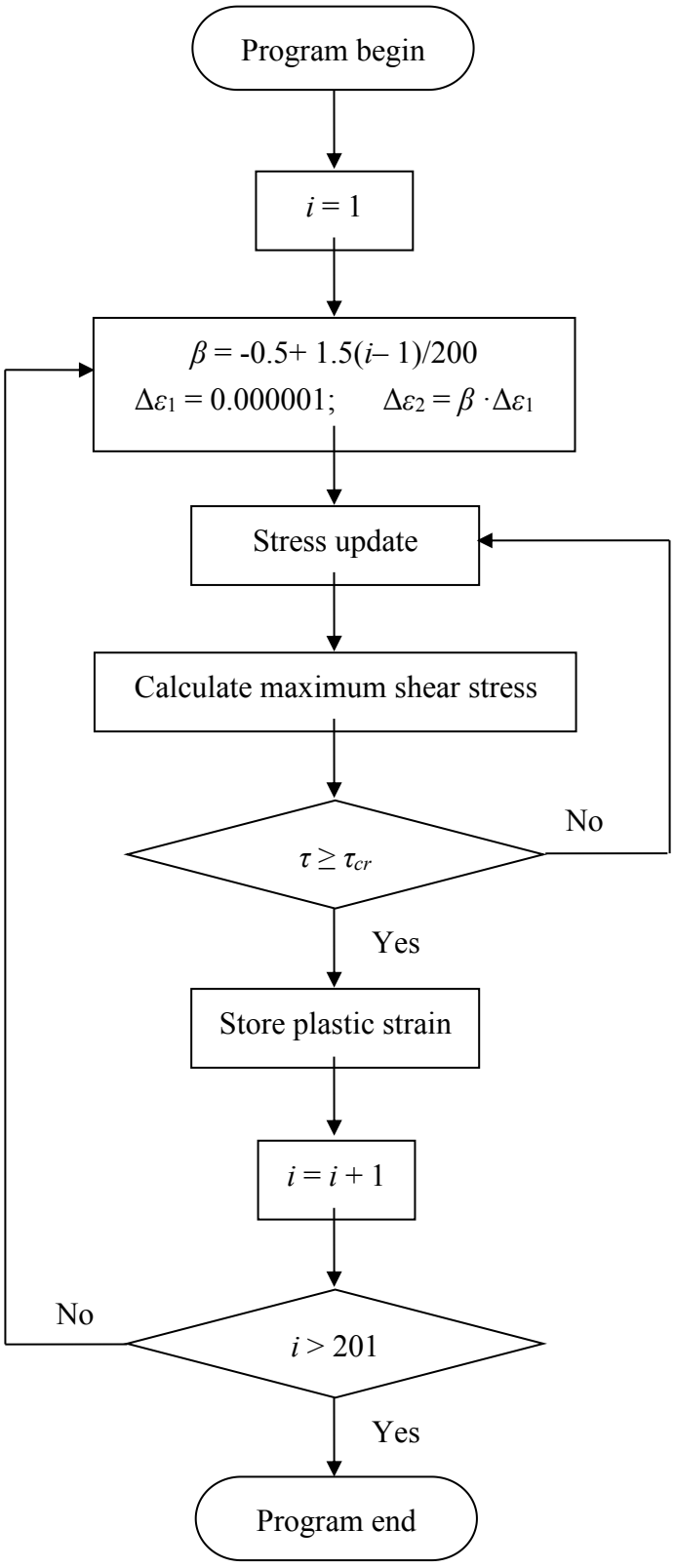

Fig.3.4 Flow chart of the program for FLC calculation.

3.3.2 Derivation of matrix form $\overline{\boldsymbol{C}}^{ep}$

The main part of the FLDs calculation program is the stress update in each strain increment step. In order to achieve the stress update calculation, the effective hardening modulus tensor $\overline{\boldsymbol{C}}^{ep}$ should be computed in advance. The equations in deducing $\overline{\boldsymbol{C}}^{ep}$ are tensor form (Chow and Jie 2004, Chow and Yang 2002). In order to code FORTRAN program, matrix form expression is required. The derivation of matrix form $\overline{\boldsymbol{C}}^{ep}$ is introduced in this section.

Similar to the yield surface, the damage surface is assumed as following

$$F_d = Y_{eq} - \left[C_0 + C(Z)\right] = 0 \tag{3.92}$$

Where is defined as

$$Y_{eq} = \left(\frac{1}{2}\boldsymbol{Y}^T : \boldsymbol{N} : \boldsymbol{Y}\right) \tag{3.93}$$

Here Y_{eq} is expressed as

$$Y_{eq} = \frac{1}{2}\boldsymbol{\sigma}^T : (\overline{\boldsymbol{C}}^{e-1} : \frac{\partial \boldsymbol{P}}{\partial \boldsymbol{D}} : \boldsymbol{M}^2)^s : \boldsymbol{\sigma} \tag{3.94}$$

where

$$\overline{\boldsymbol{C}}^{e-1} = \begin{bmatrix} \frac{1}{(1-D_1)^2 e_0} & -\frac{1}{(1-D_1)(1-D_2)e_0} & 0 \\ -\frac{1}{(1-D_1)(1-D_2)e_0} & \frac{1}{(1-D_2)^2 e_0} & 0 \\ 0 & 0 & \frac{2(1+\nu)}{(1-D_1)(1-D_2)e_0} \end{bmatrix} \tag{3.95}$$

$$\overline{\boldsymbol{C}}^{e-1} : \frac{\partial \boldsymbol{P}}{\partial D_{11}} : \boldsymbol{M}^2 = \begin{bmatrix} \frac{1}{(1-D_1)^2 e_0} & -\frac{1}{(1-D_1)(1-D_2)e_0} & 0 \\ -\frac{1}{(1-D_1)(1-D_2)e_0} & \frac{1}{(1-D_2)^2 e_0} & 0 \\ 0 & 0 & \frac{2(1+\nu)}{(1-D_1)(1-D_2)e_0} \end{bmatrix} :$$

$$\begin{bmatrix} -2(1-D_{11}) & 0 & 2D_{12} \\ 0 & 0 & 0 \\ D_{21} & 0 & -1+D_{22} \end{bmatrix} : \left[\boldsymbol{M}^2 \right]$$

$$= \begin{bmatrix} \frac{-2}{(1-D_1)^3 e_0} & 0 & 0 \\ -\frac{1}{(1-D_1)^2 (1-D_2)e_0} & 0 & 0 \\ 0 & 0 & \frac{-2(1+\nu)}{(1-D_1)^2 (1-D_2)e_0} \end{bmatrix}$$

(3.96)

$$\overline{\boldsymbol{C}}^{e-1} : \frac{\partial \boldsymbol{P}}{\partial D_{12}} : \boldsymbol{M}^2 = \begin{bmatrix} \frac{1}{(1-D_1)^2 e_0} & -\frac{1}{(1-D_1)(1-D_2)e_0} & 0 \\ -\frac{1}{(1-D_1)(1-D_2)e_0} & \frac{1}{(1-D_2)^2 e_0} & 0 \\ 0 & 0 & \frac{2(1+\nu)}{(1-D_1)(1-D_2)e_0} \end{bmatrix} :$$

$$\begin{bmatrix} 0 & 2D_{12} & -2(1-D_{11}) \\ 0 & 0 & 0 \\ 0 & -1+D_{22} & D_{21} \end{bmatrix} : \left[\boldsymbol{M}^2 \right]$$

$$= \begin{bmatrix} 0 & 0 & -\frac{-2}{(1-D_1)^2(1-D_2)e_0} \\ 0 & 0 & \frac{2\nu}{(1-D_1)(1-D_2)^2 e_0} \\ 0 & -\frac{-2(1+\nu)}{(1-D_1)(1-D_2)^2 e_0} & 0 \end{bmatrix}$$

(3.97)

$$\overline{\boldsymbol{C}}^{e-1} : \frac{\partial \boldsymbol{P}}{\partial D_{21}} : \boldsymbol{M}^2 = \begin{bmatrix} \frac{1}{(1-D_1)^2 e_0} & -\frac{1}{(1-D_1)(1-D_2)e_0} & 0 \\ -\frac{1}{(1-D_1)(1-D_2)e_0} & \frac{1}{(1-D_2)^2 e_0} & 0 \\ 0 & 0 & \frac{2(1+\nu)}{(1-D_1)(1-D_2)e_0} \end{bmatrix} :$$

$$\begin{bmatrix} 0 & 0 & 0 \\ 2D_{21} & 0 & 0 \\ -1+D_{11} & 0 & D_{12} \end{bmatrix} : \left[\boldsymbol{M}^2 \right]$$

$$= \begin{bmatrix} 0 & 0 & -\frac{2\nu}{(1-D_1)^2(1-D_2)e_0} \\ 0 & 0 & \frac{-2}{(1-D_1)(1-D_2)^2 e_0} \\ -\frac{-2(1+\nu)}{(1-D_1)^2(1-D_2)e_0} & 0 & 0 \end{bmatrix}$$

(3.98)

$$\overline{\boldsymbol{C}}^{e-1} : \frac{\partial \boldsymbol{P}}{\partial D_{21}} : \boldsymbol{M}^2 = \begin{bmatrix} \frac{1}{(1-D_1)^2 e_0} & -\frac{1}{(1-D_1)(1-D_2)e_0} & 0 \\ -\frac{1}{(1-D_1)(1-D_2)e_0} & \frac{1}{(1-D_2)^2 e_0} & 0 \\ 0 & 0 & \frac{2(1+\nu)}{(1-D_1)(1-D_2)e_0} \end{bmatrix} :$$

$$\begin{bmatrix} 0 & 0 & 0 \\ 0 & -2(1-D_{11}) & 2D_{21} \\ 0 & D_{12} & -(1-D_{11}) \end{bmatrix} : \left[\boldsymbol{M}^2\right]$$

$$= \begin{bmatrix} 0 & -\frac{2\nu}{(1-D_1)(1-D_2)^2 e_0} & 0 \\ 0 & -\frac{2}{(1-D_2)^3 e_0} & 0 \\ 0 & 0 & -\frac{2(1+\nu)}{(1-D_1)(1-D_2)^2 e_0} \end{bmatrix}$$

(3.99)

Where $\frac{\partial \boldsymbol{P}}{\partial D_{11}}$ $\frac{\partial \boldsymbol{P}}{\partial D_{12}}$ $\frac{\partial \boldsymbol{P}}{\partial D_{21}}$ $\frac{\partial \boldsymbol{P}}{\partial D_{22}}$ can be found in Chow, Jie (2004) and noted that $D_{12} = D_{21} = 0$

$$\left(\sigma_1, \sigma_2, \sigma_3\right)\left[\overline{\boldsymbol{C}}^{e-1} : \frac{\partial \boldsymbol{P}}{\partial D_{11}} : \boldsymbol{M}^2\right]\left(\sigma_1, \sigma_2, \sigma_3\right)^T$$

$$= \frac{-2\sigma_1^{\,2}}{(1-D_2)^3 e_0} + \frac{2\nu\sigma_1\sigma_2}{(1-D_1)^2(1-D_2)e_0} - \frac{-2(1+\nu)\sigma_6}{(1-D_1)^2(1-D_2)e_0} \tag{3.104}$$

$$\left(\sigma_1, \sigma_2, \sigma_3\right)\left[\overline{\boldsymbol{C}}^{e-1} : \frac{\partial \boldsymbol{P}}{\partial D_{12}} : \boldsymbol{M}^2\right]\left(\sigma_1, \sigma_2, \sigma_3\right)^T$$

$$= -\frac{2\sigma_2\sigma_6}{(1-D_1)(1-D_2)^2} - \frac{2\sigma_1\sigma_6}{(1-D_1)^2(1-D_2)e_0} \tag{3.105}$$

$$\left(\sigma_1,\sigma_2,\sigma_3\right)\left[\overline{\boldsymbol{C}}^{e-1}:\frac{\partial \boldsymbol{P}}{\partial D_{21}}:\boldsymbol{M}^2\right]\left(\sigma_1,\sigma_2,\sigma_3\right)^T$$
$$=-\frac{2\sigma_2\sigma_6}{(1-D_1)(1-D_2)^2}-\frac{2\sigma_1\sigma_6}{(1-D_1)^2(1-D_2)e_0} \tag{3.106}$$

$$\left(\sigma_1,\sigma_2,\sigma_3\right)\left[\overline{\boldsymbol{C}}^{e-1}:\frac{\partial \boldsymbol{P}}{\partial D_{22}}:\boldsymbol{M}^2\right]\left(\sigma_1,\sigma_2,\sigma_3\right)^T$$
$$=\frac{2\nu\sigma_1\sigma_2-2(1+\nu){\sigma_6}^2}{(1-D_1)(1-D_2)^2e_0}-\frac{2{\sigma_2}^2}{(1-D_2)^3e_0} \tag{3.107}$$

$$\left[\overline{\boldsymbol{C}}^{e-1}:\frac{\partial \boldsymbol{P}}{\partial D_{11}}:\boldsymbol{M}^2\right]\left(\sigma_1,\sigma_2,\sigma_3\right)^T$$
$$=\left[\frac{-2{\sigma_1}^2}{(1-D_2)^3e_0},\quad\frac{2\nu\sigma_1}{(1-D_1)^2(1-D_2)e_0},\quad\frac{-2(1+\nu)\sigma_6}{(1-D_1)^2(1-D_2)e_0}\right]^T \tag{3.108}$$

$$\left[\overline{\boldsymbol{C}}^{e-1}:\frac{\partial \boldsymbol{P}}{\partial D_{12}}:\boldsymbol{M}^2\right]\left(\sigma_1,\sigma_2,\sigma_3\right)^T$$
$$=-\frac{2\sigma_2\sigma_6}{(1-D_1)(1-D_2)^2}-\frac{2\sigma_1\sigma_6}{(1-D_1)^2(1-D_2)e_0} \tag{3.109}$$

$$\left(\sigma_1,\sigma_2,\sigma_3\right)\left[\overline{\boldsymbol{C}}^{e-1}:\frac{\partial \boldsymbol{P}}{\partial D_{21}}:\boldsymbol{M}^2\right]\left(\sigma_1,\sigma_2,\sigma_3\right)^T$$
$$=-\frac{2\sigma_2\sigma_6}{(1-D_1)(1-D_2)^2}-\frac{2\sigma_1\sigma_6}{(1-D_1)^2(1-D_2)e_0} \tag{3.110}$$

$$\begin{aligned}&\left(\sigma_1,\sigma_2,\sigma_3\right)\left[\overline{\boldsymbol{C}}^{e-1}:\frac{\partial \boldsymbol{P}}{\partial D_{22}}:\boldsymbol{M}^2\right]\left(\sigma_1,\sigma_2,\sigma_3\right)^T\\&=\frac{2\nu\sigma_1\sigma_2-2(1+\nu)\sigma_6{}^2}{(1-D_1)(1-D_2)^2e_0}-\frac{2\sigma_2{}^2}{(1-D_2)^3e_0}\end{aligned}\tag{3.111}$$

$$\boldsymbol{M}^{-1}=\begin{bmatrix}1-D_1 & 0 & 0\\ 0 & 1-D_2 & 0\\ 0 & 0 & \sqrt{(1-D_1)(1-D_2)}\end{bmatrix}\tag{3.112}$$

$$\boldsymbol{\sigma}=\begin{pmatrix}\sigma_1 & \sigma_2 & \sigma_3\end{pmatrix}^T$$

A^{-1} can be derived from reversing matrix A (26) in (Chow and Jie 2004)

$$\boldsymbol{A}=\boldsymbol{I}+\alpha\left\{\frac{\partial \boldsymbol{M}}{\partial \boldsymbol{D}^T}:\frac{\partial F_d}{\partial(-\boldsymbol{Y})}:\boldsymbol{M}^{-1}+\left[\boldsymbol{C}^{ep}:\boldsymbol{M}^{-1}:\frac{\partial \boldsymbol{M}}{\partial \boldsymbol{D}^T}:\frac{\partial F_d}{\partial(-\boldsymbol{Y})}\right]:\boldsymbol{C}^{e-1}\right\}:\boldsymbol{\sigma}\frac{\partial F_d}{\partial \boldsymbol{\sigma}^T}\tag{3.113}$$

Where

$$\frac{\partial F_d}{\partial \boldsymbol{\sigma}^T}=\left\{\frac{\boldsymbol{Y}^T:\boldsymbol{N}}{2Y_{eq}}\right\}\left(\boldsymbol{X}^s:\boldsymbol{\sigma}\right)\tag{3.114}$$

$$=\frac{1}{2Y_{eq}}\left\{Y_1+\mu Y_2,Y_2+\mu Y_1,2(1-\mu)Y_6\right\}\begin{bmatrix}\frac{-2\sigma_1}{(1-D_1)^3e_0} & \frac{-2\nu\sigma_6}{(1-D_1)^2(1-D_2)e_0}\\ \frac{2\nu\sigma_1}{(1-D_1)^2(1-D_2)e_0} & \frac{2\nu\sigma_6}{(1-D_1)(1-D_2)^2e_0}\\ \frac{-2(1+\nu)\sigma_6}{(1-D_1)^2(1-D_2)e_0} & \frac{-2(1+\nu)\sigma_2}{(1-D_1)(1-D_2)^2e_0}\\ \frac{2\nu\sigma_6}{(1-D_1)^2(1-D_2)e_0} & \frac{2\nu\sigma_2}{(1-D_1)(1-D_2)^2e_0}\\ \frac{-2\nu\sigma_6}{(1-D_1)(1-D_2)^2e_0} & \frac{-2\sigma_2}{(1-D_1)^3e_0}\\ \frac{-2(1+\nu)\sigma_2}{(1-D_1)(1-D_2)^2e_0} & \frac{-2(1+\nu)\sigma_6}{(1-D_1)(1-D_2)^2e_0}\end{bmatrix}$$

$$= \begin{bmatrix} \dfrac{\partial F_d}{\partial \sigma_{11}} & \dfrac{\partial F_d}{\partial \sigma_{12}} \\ \dfrac{\partial F_d}{\partial \sigma_{21}} & \dfrac{\partial F_d}{\partial \sigma_{22}} \end{bmatrix} \tag{3.115}$$

Where

$$\frac{\partial F_d}{\partial \sigma_{11}} = \frac{1}{Y_{eq} e_0}\left(\frac{-\sigma_1 (Y_1 + \mu Y_2)}{(1-D_1)^3} + \frac{2\nu\sigma_1(\mu Y_1 + Y_2)}{(1-D_1)^2(1-D_2)} - \frac{2(1-\mu)(1+\nu)\sigma_6 Y_6}{(1-D_1)^2(1-D_2)} \right) \tag{3.116}$$

$$\frac{\partial F_d}{\partial \sigma_{12}} = \frac{1}{Y_{eq} e_0}\left(-\frac{\sigma_6 (Y_1 + \mu Y_2)}{(1-D_1)^2(1-D_2)} + \frac{\nu\sigma_6(\mu Y_1 + Y_2)}{(1-D_1)(1-D_2)^2} - \frac{2(1-\mu)(1+\nu)\sigma_2 Y_6}{(1-D_1)(1-D_2)^2} \right) \tag{3.117}$$

$$\frac{\partial F_d}{\partial \sigma_{21}} = \frac{1}{Y_{eq} e_0}\left(\frac{\nu\sigma_6 (Y_1 + \mu Y_2)}{(1-D_1)^2(1-D_2)} - \frac{\sigma_6(\mu Y_1 + Y_2)}{(1-D_1)(1-D_2)^2} - \frac{2(1-\mu)(1+\nu)\sigma_1 Y_6}{(1-D_1)(1-D_2)^2} \right) \tag{3.118}$$

$$\frac{\partial F_d}{\partial \sigma_{22}} = \frac{1}{Y_{eq} e_0}\left(\frac{\nu\sigma_2 (Y_1 + \mu Y_2)}{(1-D_1)(1-D_2)^2} + \frac{\sigma_2(\mu Y_1 + Y_2)}{(1-D_2)^3} - \frac{2(1-\mu)(1+\nu)\sigma_6 Y_6}{(1-D_1)(1-D_2)^2} \right) \tag{3.119}$$

$$\begin{aligned} \frac{\partial F_d}{\partial (-\boldsymbol{Y})} &= -\frac{\partial F_d}{\partial \boldsymbol{Y}} = -\left\{ \frac{\partial F_d}{\partial Y_1}, \frac{\partial F_d}{\partial Y_2}, \frac{\partial F_d}{\partial Y_6} \right\}^T \\ &= -\left(\frac{\partial F_d}{\partial Y_{eg}} \right)\left(\frac{\partial Y_{eq}}{\partial Y^T} \right) = \frac{\boldsymbol{Y}^T : \boldsymbol{N}}{2Y_{eg}} \\ &= -\frac{1}{2Y_{eg}}\left[Y_1 + HY_2, Y_2 + HY_1, 2(1-H)Y_6 \right]^T \end{aligned} \tag{3.120}$$

$$\left\{\frac{\partial F_d}{\partial \boldsymbol{D}^T}\right\}=\left\{\frac{\partial F_d}{\partial D_{11}},\frac{\partial F_d}{\partial D_{22}},\frac{\partial F_d}{\partial D_{12}}\right\}$$

$$=\left\{\left\{\frac{\partial F_d}{\partial \boldsymbol{Y}^T}\right\}\left\{\frac{\partial \boldsymbol{Y}}{\partial D_{11}}\right\},\left\{\frac{\partial F_d}{\partial \boldsymbol{Y}^T}\right\}\left\{\frac{\partial \boldsymbol{Y}}{\partial D_{22}}\right\},\left\{\frac{\partial F_d}{\partial \boldsymbol{Y}^T}\right\}\left\{\frac{\partial \boldsymbol{Y}}{\partial D_{12}}\right\}\right\} \tag{3.121}$$

$$=\left\{\frac{\partial F_d}{\partial \boldsymbol{Y}^T}\right\}\begin{Bmatrix}\frac{\partial Y_{11}}{\partial D_{11}} & \frac{\partial Y_{11}}{\partial D_{22}} & \frac{\partial Y_{11}}{\partial D_{12}}\\ \frac{\partial Y_{22}}{\partial D_{11}} & \frac{\partial Y_{22}}{\partial D_{22}} & \frac{\partial Y_{22}}{\partial D_{12}}\\ \frac{\partial Y_{12}}{\partial D_{11}} & \frac{\partial Y_{12}}{\partial D_{22}} & \frac{\partial Y_{12}}{\partial D_{12}}\end{Bmatrix}$$

Where $\frac{\partial \boldsymbol{Y}}{\partial \boldsymbol{D}}$ can be obtained from the equation (22) in (Chow and Jie 2004).

Noted that

$$\frac{\partial F_d}{\partial(-\boldsymbol{Y})^T}=-\frac{\partial F_d}{\partial \boldsymbol{Y}^T}$$

$$=-\left(\frac{\partial F_d}{\partial Y_{eq}}\right)\left(\frac{\partial Y_{eq}}{\partial \boldsymbol{Y}^T}\right)$$

$$=-\frac{1}{2Y_{eq}}\left(Y_1+\mu Y_2,\quad \mu Y_1+Y_2,\quad 2(1-\mu)Y_6\right) \tag{3.122}$$

The $\left\{\frac{\partial F_d}{\partial \boldsymbol{D}^T}\right\}$ then can be computed

$$\alpha=\left[\frac{\partial C}{\partial Z}-\frac{\partial F_d}{\partial(-\boldsymbol{Y}^T)}:\frac{\partial(-\boldsymbol{Y})}{\partial \boldsymbol{D}^T}:\frac{\partial F_d}{\partial(-\boldsymbol{Y})}\right]^{-1}$$

$$=\left[\frac{\partial C}{\partial Z}+\left\{\frac{\partial F}{\partial \boldsymbol{Y}^T}\right\}\left[\frac{\partial \boldsymbol{Y}}{\partial \boldsymbol{D}^T}\right]\left\{\frac{\partial F_d}{\partial \boldsymbol{Y}}\right\}\right]^{-1}$$

$$= \left[\frac{\partial C}{\partial Z} + \frac{1}{4Y_{eq}^{\ 2}} \begin{Bmatrix} Y_1 + \mu Y_2 \\ \mu Y_1 + Y_2 \\ 2(1-\mu)Y_6 \end{Bmatrix}^T \begin{bmatrix} \frac{\partial Y_{11}}{\partial D_{11}} & \frac{\partial Y_{11}}{\partial D_{22}} & \frac{\partial Y_{11}}{\partial D_{12}} \\ \frac{\partial Y_{22}}{\partial D_{11}} & \frac{\partial Y_{22}}{\partial D_{22}} & \frac{\partial Y_{22}}{\partial D_{12}} \\ \frac{\partial Y_{12}}{\partial D_{11}} & \frac{\partial Y_{12}}{\partial D_{22}} & \frac{\partial Y_{12}}{\partial D_{12}} \end{bmatrix} \begin{Bmatrix} Y_1 + \mu Y_2 \\ \mu Y_1 + Y \\ 2(1-\mu)Y \end{Bmatrix} \right]^{-1}$$

(3 .123)

Where $\frac{\partial \boldsymbol{Y}}{\partial \boldsymbol{D}}$ can be obtained from the equation (22) in (Chow and Jie 2004)

$$\boldsymbol{A} = \boldsymbol{I} + \alpha \left\{ \frac{\partial \boldsymbol{M}}{\partial \boldsymbol{D}^T} : \frac{\partial F_d}{\partial(-\boldsymbol{Y})} : \boldsymbol{M}^{-1} + \left[\boldsymbol{C}^{ep} : \boldsymbol{M}^{-1} : \frac{\partial \boldsymbol{M}}{\partial \boldsymbol{D}^T} : \frac{\partial F_d}{\partial(-\boldsymbol{Y})} \right] : \boldsymbol{C}^{e-1} \right\} : \boldsymbol{\sigma} \frac{\partial F_d}{\partial \boldsymbol{\sigma}^T} \qquad (3.124)$$

Where

$$\frac{\partial \boldsymbol{M}}{\partial \boldsymbol{D}^T} = \left[\frac{\partial \boldsymbol{M}}{\partial D_{11}} \quad \frac{\partial \boldsymbol{M}}{\partial D_{22}} \quad \frac{\partial \boldsymbol{M}}{\partial D_{12}} \right] \qquad (3.125)$$

$$\frac{\partial \boldsymbol{M}}{\partial D_{11}} = -\frac{1}{2} \boldsymbol{M} : \frac{\partial \boldsymbol{P}}{\partial D_{11}} : \boldsymbol{M}^2 \qquad (3.126)$$

Where, $\frac{\partial \boldsymbol{P}}{\partial D_{11}}$ can be obtained from the Appendix A. in (Chow and Jie 2004).

And note that $D_{12} = D_{21} = 0$, the following can be obtained

$$\frac{\partial \boldsymbol{M}}{\partial D_{11}} = -\frac{1}{2}\begin{bmatrix} \frac{1}{1-D_1} & 0 & 0 \\ 0 & \frac{1}{1-D_2} & 0 \\ 0 & 0 & \frac{1}{\sqrt{(1-D_1)(1-D_2)}} \end{bmatrix}\begin{bmatrix} -2(1-D_1) & 0 & 0 \\ 0 & 0 & 0 \\ 0 & 0 & -1+D_2 \end{bmatrix}\left[\boldsymbol{M}^2\right]$$

$$= -\frac{1}{2}\begin{bmatrix} -2 & 0 & 0 \\ 0 & 0 & 0 \\ 0 & 0 & \frac{-1+D_2}{\sqrt{(1-D_1)(1-D_2)}} \end{bmatrix}\begin{bmatrix} \frac{1}{(1-D_1)^2} & 0 & 0 \\ 0 & \frac{1}{(1-D_2)^2} & 0 \\ 0 & 0 & \frac{1}{(1-D_1)(1-D_2)} \end{bmatrix}$$

$$= -\frac{1}{2}\begin{bmatrix} -2 & 0 & 0 \\ 0 & 0 & 0 \\ 0 & 0 & \frac{-1+D_2}{\sqrt{(1-D_1)(1-D_2)}} \end{bmatrix}\begin{bmatrix} \frac{1}{(1-D_1)^2} & 0 & 0 \\ 0 & \frac{1}{(1-D_2)^2} & 0 \\ 0 & 0 & \frac{1}{(1-D_1)(1-D_2)} \end{bmatrix}$$

$$= \begin{bmatrix} \frac{1}{(1-D_1)^2} & 0 & 0 \\ 0 & 0 & 0 \\ 0 & 0 & \frac{1}{2(1-D_1)^{\frac{3}{2}}(1-D_2)^{\frac{1}{2}}} \end{bmatrix} \tag{3.127}$$

Similar calculation can be performed to obtain follows

$$\frac{\partial \boldsymbol{M}}{\partial D_{12}} = \begin{bmatrix} 0 & 0 & \frac{1}{2(1-D_1)(1-D_2)} \\ 0 & 0 & 0 \\ 0 & \frac{1}{2(1-D_1)^{\frac{1}{2}}(1-D_2)^{\frac{3}{2}}} & 0 \end{bmatrix} \tag{3.128}$$

$$\frac{\partial \boldsymbol{M}}{\partial D_{22}} = \begin{bmatrix} 0 & 0 & 0 \\ 0 & \dfrac{1}{(1-D_2)^2} & 0 \\ 0 & 0 & \dfrac{1}{2(1-D_1)^{\frac{1}{2}}(1-D_2)^{\frac{3}{2}}} \end{bmatrix} \tag{3.129}$$

And

$$\frac{\partial \boldsymbol{M}}{\partial \boldsymbol{D}^T} = \begin{bmatrix} \dfrac{\partial \boldsymbol{M}}{\partial D_{11}} & \dfrac{\partial \boldsymbol{M}}{\partial D_{22}} & \dfrac{\partial \boldsymbol{M}}{\partial D_{12}} \end{bmatrix} \tag{3.130}$$

Then

$$\left[\frac{\partial \boldsymbol{M}}{\partial \boldsymbol{D}^T}\right]\left\{\frac{\partial F_d}{\partial(-\boldsymbol{Y})}\right\} = -\frac{1}{2}\begin{bmatrix} \dfrac{\partial \boldsymbol{M}}{\partial D_{11}} & \dfrac{\partial \boldsymbol{M}}{\partial D_{12}} & \dfrac{\partial \boldsymbol{M}}{\partial D_{22}} \end{bmatrix}\begin{Bmatrix} Y_1+\mu Y_2 \\ \mu Y_1 + Y_2 \\ 2(1-\mu)Y_6 \end{Bmatrix}$$

$$= -\frac{1}{2Y_{eq}}\left[\left[\frac{\partial \boldsymbol{M}}{\partial D_{11}}\right]\begin{Bmatrix} Y_1+\mu Y_2 \\ \mu Y_1 + Y_2 \\ 2(1-\mu)Y_6 \end{Bmatrix} \quad \left\|\frac{\partial \boldsymbol{M}}{\partial D_{22}}\right\|\begin{Bmatrix} Y_1+\mu Y_2 \\ \mu Y_1 + Y_2 \\ 2(1-\mu)Y_6 \end{Bmatrix} \quad \left[\frac{\partial \boldsymbol{M}}{\partial D_{22}}\right]\begin{Bmatrix} Y_1+\mu Y_2 \\ \mu Y_1 + Y_2 \\ 2(1-\mu)Y_6 \end{Bmatrix}\right]$$

$$= -\frac{1}{2Y_{eq}}\begin{bmatrix} \dfrac{Y_1+\mu Y_2}{(1-D_1)^2} & 0 & \dfrac{2(1-\mu)Y_6}{(1-D_1)(1-D_2)} \\ 0 & \dfrac{\mu Y_1 + Y_2}{(1-D_2)^2} & 0 \\ \dfrac{2(1-\mu)Y_6}{2(1-D_1)^{\frac{3}{2}}(1-D_2)^{\frac{1}{2}}} & \dfrac{2(1-\mu)Y_6}{2(1-D_1)^{\frac{1}{2}}(1-D_2)^{\frac{3}{2}}} & \dfrac{\mu Y_1 + Y_2}{2(1-D_1)^{\frac{1}{2}}(1-D_2)^{\frac{3}{2}}} \end{bmatrix} \tag{3.131}$$

Then

$$\left[\frac{\partial \boldsymbol{M}}{\partial \boldsymbol{D}^T}\right]\left\{\frac{\partial F_d}{\partial(-\boldsymbol{Y})}\right\}[\boldsymbol{M}]^{-1} = -\frac{1}{2Y_{eq}}\begin{bmatrix} \frac{Y_1+\mu Y_2}{1-D_1} & 0 & \frac{2(1-\mu)Y_6}{(1-D_1)^{\frac{1}{2}}(1-D_2)^{\frac{1}{2}}} \\ 0 & \frac{\mu Y_1+Y_2}{1-D_2} & 0 \\ \frac{2(1-\mu)Y_6}{2(1-D_1)^{\frac{1}{2}}(1-D_2)^{\frac{1}{2}}} & \frac{2(1-\mu)Y_6}{2(1-D_1)^{\frac{1}{2}}(1-D_2)^{\frac{1}{2}}} & \frac{\mu Y_1+Y_2}{2(1-D_1)} \end{bmatrix} \tag{3.132}$$

The equivalent stress is

$$\bar{\sigma}_{eq} = \left(\frac{1}{2}\bar{\boldsymbol{\sigma}}^T : \boldsymbol{H} : \bar{\boldsymbol{\sigma}}\right)^{\frac{1}{2}} \tag{3.133}$$

As

$$\bar{\boldsymbol{\sigma}} = \begin{Bmatrix} \bar{\sigma}_1 & \bar{\sigma}_2 & \bar{\sigma}_6 \end{Bmatrix}^T \tag{3.134}$$

$$\boldsymbol{H} = \begin{bmatrix} G+H & -H & 0 \\ -H & F+H & 0 \\ 0 & 0 & 2N \end{bmatrix} \tag{3.135}$$

$$\bar{\sigma}_{eq} = \left(\frac{(G+H)\sigma_1^2}{2(1-D_1)^2} + \frac{(F+H)\sigma_2^2}{2(1-D_2)^2} - \frac{H\sigma_1\sigma_2}{(1-D_1)(1-D_2)} + \frac{N\sigma_6}{(1-D_1)(1-D_2)}\right)^{\frac{1}{2}} \tag{3.136}$$

$$\begin{aligned} \frac{\partial F_p}{\partial \bar{\boldsymbol{\sigma}}} &= \frac{\partial F_p}{\partial \bar{\sigma}_{eq}}\frac{\partial \bar{\sigma}_{eq}}{\partial \bar{\boldsymbol{\sigma}}} \\ &= \frac{\bar{\boldsymbol{\sigma}}^T : \boldsymbol{H}}{2\bar{\sigma}_{eq}} \\ &= \frac{1}{2\bar{\sigma}_{eq}}\begin{Bmatrix} (G+H)\bar{\sigma}_1 - H\bar{\sigma}_2 \\ (F+H)\bar{\sigma}_2 - H\bar{\sigma}_1 \\ 2N\bar{\sigma}_6 \end{Bmatrix} \end{aligned} \tag{3.137}$$

As

$$\boldsymbol{C}^e = \frac{e_0}{1-\nu^2}\begin{bmatrix} 1 & \nu & 0 \\ \nu & 1 & 0 \\ 0 & 0 & \dfrac{1-\nu}{2} \end{bmatrix} \tag{3.138}$$

Then

$$\left[\boldsymbol{C}^e\right]\left\{\frac{\partial F_p}{\partial \overline{\boldsymbol{\sigma}}}\right\} = \frac{e_0}{2\overline{\sigma}_{eq}(1-\nu^2)}\begin{Bmatrix} (G+H)\overline{\sigma}_1 + \nu(F+H)\overline{\sigma}_2 - H(\overline{\sigma}_2 + \nu\overline{\sigma}_1) \\ \nu(G+H)\overline{\sigma}_1 + (F+H)\overline{\sigma}_2 - H(\nu\overline{\sigma}_2 + \overline{\sigma}_1) \\ (1-\nu)N\overline{\sigma}_1 \end{Bmatrix} \tag{3.139}$$

Similarly

$$\left\{\frac{\partial F_p}{\partial \overline{\boldsymbol{\sigma}}^T}\right\}\left[\boldsymbol{C}^e\right] = \frac{e_0}{2\overline{\sigma}_{eq}(1-\nu^2)}\begin{Bmatrix} (G+H)\overline{\sigma}_1 + \nu(F+H)\overline{\sigma}_2 - H(\overline{\sigma}_2 + \nu\overline{\sigma}_1) \\ \nu(G+H)\overline{\sigma}_1 + (F+H)\overline{\sigma}_2 - H(\nu\overline{\sigma}_2 + \overline{\sigma}_1) \\ (1-\nu)N\overline{\sigma}_1 \end{Bmatrix}^T \tag{3.140}$$

Then

$$\left[\left[\boldsymbol{C}^e\right]\left\{\frac{\partial F_p}{\partial \overline{\boldsymbol{\sigma}}}\right\}\right]\left[\left\{\frac{\partial F_p}{\partial \overline{\boldsymbol{\sigma}}^T}\right\}\left[\boldsymbol{C}^e\right]\right] = \frac{e_0^2}{4\overline{\sigma}_{eq}{}^2(1-\nu^2)^2}\begin{bmatrix} V_1^2 & V_1V_2 & V_1V_3 \\ & V_2^2 & V_2V_3 \\ S & & V_3^2 \end{bmatrix} \tag{3.141}$$

Where

$$V_1 = (G+H)\overline{\sigma}_1 + \nu(F+H)\overline{\sigma}_2 - H(\overline{\sigma}_2 + \nu\overline{\sigma}) \tag{3.142}$$

$$V_2 = \nu(G+H)\overline{\sigma}_1 + (F+H)\overline{\sigma}_2 - H(\nu\overline{\sigma}_2 + \overline{\sigma}) \tag{3.143}$$

$$V_3 = (1-\nu)N\overline{\sigma}_1 \tag{3.144}$$

$$\beta = \left(\frac{\partial T}{\partial p} + \frac{\partial F_p}{\partial \overline{\overline{\boldsymbol{\sigma}}}^T} : \boldsymbol{C}^e : \frac{\partial F_p}{\partial \overline{\overline{\boldsymbol{\sigma}}}} \right)^{-1}$$

$$= \left(\frac{\partial T}{\partial p} + \frac{e_0^2}{4\overline{\sigma}_{eq}{}^2 (1-\nu^2)^2} \left(V_1^2 + V_2^2 + V_3^2 \right) \right)^{-1} \tag{3.145}$$

Put (3.145), (3.141) into following

$$\boldsymbol{C}^{ep} = \boldsymbol{C}^e - \beta \left(\boldsymbol{C}^e : \frac{\partial F_p}{\partial \overline{\overline{\boldsymbol{\sigma}}}} \right) \left(\frac{\partial F_p}{\partial \overline{\overline{\boldsymbol{\sigma}}}^T} : \boldsymbol{C}^e \right) \tag{3.146}$$

Put (3.146) into (3.113) **A** can be obtained. Put (3.112), (3.113) and (3.146) into equation (25) in Chow and Jie 2004, $\overline{\boldsymbol{C}}^{ep}$ can be calculated.

$$\overline{\boldsymbol{C}}^{ep} = \boldsymbol{M}^{-1} : \boldsymbol{A}^{-1} : \boldsymbol{C}^{ep} : \boldsymbol{M}^{-1}$$

Chapter 4 Numerical Simulations

4.1 Finite element failure analysis

In the traditional hydroforming process, the tryouts and gradually modification of process are based on practical tryout. Much time and financial investment are required in achieving this work. Furthermore, both the material property and the deformation of the components during THF process are nonlinear which makes it impossible to obtain analytic solutions. In order to study the different characteristics during the process and validate the proposed design, the finite element method has been developed and used widely since the late 1960s.

Commercial FEM software packages, such as LS-DYNA, DEFORM ANASYS, MAC, NASTRAN and ABAQUS, have been used widely in recent decades. These provide feasible methods of dealing with problems in both the pre-process and post process, and provide varies interfaces for the users to implement for special purpose. Using explicit method in LS-DYNA commercial software package, the multi-operation tube hydroforming of a component used in automotive was simulated by Wu and Yu (Wu and Yu, 1996). In 1998, Srinivasan et al. (Srinivasan et al., 1998) and Liu et al. (Liu et

al., 1998) worked on validations of experimental and analytical results using LS-DYNA 3D respectively. In 2002, Kaya et al. (Kaya et al., 2002) worked on the deformation of tube cross section using implicit method in DEFORM 2D. After then, many other researchers have performed lots of numerical analysis with different FEM software on tube hydroforming (Kim et al., 2002,Kim et al., 2002 Hwang and Altan, 2004, Hwang and Altan, 2003, Hsu, 2003, Fann and Hsiao, 2003, Corona, 2004, Aue-U-Lan et al., 2004, Kulkarni et al., 2004, Papelnjak, 2004, Hama et al., 2004a, Hama et al., 2004b, Hama et al., 2003, Lin and Kwan, 2004, Imaninejad et al., 2004, Ray and Mac Donald, 2004, Johnson et al., 2004, Kim and Kang, 2004, Kim et al., 2004, Kim et al., 2003, Lang et al., 2004b, Aydemir et al., 2005, and Yoon et al., 2006)

The multi-purpose finite element packages ABAQUS is used widely in academic areas because of its strong ability to solve nonlinear problem and its feasible interface for users. In the present study, this was used to simulate the hydroforming process. With the aid of reliable experimental findings (i.e., mechanical properties and damage parameters) the hydroforming behavior of the components can be predicted using the selected constitution models. Meanwhile, the shear criterion is implemented into the software package with which the failure of components is simulated. The simulated results are compared with experimental results to validate the proposed criterion.

For this project, the developed model was put into codes with user defined subroutines. The components in the hydroforming process are a large deformation problem, and the ABAQUS/Explicit was chosen to simulate such a problem. The subroutine used in the study was VUMAT subroutine.

In order to use the present material constitution and the damage coupled shear criterion, a user defined subroutine should be utilized. The explicit method was used in this study, and the VUMAT was used in designing the required subroutine. This chapter describes the implementation of the materials constitution and the failure criterion into user defined material subroutine for ABAQUS using VUMAT. With the aid of the modified finite element code, two kind of THF were simulated, and the results of them are then compared with experimental results for the validation of the proposed theory.

4.2 User-defined material subroutine for ABAQUS

In ABAQUS main software process, strain increments are calculated based on certain stress condition and used as input variables in VUMAT subroutine. With these strain increment, the stresses in each nodes are updated in the subroutine. The yield of the material is tested in the initial stage of each step. If the material yields, the stress will be

updated using effective hardening modulus tensor $\overline{C}^{ep}$, if it is not, the stress is updated using effective elastic modulus tensor $\overline{C}^{e}$. The stress increment and the state variables are updated at the end of each step. The flow chat of the subroutine is shown in Fig 4.1. At each step, the maximum shear stress at each element is compared with the shear criterion. If it is reaches the criterion, it states that a localized necking point appeared in the component and fracture will occur in hydroforming process. Any fracture point will lead to decreasing of internal pressure and the component will not be hydroformed after then. So the state variable (*,11) which is the flag of criterion is set as 1 in this condition. The element will be defined as failure and the program will be ceased.

The main purposes of the VUMAT subroutine include to provide stress updating and to check the deformation condition to test if the localized necking criterion has been reached. There are 11 state variables in the VUMAT subroutine including strain increment, damage increment, equivalent plastic strain, equivalent damage and the flat of the shear stress. The equivalent damage is based on the formulas mentioned in Chapter 3. The state variables are put into the array state (*). These variables are shown in Table 4.1.

State variables	Variable
State (*,1)	New damage components 11
State (*,2)	New damage components 22
State (*,3)	New equivalent plastic strain
State (*,4)	New equivalent damage
State (*,5)	Old damage component 11
State (*,6)	Old damage component 22
State (*,7)	Old equivalent plastic strain
State (*,8)	Old equivalent damage
State (*,9)	Strain component 11
State (*,10)	Strain component 22
State (*,11)	Flat of failure

Table 4.1 State variables used in VUMAT

There were 10 property parameters in the subroutine which can be set in the user defined material tables including: initial Young's modulus and Poisson's ratio, anisotropic parameters, yield stress, damage threshold and shear criterion. The material property variables used in the subroutine are put into array PROP (*) which is shown in Table 4.2.

Property variables	Variable
PROP (1)	Young's modulus of as received material
PROP (2)	Poisson's ratio of as received material
PROP (3)	Anisotropic parameter G
PROP (4)	Anisotropic parameter F
PROP (5)	Anisotropic parameter H
PROP (6)	Anisotropic parameter N
PROP (7)	Damage hardening coefficient η
PROP (8)	Initial yield threshold C(0)
PROP (9)	Initial plastic damage strengthening threshold T(0)
PROP (10)	Shear criterion τ_{cr}

Table 4.2 Material properties used in VUMAT

Element failure method is used in the simulation. There are mainly two methods can be utilized simulate the failure of elements in ABAQUS. One method is direct element removal, with which the removed elements are selected in advance by users based on the locations and special purposes. Another method is the failure test method, a criterion is defined in this method and used to judge if the elements are failure. This method is usually utilized in ABAQUS/Explicit. In this method, a status is used to control the deletion of failure element, when the element is not failing the value of the status variable is “1”, or the value of it is “0” and the element should be deleted. There are two kinds of definitions of the criterion that can be used in this method. The first one is to choose one damage property in the material property table, and the related damage initiation and evolution parameters should also be set. Different variables, such as displacements or energies, are usually used in this method to determine the damage values. When the damage value reaches 1, failure has occurred in the element. The second failure definition method uses VUMAT which was used in the present study. In the subroutine, state (*, 11) is used to express the elements status. When the shear criterion is reached the status variable will be set as 0.

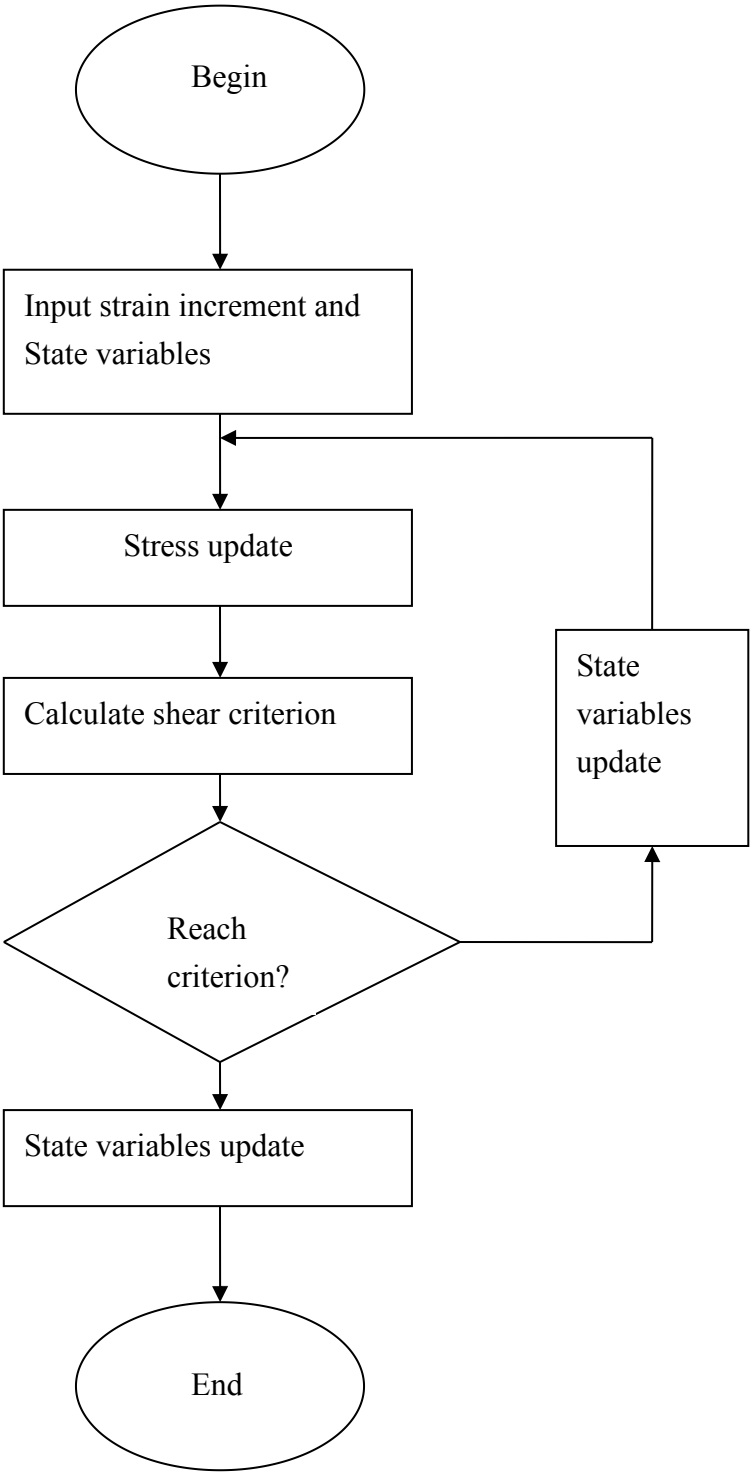

Fig. 4.1 Flow chart of the subroutine

4.3 Numerical simulation of bulging THF components

The geometry model of the material was constructed in ABAQUS/CAE. The part of the model included tube and die. The part of tube was constructed based on the geometry of AA 6063 tubes. Due to the symmetric shape of the tube, the simulation was done on 1/8 part of the tube. The length, diameter and thickness of tube were 120mm, 22.2mm and 1.2mm, respectively. The die was set as discrete rigid. The geometry shape of the die can be referred to Fig 5.1. The element of tube was set as a deformable 3D shell elements with thickness value 1.2 and the C4R element set as the mesh element. The material property was selected as user defined material, by which the VUMAT could be performed during the simulation.

In bulging process, the tubes are deformed by internal pressure with axial force loaded on both ends of tubes. The material in the two sides of tubes will flow into the die cavity freely when the middle parts of tubes are expanded and bulged. Three kinds of combinations of internal pressure and axial force were designed in the present study. In order to validate the proposed criterion for this study the bulging THF processes were simulated. The tooling for the process can be referred in Fig 5.9.

The select loading paths were based on the analysis introduced in Chapter 3.2. The path A, B and C were selected in the bursting region to test the different fracture situation of tubes. During the process, the maximum shear stress was calculated and compared with the shear criterion. If it was equal to or larger than the criterion, the simulation stopped. The stress and strain of the component in the failure step could be obtained from the data file. The related results are discussed in Chapter 6.

Chapter 5 Experiments and Experimental Data Processing

There are three main sections in this chapter. The material and the preparations of specimens are introduced in Section 5.1. In Section 5.2, the equipment and tooling used in the experiments are described. Section 5.3 mentions three different kinds of experiments, which have been cataloged by their purposes and processing procedures. The first group of experiments includes those used to test related material properties, from which the mechanical properties and damage parameters of AA 6063 can be obtained and then be used in the modified theoretical criterion and the corresponding simulation. The second group is the hydroformability test, from which the FLDs of tubes in the hydroforming process can be obtained and then used to compare with the predicted FLDs calculated using the damage coupled shear criterion. The last group of experiments is the tube hydroforming using barrel die, which is used to investigate the fracture conditions and features of AA 6063 tubes in the hydroforming process and to validate the simulation results obtained by using the ABAQUS software package. Related experimental-data processing methods are also introduced in Section 5.3 also, in which a new analytic method is proposed in deducing the damage parameters.

5.1 Material and preparations of specimens

In this study, aluminum alloy AA 6063 tubes were used as the specimen material for all tests and experiments. These tubes are extrusion products and used widely due to their lightweight, high-strength, and fine-corrosion characteristics (Bourget et al. 2009, Dutkiewicz and Litynska 2002). The main chemical composition of AA 6063 as-received tube is shown in Table 5.1.

Chemical composition	Si	Mg	Fe	Cu	Mn	Cr	Ti
Range (%)	0.2-0.6	0.45-0.9	0-0.35	0-0.1	0-0.1	0-0.1	0-0.05

Table 5.1 Chemical composition of AA 6063 (Bourget et al. 2009)

The tubes were cut into 120 mm length for the THF experiments. The diameter and thickness of the tubes were 22.2 mm and 1.2 mm, respectively. Before the tubes were used in the FLDs test, a grid pattern was printed on the surface using the photochemical etching method. The distortion of the grids could be observed and measured after the experiment, and the strain-gradient distribution could be obtained from the grids. The grid system used in the FLDs test included radial grid system (Peng 1985, Peng 1987)

and rectangular grid system (Marciniak 1967), which is usually used to measure plane strain, circular grid system (Keeler 1968).

A circular grid system based on the ISO/FDIS 12004-2 was selected for the present study as shown in Fig. 5.1. According to this standard, the maximum diameter of grids should be:

$$d_{\max} = (1 \sim 2.5) \times \text{thickness} \tag{5.1}$$

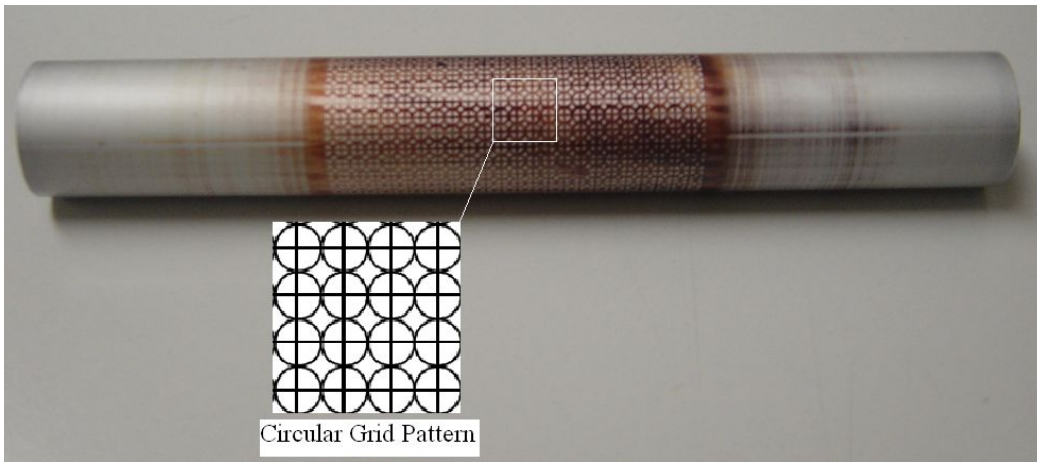

Fig. 5.1 Tube with circular grid system

As the thickness of a tube is 1.2 mm, the diameter of the grid should be between 1.2 mm and 3.0 mm. The smaller grids can be applied to improve the accuracy of the strain measurement. However, when the variation between the deformed grids and the original

grid is very small, the location of the test point determined in the measurement may influence the test accuracy greatly. Then, the test error is increased significantly. The grid size employed in this study was set as D = 2.4 mm. Five steps were applied to print the grids on the tubes:

1. Coating the tubes with the Photo Sensitizer

   Photo Sensitizer film was coated on the tube surface with brush. It should be ensured that the coating film was thin and even. After coating, the tubes were dried in a hot oven for a half minute.

2. Binding the tubes by the transparent grid-pattern film

   After coating the surfaces of the tube, the tubes were bound with a transparent grid-pattern film. The film should be contacted completely on the tube surface without any inter-space.

3. Exposing the tube through the ultraviolet radiation source

   The tube with the pattern film sticking on its surface, was put into an ultraviolet radiation box for about 3 to 5 minutes, the photo sensitizer film would be decomposed by the ultraviolet radiation passing through the grid pattern film.

Finally, grid pattern was identified from decomposed and un-decomposed photo sensitizer film on the tube surface.

4. Soaking the tube in the developer solution

The tube was soaked in developer solution for about 1 minute to make the grid appeared on its surface, and then cleaned with fresh water. The soaking time is very important. If it is too short, the photo sensitizer film cannot be removed completely and the grid cannot appear on the surface of tube completely. On the contrary, if it is too long, the remained photo sensitizer may also be corroded and the grid pattern will be destroyed. All the operations in this step were necessary to avoid touching the destruction of the grids.

5. Coloring the grids with the coloring agent

The coloring agent was dripped onto the surface of tube, with which the grid can be dyed and more clear. After then the tube was sprayed with the water to move away excess agent. Finally, the circular-grid system was printed on the surface of the tube as shown in Fig. 5.1.

5.2 Equipment and tooling

The apparatus used to perform the uniaxial tensile test and uniaxial loading/unloading tensile test was the Material Test System (MTS) 810 as shown in Fig. 5.2. The maximum load capacity of this apparatus is 100 KN. The automatically recorded experimental data included stress and strain. An extensometer was used to test the strain of samples, with a maximum test range of 40%. A user-defined program could be set in the control console of the MTS machine to conduct different experiments.

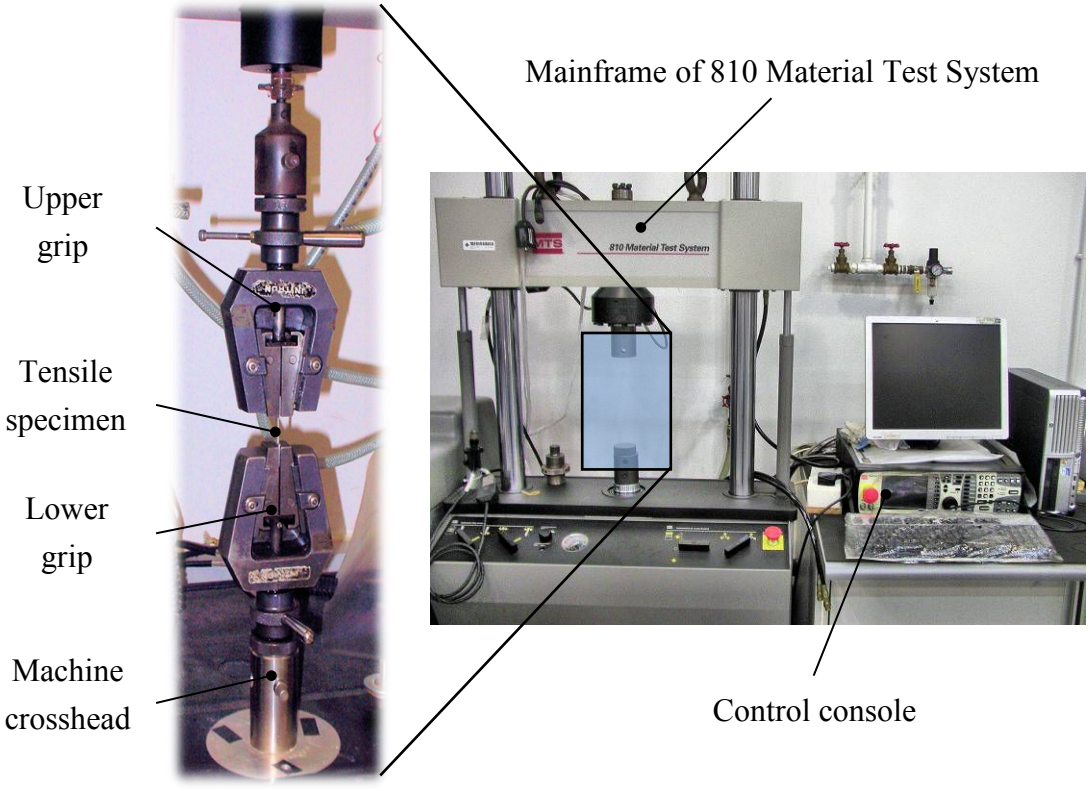

Fig. 5.2 The setup of uniaxial tensile test

A special tailor-made fixture is shown in Fig. 5.3. It was used in the uniaxial tensile test for the tubular specimens, which had been cut along hoop direction of the tube. The fixture was mounted by the upper grip and lower grip of the MTS machine along the load direction. The specimen was placed in the fixture through two semi-round cores, which diameter is designed as the same as sample's out diameter. Indeed, if the hoop-tensile specimen is flattened before being used in the uniaxial tensile test, a pre-strain will occur during the flattening process. The pre-strain may lead to variation of sample's mechanical properties. With using this fixture, the as received hoop-circular specimen can be tested directly on the MTS machine.

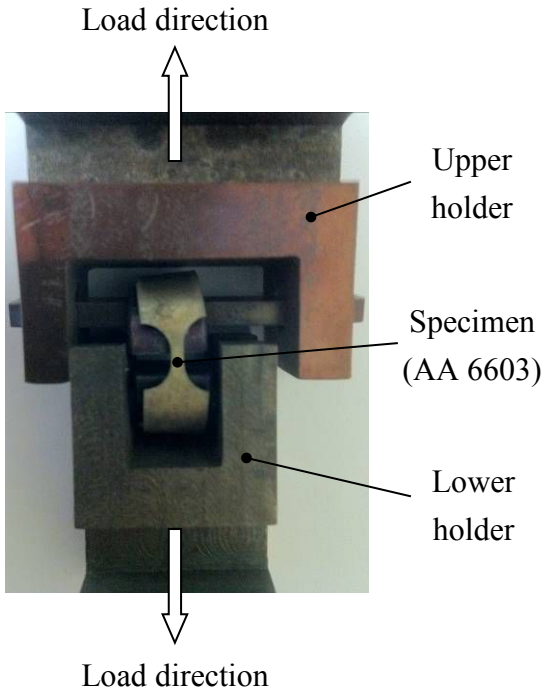

Fig. 5.3 The special tailor-made fixture used in the hoop tensile test

In this study, the tube hydroforming and the test of FLDs for AA 6063 tubes were performed using a self-developed hydroforming system attached to the OMERA 160-ton hydraulic-press machine, which is located in the Hong Kong Polytechnic University. This experimental platform is shown in Fig. 5.4. The hydroforming system was able to provide an ultra-high internal pressure of up to 200 MPa and two axial feedings with maximum displacement of 150mm and maximum force of 550KN. Thus, the tubular specimens could be hydroformed via different loading parameters (or paths).

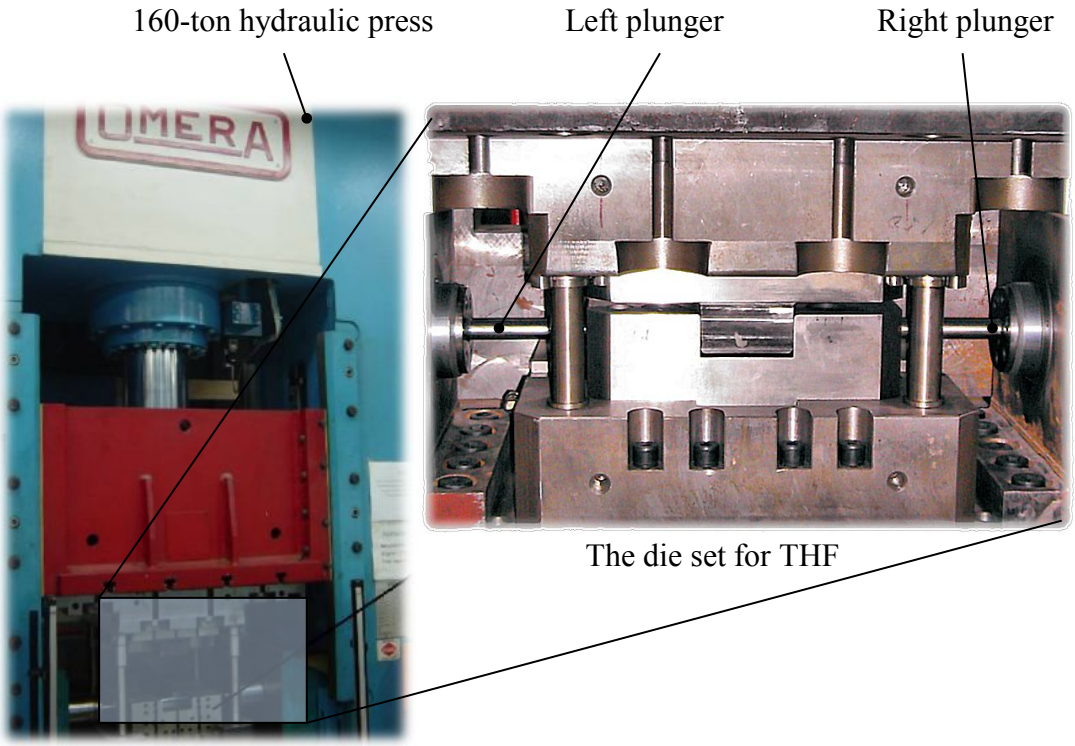

Fig.5.4 The self-developed experimental platform for carrying out the hydroforming

In this tube hydroforming process, a novel composed barrel die was used as illustrated in Fig 5.5. The die assembly consisted of two halves of die cores, which had two recessed pockets for installing various die inserts, and hence the die was able to form different shapes of tubular components when using different die inserts. By this way, the selected inner die inserts could be put into the pockets to achieve the target tube hydroforming conveniently. The barrel-shape inner die inserts were used in this study as shown in Fig 5.5a. It was able to provide a maximum bulging circumference with a diameter of 35 mm. The hydroformed component was located at the nearly middle part of the die in the experiments.

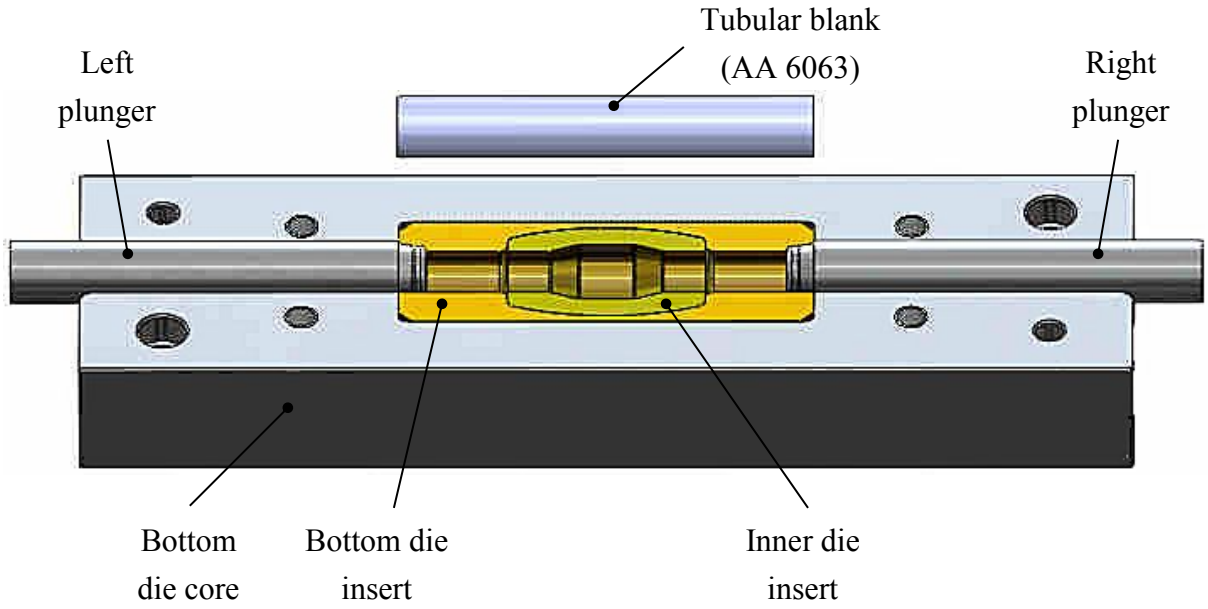

(a) Setup of the bottom die for combine die set

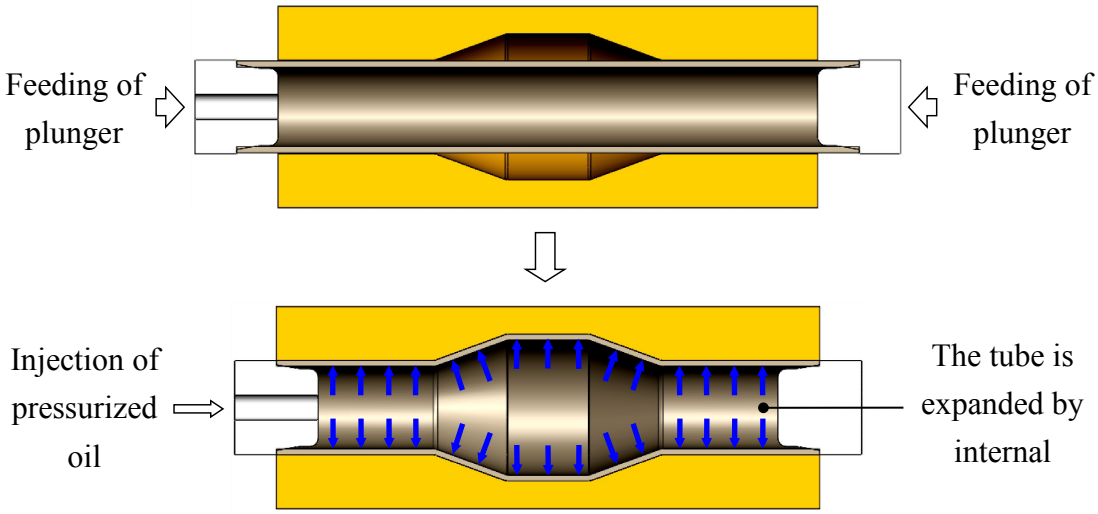

(b) Operations of the THF

Fig. 5.5 The tooling setup and operations of THF

5.3 Tests and hydroforming

Five experiments were conducted using the MTS machine. The procedures of the uniaxial tensile test and the method of acquiring material properties are described In section 5.3.1. The anisotropic variables were determined from the uniaxial tensile test using two types of specimens, which were cut along the axial and hoop directions respectively, as presented in Section 5.3.2. The damage parameters were determined from degrading feature of mechanical property parameters, obtained from the loading-unloading tensile test as introduced in Section 5.3.3. The data processing methods are described in details in Section 5.3.3. Meanwhile, a new analytical method for deducing the damage parameters is also given The experimental details about the tube hydroforming are covered in Sections 5.3.4 and 5.3.5, with the test of FLDs, experimental results were obtained by THF with using three different loading paths.

5.3.1 Uniaxial tensile test of AA 6063

The material properties of the AA 6063 tubes were investigated using the uniaxial tensile test. The specimens were cut from the raw AA 6063 tubes along the axial (longitudinal) direction. The dog bone shape was adopted for the specimens. The dimensions of the specimens are shown in Fig. 5.6.

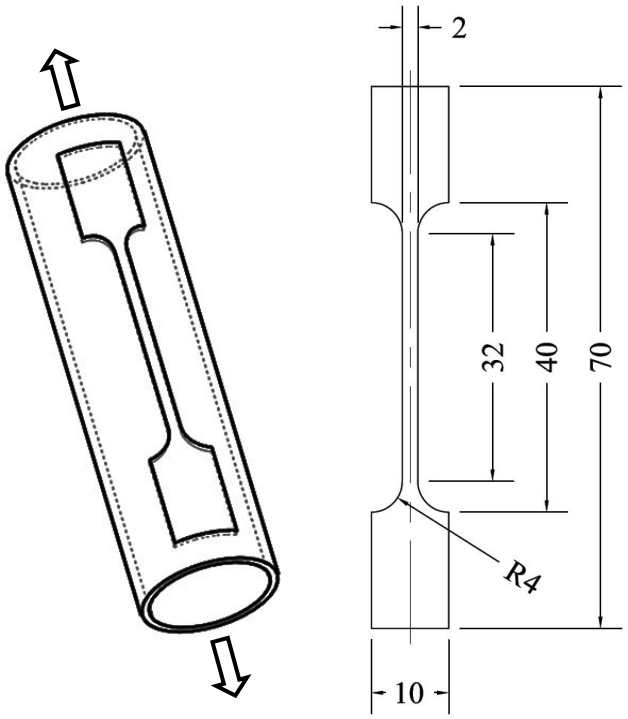

Fig. 5.6 Dimensions of the tensile specimen cut along the longitudinal direction.

The displacement-control loading type was set in the uniaxial tensile test. The displacement rate was set as 0.1 mm/min. The extensometer was used between the strain ranges from 0 to 30%; when the deformation of the specimens was over the range, the extensimeter was reset to zero and repeated the test again.

The original recording data from the MTS machine were engineering strain and stress. The true strain (logarithmic strain) ε was computed from the recorded data as follows:

$$\varepsilon = \ln(1+e) \tag{5.2}$$

Where e is the recorded engineering strain. The ε in later stage should be added by the final value of the previous stage due to the reset of the extensometer.

The true stress can be computed using the original recorded engineering stress and strain as follows:

$$\sigma = \sigma_0(1+e) \tag{5.3}$$

Where σ_0 is the recorded engineering stress.

In order to obtain the plastic strain p, the elastic strain should be uncoupled from the total strain as follows:

$$p = \varepsilon - \frac{\sigma}{E} \tag{5.4}$$

The strain hardening increment can be obtained,

$$T(p) = \sigma_{eq} - T_0 \tag{5.5}$$

Where $\sigma_{eq} = \sigma$ in the uniaxial tensile test and T_0 can be obtained from the $\sigma - \varepsilon$ curve.

5.3.2 Test of anisotropic parameters

Due to the different stress conditions that the tubes endured during the extrusion process, their properties along the hoop direction and axial direction were different. Orthotropic anisotropic plasticity is reasonable to be assumed as the tube's property. In order to obtain the related anisotropic plasticity parameters, experiments were performed to test the properties of tubes in two directions. The experiments were conducted using MTS 810 with which the designed force was loaded on axial direction. Two specimens were cut from the original tubes along longitudinal direction and hoop direction. The hoop direction of the tube was defined as direction 0°, and the longitudinal direction of the tube as the direction 90°. The dog bone shape was adopted for the both kinds of the specimens. The dimensions of 0° specimen and 90° specimen are shown in Fig. 5.7. The main objective of the uniaxial tensile test conducted on two kinds of specimens was to investigate different features in width direction and thickness direction when the tube enduring plastic deformation under axial loading.

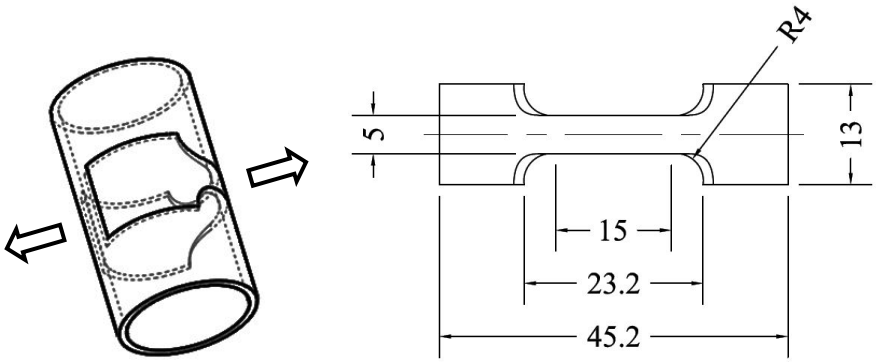

Fig. 5.7 Dimensions of the tensile specimen cut along the hoop direction.

The anisotropic plasticity parameter R which was usually used to describe the plastic property is deduced from width value and thickness value tested in plastic deformation stage. In order to test more data, the uniaxial tensile tests were performed on the specimens with several pause points after the material were yield. The pause points were selected based on the observed engineering strain. Strain was tested in the middle part of specimens. When the engineering strain reached 2%, 4%, 6%, 8%, 10%, 12% and 14%, the tensile test was manually paused. Then, the widths and the thicknesses of the specimens at the test point were measured. Initial value of width and thickness should be measured before the test.

The axial direction, transverse direction, and thickness direction of specimens were defined as direction 1, direction 2, and direction 3, respectively. The related strains

tested in these directions were then defined as ε_1, ε_2 and ε_3. ε_1 is tested using extensometer, ε_2 is calculated using the measured width values as follows:

$$\varepsilon_2 = \ln \frac{w}{w_0} \tag{5.6}$$

Where w_0 is the initial width value, w is the width value measured in pause points.

ε_3 is calculated using the measured thickness value as follows:

$$\varepsilon_3 = \ln \frac{t}{t_0} \tag{5.7}$$

Where t_0 and t are the initial thickness value and measured thickness value in pause points.

The anisotropic plasticity parameter along the direction 0° was computed using the data tested from 0° specimens:

$$R_0 = \frac{\varepsilon_2}{\varepsilon_3} \tag{5.8}$$

There were 5 points (stages) paused during the experiment. The ε_2 and ε_3 at each pause points were calculated, with which the values of R_0 at pause points could also be obtained. The average of these measured values was used to represent R_0 of the material along direction 0°.

Similarly, the anisotropic plasticity parameter along the direction 90° and 45° were computed using the data tested from the 90° and 45° specimens as follows:

$$R_{90} = \frac{\varepsilon_2^{'}}{\varepsilon_3^{'}} \tag{5.9}$$

$$R_{90} = \frac{\varepsilon_2^{'}}{\varepsilon_3^{'}}$$

where $\varepsilon_2^{'}$ and $\varepsilon_3^{'}$ are strain along width direction and thickness direction tested in the 90° specimens. $\varepsilon_2^{'}$ and $\varepsilon_3^{'}$ are strain along width direction and thickness direction tested in the 45° specimens. There were 7 points (stages) had been paused during the experiment when using 90° specimens and 5 points when using 45° specimens. The average value of R_{90} and R_{90} were obtained. The related results and the calculation of the experimental data will be described in chapter 6.

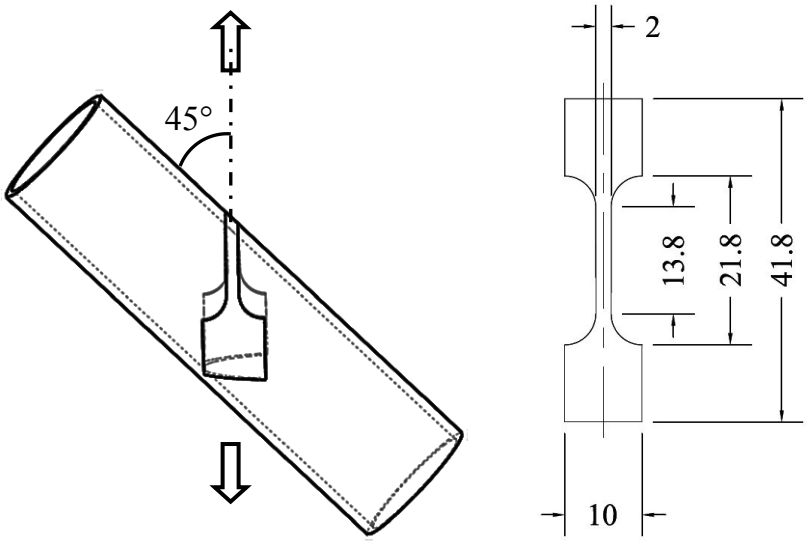

Fig. 5.8 Dimensions of the tensile specimen cut along the 45° direction

5.3.3 Loading-unloading experiment

The damage parameters of the AA 6063 were computed from the related data tested in the loading-unloading experiments. Based on the anisotropic damage theory, it was anticipated that the degradation of the material would lead to a decrease of Young's modulus. In order to investigate the damage evolution of AA6063 tubes, the loading-unloading experiments were conducted to test Yong's modulus after it endured gradually increased tensile loading. The tensile force was loaded on the specimens till its strain reaches pause values. The specimens were then unloaded, after which the tensile force are loaded again. This procedure has been repeated for each pause points. Extensometer is utilized in the experiments. Several upward and downward slope lines have been obtained from stress and strain curves recorded in loading-unloading process. Upward lines are produced in loading stages and downward lines in unloading stages. Young's module was calculated from each downward line. Declined trend was found in Young's module values corresponding to the increase of tensile forced. By studying the decline fo Young's modules, related damage parameter were derived. The experimental results and the analysis of the experimental data will be presented in Section 6.1.

In the loading-unloading experiments, the loading type was set as displacement-control. The displacement rate was 0.1 mm/min. The unloading type was set as force-control.

The force rate was set as -0.03 KN/s. In order to obtain reliable variation of the elastic modulus during the plastic deformation, as more as possible of pause points were selected based on the plastic deformation. The pause points were set by dividing the largest engineering strain into several sections such as 0.3%, 2%, 4%, 6%, 8%, 10%, 12% and 14%. The loading process was paused at each pause point, after then the unloading process started. The engineering stress and engineering strain were recorded by the MTS 810 automatically.

The effective elastic moduli $\overline{E}$ at different unloading stages were computed and the corresponding $\sigma - \overline{E}$ relation is shown in Fig. 6.4; a regression line was constructed to describe the relationship between Young's modulus and the loading stress. The regression function of the $\overline{E}$ is,

$$\overline{E} = \overline{E}(\sigma) \tag{5.10}$$

Then effective Young's modulus which was used later for the calculation of the damage parameters could be determined conveniently by using this regression function.

After $\overline{E}$ being deduced, the damage variables were calculated based on the hypothesis of elastic energy equivalence as follows:

$$D = 1 - \sqrt{\frac{\overline{E}}{E}} \tag{5.11}$$

Then, the elastic strain energy release rate can be computed as follows:

$$Y_1 = -\frac{\sigma_1^{\,2}}{E(1-D_1)} \tag{5.12}$$

Where $D_1 = D$, in the uniaxial tensile test condition. The other components of the elastic strain energy release rate are:

$$Y_2 = 0 \tag{5.13}$$

$$Y_3 = 0 \tag{5.14}$$

The equivalent elastic strain energy release rate can be computed as follows:

$$Y_{eq} = \left(\frac{1}{2} Y^T : N : Y\right)^{\frac{1}{2}} = -\frac{Y_1}{\sqrt{2}} = \frac{\sigma_1^{\,2}}{\sqrt{2}E(1-D_1)^3} \tag{5.15}$$

The damage variable *D* in as-received material was assumed to be zero. As the elastic modulus was found to be varied after the yield point, the damage was assumed to be initiated after the material yielded. The yield stress was assumed as the threshold stress for material damage and was used to calculate the initial plastic damage strengthening threshold as follows:

$$C_0 = -\frac{\sigma_y^2}{\sqrt{2}E} \tag{5.16}$$

The damage surface of the material which was proposed by Chow et al, in the anisotropy damage theory, is expressed using an equation analog the plastic yield surface as follows:

$$F_d = Y_{eq} - \left[C(Z) + C_0\right] = 0 \tag{5.17}$$

From which the damage strengthening function can be obtained as follows:

$$C(Z) = Y_{eq} - C_0 = \frac{\sigma_1^{\,2}}{\sqrt{2}E(1-D_1)^3} - C_0 \tag{5.18}$$

It is noted that, the overall damage under uniaxial tensile load can be obtained as follows:

$$Z = \sqrt{2}D_1 \tag{5.19}$$

Then,

$$C(Z) = \frac{2\sigma_1^{\,2}}{E(\sqrt{2}-Z)^3} - C_0 \tag{5.20}$$

Form the $\sigma_1 - \overline{E}$ relationship, and noted that,

$$\overline{E} = (1-D_1)^2 E \tag{5.21}$$

σ_1 can be expressed using variable D_1 as follows:

$$\sigma_1 = \sigma_1(Z) \tag{5.22}$$

Put the equation into (5.20)

$$C(Z) = \frac{2\sigma_1^{\,2}(Z)}{E(\sqrt{2}-Z)^3} - C_0 \tag{5.23}$$

The proposed analytic method in describing the $C-Z$ relationship was different from the regression method used before.

5.3.4 Test of FLD in tubular hydroforming process

The conventional method of measuring FLDs is to find out the principal strains of sheets in standard tests. This can be used to measure the forming limit with strain ratio covering both of RHS and LHS of strain diagram. The deformation mode can be achieved from uniaxial tension ($\beta = -\frac{1}{2}$) to equal biaxial tension ($\beta = 1$) in the test. The circular specimens, dog bone specimens and rectangular specimens are usually used in the test. When the geometry of the specimen and the lubricant of the die used in the experiment are adjusted, the resulted strain ratio of the specimen would be varied.

However, the stress state generated in the tubular hydroforming could not be exactly the same with the stress state existing in stamping process. Moreover, the tubes used in the hydroforming are manufactured by the extrusion process, and thus the mechanical properties of them were usually different from that of the same metal sheets. Therefore, some researchers have proposed that the formability of the components determined by the hydroforming process is the only completely reliable aid for designing the

hydroforming process and related components (Asnafi and Skogsgårdh 2000). In order to obtain an effective realization and reliable experiment data on the formability of AA 6063 tubes, a FLDs test was done in this study by using the hydroforming experiment platform. The preparations of specimens were introduced in Section 5.1.

5.3.5 Experiment of hydroforming process

The main purpose of the experiment was to investigate the maximum elongation of the tubes under different loading conditions, and to validate the reliability of the proposed shear criterion. Axisymmetric bulging experiments were conducted using the hydroforming system described in Section 5.3. Both the internal pressure and the axial feeding force were provided by the hydroforming system. The axial forces should be large enough to seal the open ends of the tubes. Meanwhile, it should push materials of the tube into the die cavity.

The apparatus and specimens used in the experiment were introduced in Sections 5.1 and 5.2. The die used in the experiment was shown in Fig. 5.5. Servo valves were used to control the displacement of axial feeding as well as the internal pressure, with which designed proportional loading paths could be achieved.

The loading path in the present experiment was a combination of axial forces and internal pressure. The internal pressure was applied to the tubes on their internal surfaces. The pressure was designed to meet several requirements including (koc 1999):

1. At the beginning of forming, it should be large enough to avoid buckling or wrinkling produced by excessive axial force.

2. At the beginning of deformation, it should be high enough to generate the plastic deformation of the tubes, so it should produce a stress that was larger than the yield strength of the material.

3. At the calibration stage, it should be high enough to drive the material into the die cavity. However, this value was difficult to be determined due to a number of factors, which might affect the calibrated results.

The axial force in hydroforming is usually used to drive the material into the expansion regions, with which the thinning in the expansion regions can be compensated. There were certain requirements for setting the axial force in the tubular hydroforming process (Koc 1999):

1. At the beginning of the process, enough sealing force should be provided to counteract the internal pressure.

2. During the process, the force should be high enough to overcome the resistance of the friction referred as the shear friction stress. That friction occurred between the tubes and die surfaces.

3. Finally, the axial force should large enough to generate the deformation of tube wall.

In the tube bulging experiment, the purpose was to obtain the maximum deformation instead of making a well-formed product in calibration stage. The internal pressure and axial forces could be adjusted in a comparable simple way. The combination of the pressure and forces was located in the bursting region in the loading window. Three loading paths are used in the experiments which shown in Fig. 5.9.

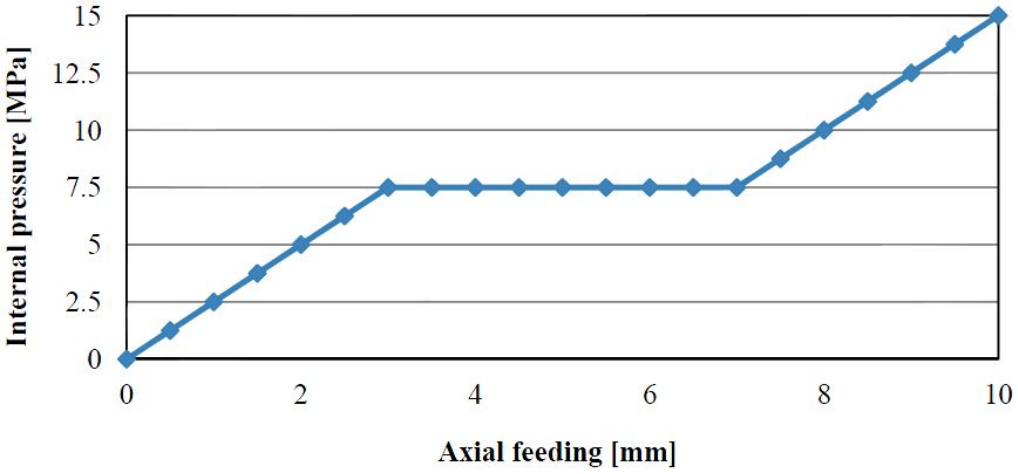

(a) Loading path A

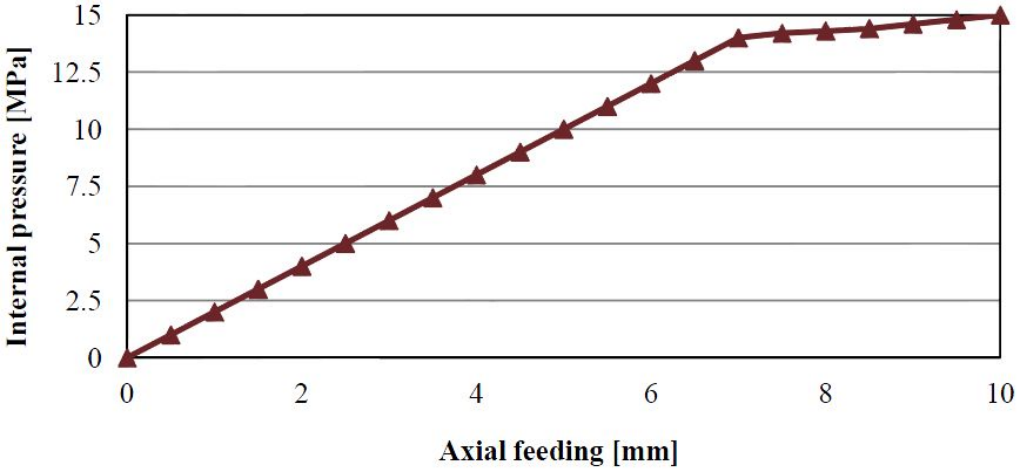

(b) Loading path B

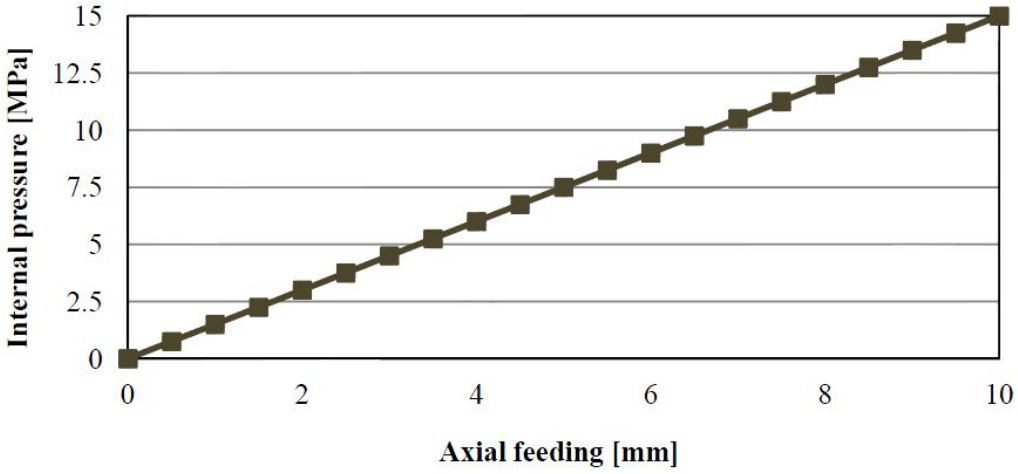

(c) Loading path C

Fig. 5.9 The three loading paths for THF experiments

The tubes were loaded and hydroformed under the above designated loading path until the fracture occurred. After that, the sealing condition was broken and the internal pressure disappeared. The related experimental results are introduced in Chapter 6.

Chapter 6 Results and Discussions

The results of present study are introduced and discussed in this chapter. The results consist of those outputs from three parts of works. The first part includes the basic material properties and the required damage parameters, which are used in the theoretical calculations and numerical simulations. The results of this parts are obtained from experiments and related data processing that have been introduced in Chapter 5. The second part includes the theoretical calculation result of the FLDs, which has been introduced in Chapter 3. The last part includes the simulated results which have been introduced in chapter 4. The relationships among them can be referred to the flow chart of the study as shown in Fig 2.1.

6.1 Material properties used in the criterion

The mechanical properties for the AA 6063 tubes obtained from uniaxial tensile test and uniaxial loading-unloading experiments include uniaxial stress-strain relation, elastic modulus E, yield stress σ_y, strain hardening rule, anisotropic plastic parameters R_0 R_{45} and R_{90}. The obtained material properties were used for the theoretical calculations and numerical simulations and to ensure their accuracies.

The engineering strain and stress data obtained from the uniaxial tensile test were output from the MTS 810 system, and then transformed into logarithmic strain ε and true stress σ respectively using equations (5.2) and (5.3). The $\varepsilon - \sigma$ relation of the AA 6063 tube is shown in Fig 6.1. From this curve, the yield stress and the Young's modulus is deduced as 210 MPa and 63.29 GPa, respectively.

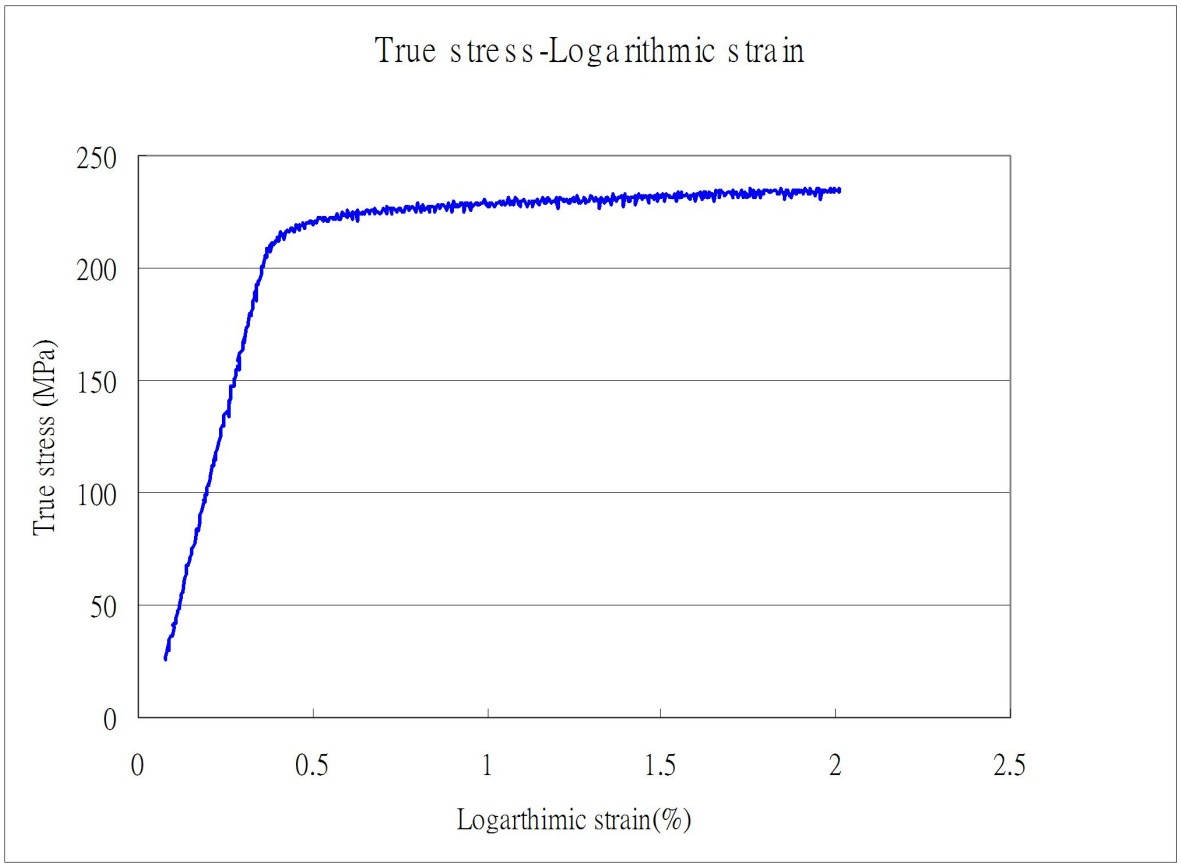

Fig 6.1 $\varepsilon - \sigma$ relation of AA 6063

The maximum strain could be estimated as 10% from the curve, it shows that the elongation property of the AA 6063 tubular material was lower about 30% than that of the AA 6063 sheet metal material (Karabay, Zeren and Yilmaz 2003). Some other tensile test works of as-received tubes and annealed tubes had also been done by other colleagues, which are shown in Fig 6.2.

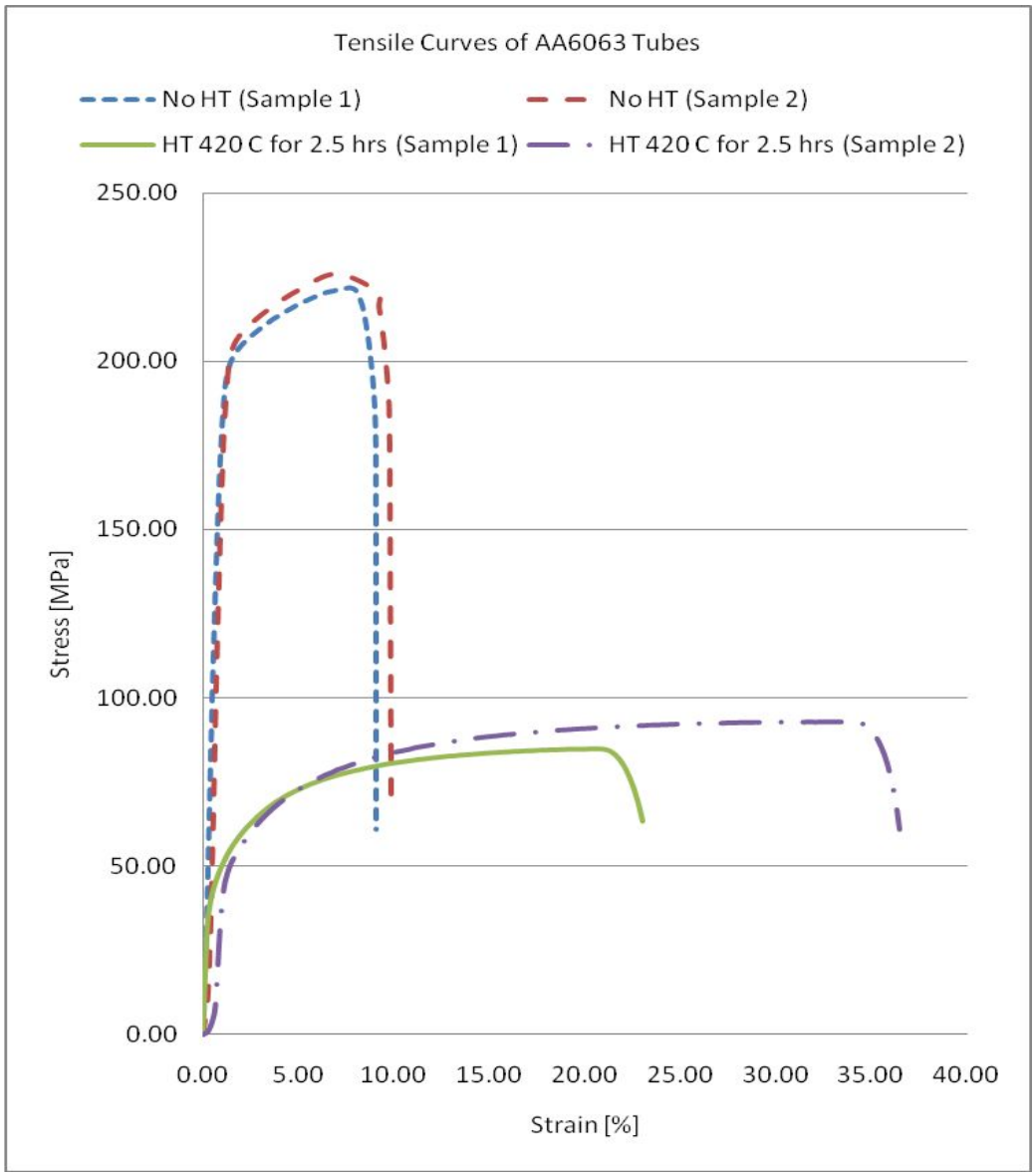

Fig 6.2 $\varepsilon - \sigma$ relations of as-received and heat treated AA 6063 tubes

The annealed condition was oxygen free one at about 420 °C for 2.5 hours. It indicates that annealing process can influence the AA 6063 tubes greatly on the yield stress, ultimate stress and elongation of the material. The yield stress of the annealed tubes decreased and below 100 MPa. On the other hand, the maximum strain increased significantly. Both of the engineering strains at the ultimate stress points of the annealed

tubes exceed 20%, which is 100% larger than those values tested from as-received tubes.

The plastic strain p and the strain hardening increment $T(p)$ were calculated using equation (5.4) and (5.5), respectively. The $T(p)-p$ relation is shown in Fig 6.3. The strain hardening rule was obtained from the regression of $T(p)-p$ data

$$T(p)=690(p+0.0021)^{0.14} \tag{6.1}$$

The obtained strain hardening rule is used to deduce the effective hardening modulus tensor $\overline{C}^{ep}$.

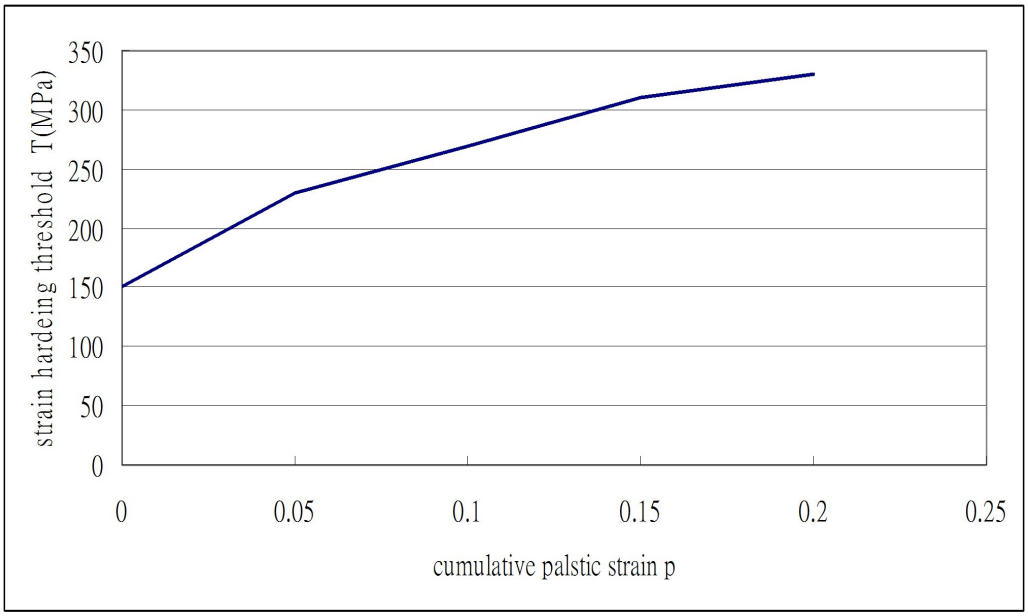

Fig. 6.3 $T(p)-p$ relation

The maximum strain obtained from Fig. 6.1 is used to set the pause points in the anisotropic parameter test and the loading-unloading experiments. As the maximum strain is no more than 10%, the pause points is set to be 0.3%, 2%, 4%, 6%, 8% and 10%. When above values displayed on the monitor of MTS 810, the machine was temporarily stopped manually. However, the actual pause point values may be little different from the set ones.

In the anisotropic test experiments, there were 5 points had been measured during experiments, the width of the specimen cut along circular direction is 2 mm, the thickness of it is 1.2mm. The measured width and thickness values are listed in Table 6.1, and then ε_2 and ε_3 defined in Chapter 5 at each pause points were calculated, with which the values of R_0 at pause points can also be further obtained, as shown in the table. As a result, the average value 0.91 is used to represent R_0 of the material.

Width w (mm)	1.920	1.905	1.895	1.885
ε_2	-0.0345	-0.0343	-0.0338	-0.0326
Thickness t (mm)	1.14	1.08	1.07	1.05
ε_3	-0.056	-0.063	-0.077	-0.0125

R_0	0.89	0.93	0.89	0.90

Table 6.1 Data from tensile test on the specimen taken along circular direction

Similarly, the anisotropic plasticity parameters along axial direction are calculated using the data measured from the tensile test specimens cutting along longitudinal direction. There are 5 points had been measured during experiment, the measured width and thickness values are listed in Table 6.2. The original width of the specimen for the tensile test is 5mm, the thickness is 1.2 mm, the average value 0.71 is used to represent R_{90} of the material.

Width w (mm)	4.985	4.961	4.943	4.827
ε_2	-0.0346	-0.0336	-0.0324	-0.0321
Thickness t (mm)	1.10	1.10	1.07	1.05
ε_3	-0.0351	-0.066	-0.087	-0.0118
R_{90}	0.69	0.70	0.68	0.71

Table 6.2 Data from tensile test on the specimen taken along axial direction

The anisotropic plasticity parameters along 45° from circular direction are calculated using the measured data from the specimens cut along that direction. There are 5 points which are measure during experiment, and the measured width and thickness values are listed in Table 6.3. The original width of the specimen is 2 mm, the thickness is 1.2 mm, the average value 0.87 was used to represent R_{45} of the material.

Width w (mm)	1.985	1.975	1.9625	1.957
ε_2	-0.056	-0.067	-0.076	-0.085
Thickness t (mm)	1.14	1.08	1.07	1.05
ε_3	-0.056	-0.063	-0.077	-0.0125
R_{45}	0.87	0.90	0.89	0.90

Table 6.3 Data from tensile test on the specimen taken along 45° from circular direction

The values of R_0, R_{45} and R_{90} are used to calculate the anisotropic parameters. The values of G, H, F, N are then obtained as 0.4386, 0.5614, 0.3018 and 3.4027, respectively.

6.2 Damage parameters used in the model establishment

The damage parameters are required to implement the theoretical calculations and the numerical simulations by which the material degradation could be taken into considerations. Damage rule and the related damage variables were brought from uniaxial loading-unloading experiment which has been introduced in Chapter 5.

The engineering strain and stress data were transformed into logarithmic strain and true stress in advance, with which the true stress strain curve from loading-unloading test was illustrated in Fig. 6.4. The data from unloading stages had fine linearity and the slopes of the unloading lines is decreased gradually accompany with the strain hardening. The Degradation of the material was identified through the decrease of the elastic modulus.

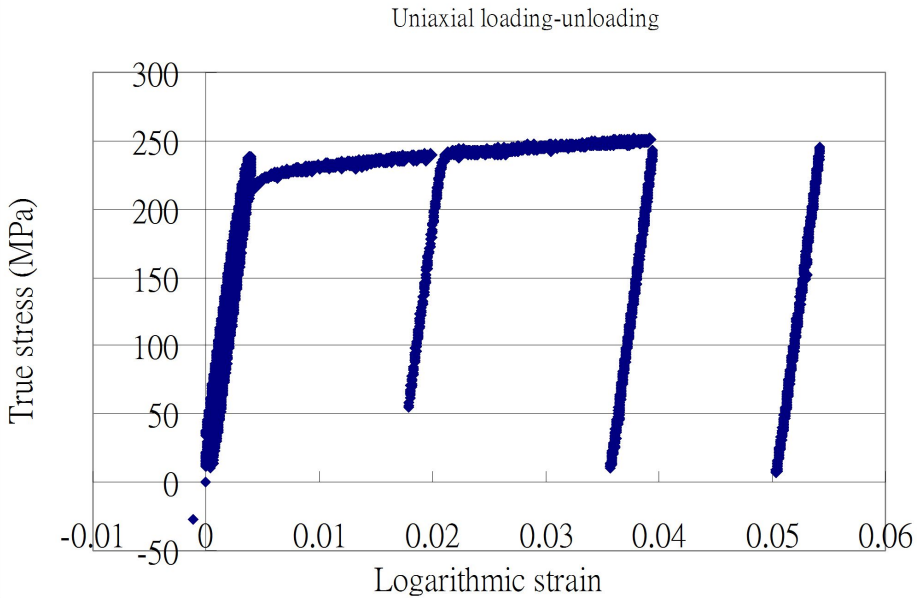

Fig. 6.4 $\varepsilon - \sigma$ relation from loading unloading experiment

There were three unloading paths as shown in Fig. 6.5, which were obtained from the experiment. The unloading pause points were set as same as those ones in the anisotropic tests. The effective Young's modulus is then derived from the slopes of the unloading lines.

Each unloading line is plotted in Fig. 6.5, the relation between the stress and strain are regressed from the slope lines and shown in the figure. The elastic modulus in each stage was obtained from coefficients of regression equations. An obvious decrease of the young's modulus could be detected among them. From Fig. 6.4 and Fig. 6.5, it can be found that the initial Young's mudulus value of the material is 63.29 GPa which is measured from the initial loading path of the elastic stage. The material was yield after

210 MPa, and strain hardening appeared after then. When the stress reaches 245 MPa, the Young's modulus measured from the unloading line becomes 61.69 GPa.

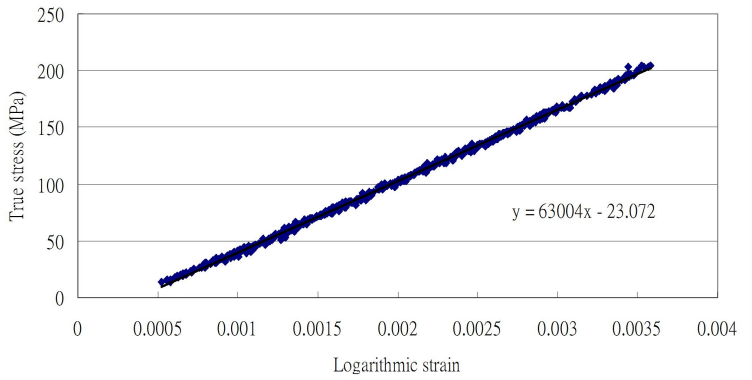

(a)

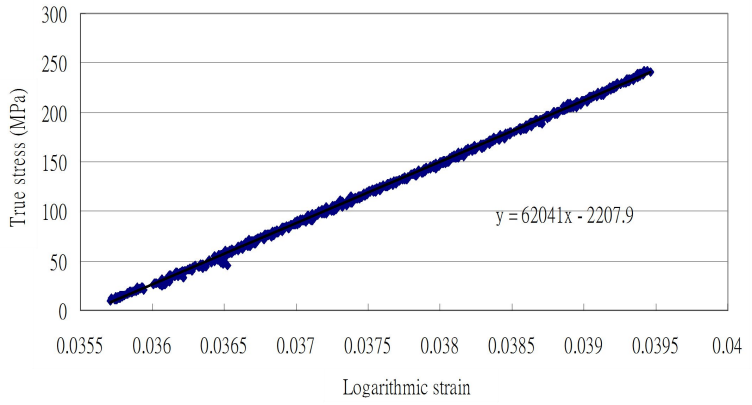

(b)

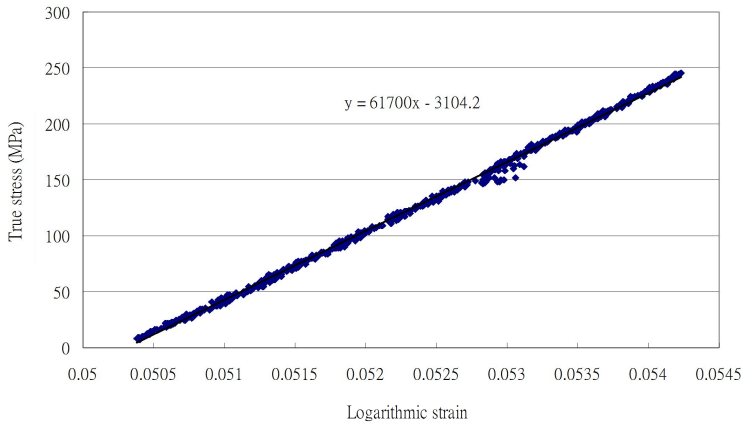

(c)

Fig. 6.5 True stress vs true strain of unloading paths

The damage parameters are calculated from the measured data in Fig. 6.5, as show in Table 6.4.

Strain (%)	Young's modulus (GPa)	D	Z	Y_{eq} (MPa)
0.3	63	0.057	0.082	0.81
4	62.04	0.064	0.091	1.15
6	61.69	0.062	0.093	1.42

Table 6.4 Damage parameters derived from the loading-unloading tensile test

From Fig. 6.5, it can be found that the effective Young's modulus varies during the loading process. In order to investigate the characteristic of the Young's modulus variation, relationships between the effective Young's modulus and stress/strain are studied.

The loading process of the material could be illustrated by using the $\sigma - \varepsilon$ curve. For strain hardening material such as AA 6063 tubes, the stress value would increase after the material yields. So the increased yield stress could be an index to identify the loading progress.

Three pause points are selected in the experiment. The effective Young's modulus measured from the unloading slope lines starting at these 3 pause points are related to damage variables and can be used to represent the corresponding damage degrees.

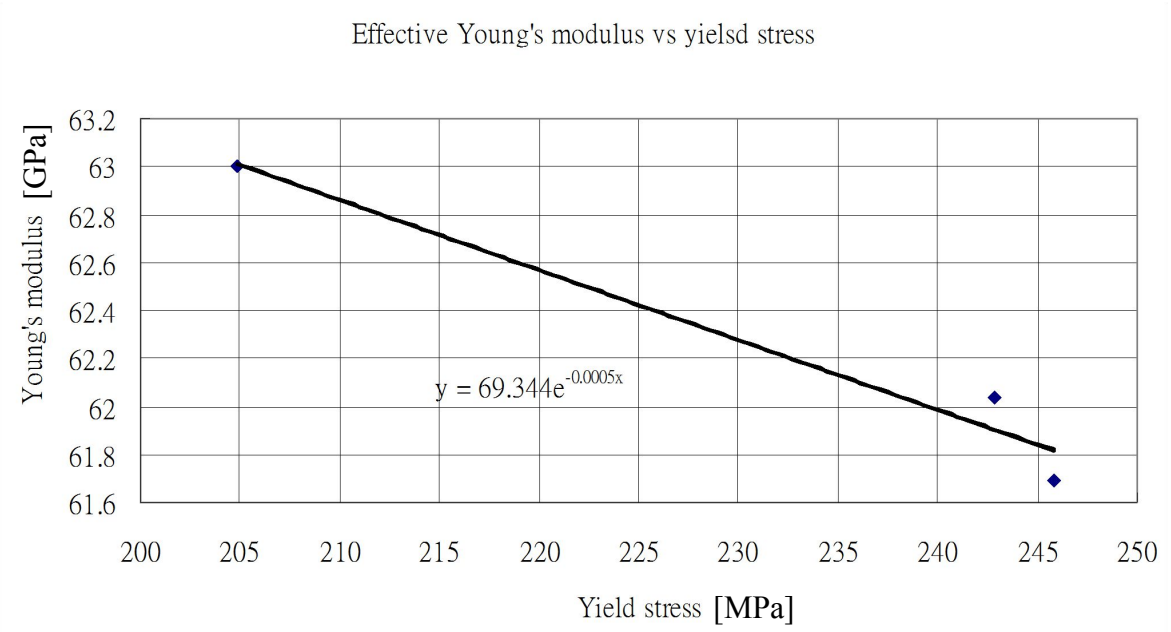

Fig. 6.6 $\overline{E}-\sigma$ curve of AA 6063

The effective Young's modulus values deduced from the unloading paths and the yield stress values at the start points of the each loading paths are plotted in Fig. 6.6, the effective modulus is decreased when the yield stress increased. A negative correlation can be observed from the plot, which is regressed using an exponential function

$$\overline{E} = 69.344e^{-0.0005\sigma'} \times 10^9 \tag{6.2}$$

Where $\sigma' = \sigma \times 10^{-6}$

The obtained relation between the effective Young's modulus and the yield stress could be used only before the ultimate stress was reached. After the ultimate stress achieved, the $\sigma - \varepsilon$ curve shown a decline trend and the yield stress decreased. However, after the material being damaged, the damage cannot be released based on irreversible thermodynamics theory.

In basic physical view, when the plastic strain increases the geometric size of defects inside the material should also increase; this will influence the elastic properties and can be identified by the variations of Young's modulus.

Another relationship is studied between effective Young's modulus and strain. When the material is strengthened by loading, the plastic strain always becomes larger than before. Even when the material was strain softening, the plastic deformation would also increase when the yield stress decreased. Thus, ε_p can be a label of the loading progress in a larger loading range. When the elastic strain is neglected, the total strain ε can be used to represent ε_p

The $\overline{E}-\varepsilon$ relation is shown in Fig. 6.7(b), where ε is measured at pause points. The effective Young's modulus decreased when the ε increased. The relationship between them is regressed from the measured data as follows:

$$\overline{E} = 63.093e^{-0.4183\varepsilon} \times 10^9 \tag{6.3}$$

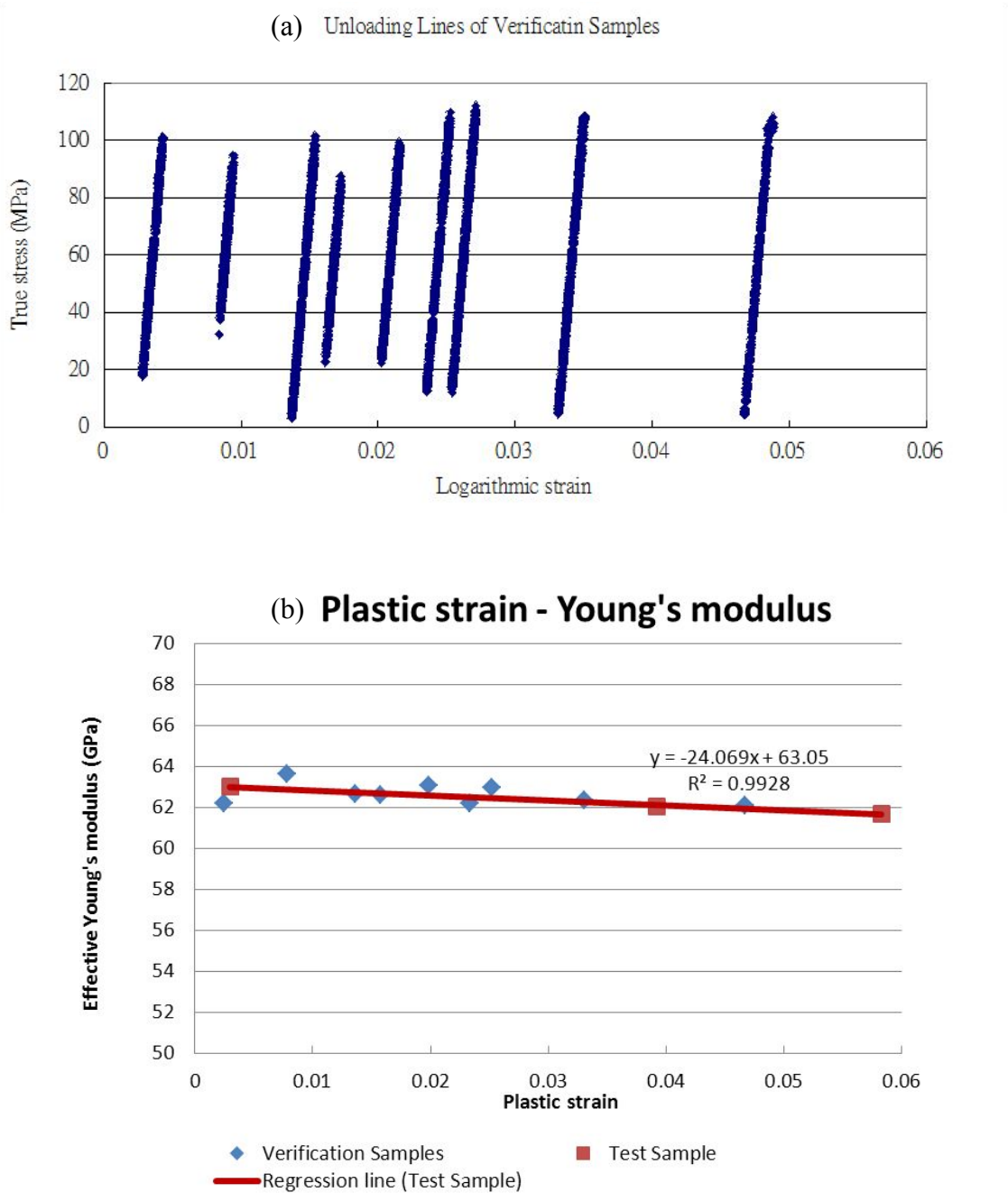

Fig 6.7 $\overline{E} - \varepsilon$ curve of AA 6063 tubes

The initial plastic damage strengthening threshold is calculated by using equation (5.16) as:

$C_0 = 450.041\,\text{MPa}$

Above value is larger than those values of the other aluminum alloys such as 293.19 MPa in Al 6022-T4, which has be calculated using the parameters in the published article (Chow and Jie 2004).

In order to validate the reliability of damage parameters, further verification using loading-unloading tests was carried out. The unloading lines obtained from the tests are shown in Fig. 6.7 (a). These unloading lines could be used to illustrate varied effective Young's moduli in different unloading stages. The plastic strain and the effective Young's model were calculated from these unloading lines accordingly, as shown in Fig. 6.7(b). The relationship between plastic strain and effective Young's modulus was estimated based on the calculated results from the previous loading-unloading tests.

It was shown that points obtained from the verification samples were distributed around the regression line (Fig. 6.7(b)), which validated that the proposed damage parameters did agree with the damage parameters in those verification samples.

From equation (6.2), the stress can be expressed using equivalent damage such that

$$\sigma_1 = 4.99\times10^{10} - 2\times10^{9}\ln\left[(1-\frac{\sqrt{2}}{2}Z)^3 E\right] \tag{6.4}$$

The damage parameters can be obtained using equation (5.23) as follows:

$$C(Z) = \frac{2}{E(\sqrt{2}-Z)^3}\left\{4.99\times10^{10} - 2\times10^{9}\ln\left[(1-\frac{\sqrt{2}}{2}Z)^3 E\right]\right\}^2 - C_0 \tag{6.5}$$

6.3 Comparison between predicted FLDs results and experimental FLDs results

The experimental data of FLDs were derived from experiments introduced in Section 5.3.3. In the experiments the AA6063 tubes with printed grids were bulged and fractured. The deformation regions of the tubes were divided into three regions: the safety region, the marginal localized necking region and the fracture region. The shape and size of the grids on different regions are different. Strain in these regions was determined from calculation on grids deformation. The length of major axis and minor axis on the selected grids were measured under microscope, as illustrated in Fig. 6.8. The engineering strain was calculated using the measured axis lengths and then transformed to the true strain.

Fig 6.8 Microscope used in the FLDs test

The fractured tube is shown in Fig 6.9, it is central symmetric with a bulged dome in the middle part. The fracture points locate at the top of the dome along the axial direction, as shown in the amplified region in the figure. Because the stress state and the strain distribution were axial symmetric, the deformation along circular direction should be the same when ignoring the non-homogenization of material. The localized necking point should initiate at the weakness point among the region located at the top of the bulging dome.

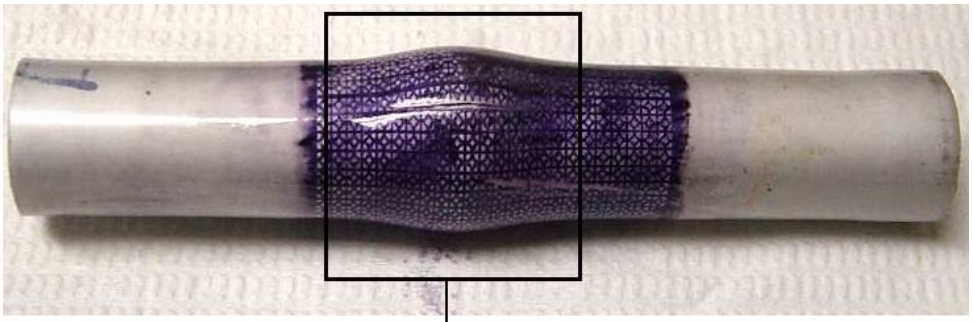

(a)

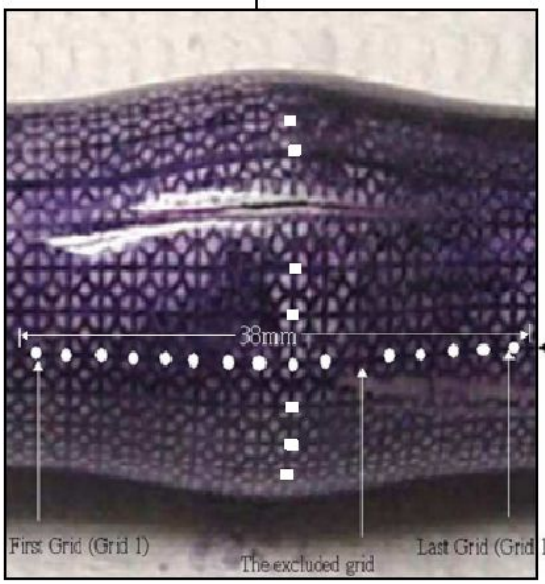

(b)

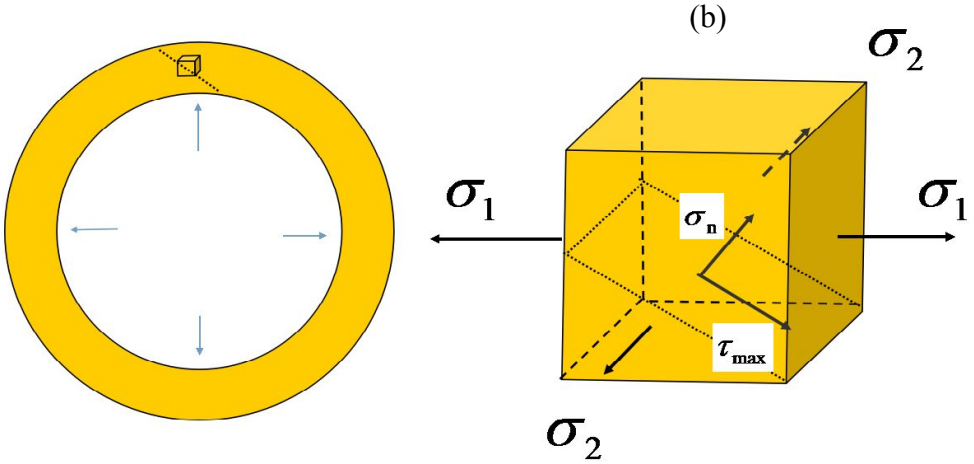

(c)

Fig, 6.9 Test point of FLDs

An element in the cross section of the bulged tube was enlarged, as shown in Fig. 6.9 (c)

The major stress of the element was the hoop/tensile stress σ_1 that was created by the

internal pressure. The minor stress σ_2 created by the feed in force should be along the axial direction. Both normal stress σ_n and shear stress τ existed in any cross section inside the element. The maximum shear stress τ_{max} was assumed to exist in the plane shown by dotted lines in the element. When the maximum stress in this plane reached the shear criterion, the slip/shear band that occurred along this plane in the element and localized necking should have been on the wall of the tube (BRESSAN and WILLIAMS 1983). Equation (3.23) shows that the angle between directions of major stress σ_1 and the maximum shear stress τ_{max} was determined by the strain ratio. Equation (3.25) showed that the maximum shear stress was determined by its direction and σ_1. This did explain why the shear criterion was still used to predict the material failure.

The grids along the circular direction at the top of the bulging dome were chosen as the marginal localized necking points. Two localized circular grids could be identified near the fracture. The remained regions are taken as safety regions. In the present study, grid region along an axial are chosen to represent the safety region. The grids with white dots are measured, as shown in Fig. 6.9. It should also be noted that some of the grids had been destroyed in the experiment due to friction or oil pollution. The FLDs measured from the selected marginal grids are shown in Table 6.5.

No.	Minor strain	Major strain
1	0.339325	0.424614
2	0.303063	0.429182
3	0.29788	0.434376
4	0.310422	0.426574
5	0.307485	0.421338
6	0.352767	0.429182
7	0.34146	0.431133
8	0.288182	0.435671
9	0.318454	0.442761
10	0.319907	0.449801

Table 6.5 Limit strain measured from tube hydroformed components

The predicted theoretical FLD of AA 6063 was calculated based on damage coupled shear criterion, using the self-developed FORTRAN program introduced in Section 3.3.

The material parameters and the damage parameters including the hardening law, the damage law, the Young's modulus, yield stress and the anisotropic plasticity parameters, etc., have been incorporated into the FORTRAN program.

Both of the limit strain in Table 6.5 and the predicted FLDs are plotted in Fig. 6.10. It can be found that the distribution of the measured strain values are all located in the RHS region, which means deformation of bulging tubes in the hydroforming process is mainly a biaxial tensile deformation. Meanwhile the strain ratios of the measured limit strain values are quite close 1, which is corresponding to equal biaxial stretch. In order to obtain wider distribution of limit strain values, some loading path had been tried during the experiment. However, the results are unsatisfied. When the axial force had been added in the experiment with which more material can be feed into the die cavity to get smaller minor strains, wrinkling occurred and thus no limit strain can be obtained from the specimen. It also shows that the loading path influences the hydroforming results significantly.

The predicted FLDs were located at the area with strain ratio β range from -0.5 to 1. In the LHS area, the limit major strains are larger than the value of critical plane strain.

In the RHS area, limit strain curve takes the shape of a descend line starting from the point of plane strain state. The predicted FLDs were well correlated with the FLDs obtained from the tube hydroforming experiment.

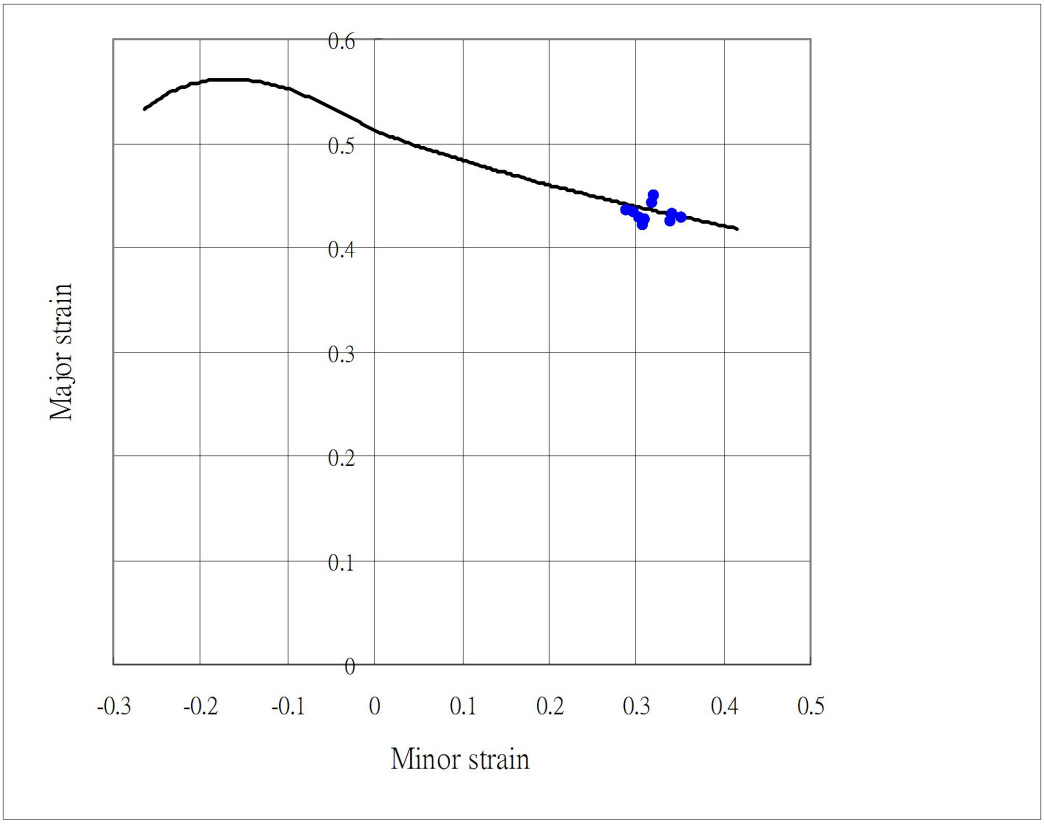

Fig 6.10 The comparison between tested limit strain and theoretical prediction of FLDs for AA 6063

A forming limit curve is usually calculated by using the FLD criterion and constructed in the forming limit strain distribution diagram. The main validation method is to assess

the agreement between the forming limit curve and the forming limit diagram. As the failure of the tube occurred in hydroforming was not so easy to predict by using other criteria and verified with related facilities for its non-proportional loading path. Obviously, other criteria were not used or compared at this time due to an insufficient duration of study. Therefore, the error percentages of using different criteria have not been achieved by using other widely acceptable methods at the moment.

As the tested FLDs are all located in the RHS, the predicted results can not be validated in the LHS in the FLDs. In order to validate the prediction result of the proposed criterion in the LHS, more comparisons have been conducted. Here, two forming limit data of AA 6063-T4 and AA 6063-W which have obtained from published article (Adam R. 2007) are used to compare with the predicted FLDs. The limit strain data of AA 6063-T4 and AA 6063-W are shown in Tables 6.6 and 6.7, respectively.

No.	Minor strain	Major strain
1	0.21129	0.275862
2	0.195161	0.248276
3	0.180645	0.282759
4	0.182258	0.303448
5	0.135484	0.255172
6	0.140323	0.275862
7	0.053226	0.313793
8	0.053226	0.293103
9	0.012903	0.377586
10	0.014516	0.374138
11	-0.02903	0.358621
12	-0.12903	0.45
13	-0.15161	0.301724
14	-0.30323	0.346552
15	-0.48871	0.403448
16	-0.44677	0.406897
17	-0.47903	0.365517
18	-0.45645	0.313793
19	-0.42419	0.305172
20	-0.44355	0.175862
21	-0.48548	0.267241
22	-0.17742	0.431034
23	-0.18871	0.431034

Table 6.6 Limit strain of Al 6063-T4

No.	Minor strain	Major strain
1	0.032258	0.25
2	0.01129	0.232759
3	0.016129	0.274138
4	0.003226	0.303448
5	0.014516	0.315517
6	-0.03065	0.301724
7	-0.06452	0.389655
8	-0.0871	0.372414
9	-0.08548	0.368966
10	-0.09677	0.424138
11	-0.14516	0.415517
12	-0.17742	0.382759
13	-0.17742	0.381034
14	-0.17581	0.556897
15	-0.19194	0.42931
16	-0.42419	0.336207
17	-0.45	0.32931
18	-0.48871	0.356897
19	-0.45	0.377586
20	-0.46935	0.151724
21	-0.48871	0.139655
22	-0.09032	0.568966
23	0.077419	0.531034
24	0.174194	0.531034
25	0.219355	0.493103
26	0.170968	0.481034
27	0.203226	0.42931
28	0.324194	0.42931
29	0.15	0.387931

Table 6.7 Limit strain of Al 6063-W

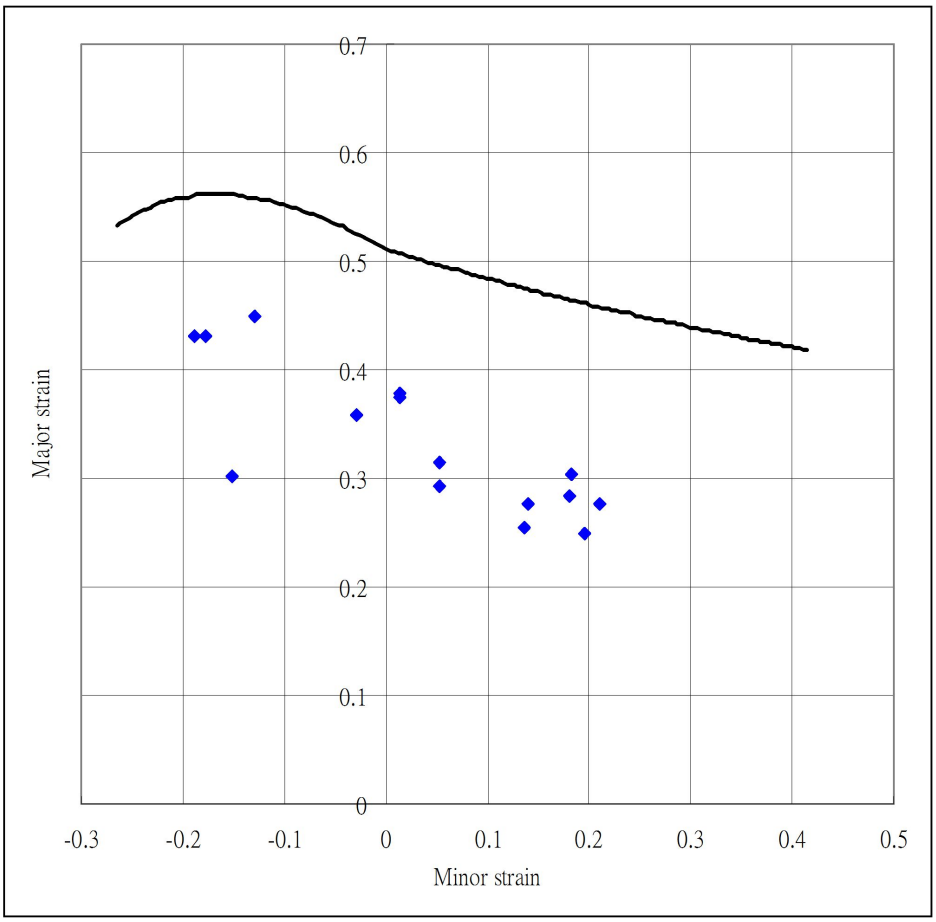

Fig 6.11 Comparison of AA 6063-T4

The experimental forming limit strain of AA 6063-T4 (Adam R. 2007) and the predicted FLDs are plotted in Fig. 6.11. The distribution of limit strains is accordance to the shape of the predicted FLDs curve. The limit strains obtained from experiments are all below the predicted FLDs. It shows that the predicted criterion is larger than the localized necking strains of AA 6063-T4. The damage coupled shear criterion may be only a rough standard to estimate the maximum limit strains of AA 6063-T4 sheets before designing sheet forming process. It cannot be used to determine the loading condition as well as to design the process and components accurately.

The experimental forming limit strain of AA 6063-W (Adam R. 2007) and the predicted forming limit strain are plotted in Fig 6.12. The predicted FLDs go through the experimental FLDs in both RHS and LHS areas, it shows that the damage coupled shear criterion is suitable for predicting the forming limit of AA 6063-W. It should be noted that more forming limit strain points are located under the predicted FLDs curve, this means that the proposed criterion may still overestimate the forming limit for AA 6063-W components.

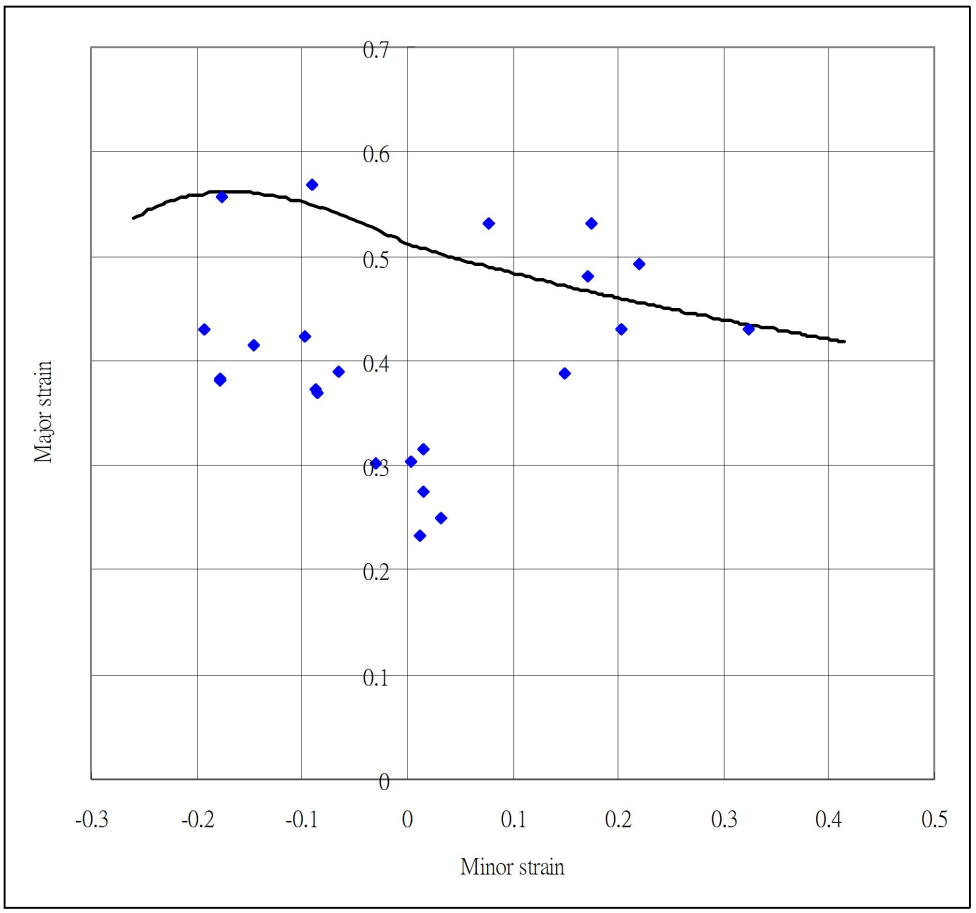

Fig. 6.12 Comparison of AA 6063-W

In most of these comparisons, the FLDs predicted by damage coupled shear criterion is higher or equal to the experimental limit strain especially when compared with experimental AA 6063-T4 data. It can be concluded that the proposed criterion can be used to determine an upper bound of forming limit of AA 6063.

The proposed forming limit curve was acceptable when it was compared with experimental results of AA 6063-W, but was higher than that of AA 6063-T4 results. The main reasons for the differences between the prediction result and experimental results were:

(a) The damage parameters used in the prediction were obtained from the tests carried out using AA 6063 tube. The damage evolutions of AA 6063-T4 and AA 6063-W (studied by others) were not the same as the damage evolution of our AA 6063 tube, so their damage parameters were different. The experimental results for AA 6063-T4 were lower than the predicted FLC. The findings showed that the damage evolution of AA 6063-T4 made the material deteriorate more rapidly than in the case of the AA 6063 tube.

(b) The mechanical properties used in the prediction were obtained from the AA 6063 tube. The properties of AA 6063-T4 and AA 6063-W were different from the AA 6063

tube. As the material properties used in the prediction were based mainly on our acquired values of the AA 6063 tube, the prediction results were hence quite different from the experimental results.

(c) The FLD data of AA 6063-T4 and AA 6063-W were investigated through the use of their sheet materials. The FLD data from sheet materials were somehow different from the FLD observed from tubes. The material properties used in the prediction were obtained from tubular materials, while the FLD data were acquired from sheet materials, thus the prediction results were unable to be in good agreement.

In order to get more accurate predicted results, the material properties of those tubular AA 6063-T4 and AA 6063-W materials should be obtained again and re-determined.

Meanwhile new loading-unloading tests should also be conducted on these two materials to obtain more accurate damage evolutions of AA 6063-T4 and AA 6063-W.

6.4 Comparison between simulation and experimental results of THF components

In this section, the hydroformed tubes in the experiment introduced in section 5.3 are compared with the simulation results which have been introduced in chapter 4. The loading condition set in the simulation is similar to those in the experiments. The corresponding results are compared with each other.

The simulated results and the experiment results by using loading path A-C is shown in Fig. 6.13-15, respectively. The localized necking areas are located at the central part of tubes as marked in the Figures. The experiment results include two kinds of situation: localized necking or bursting. If the loading in the experiment paused just at the initiation point of localized necking, a localized necking region appeared. If the loading is continued after then, bursting will occur. The results show that the largest stress point exists at the middle of the tube. The major strain direction of the tube during the hydroforming process was in the hoop direction.

The results obtained under loading path A is shown in Fig. 6.13. In the loading path A, a comparable larger internal pressure is provided to the tubes with a little axial feeding. There is a localized necking region observed from experimental result. The necking

region located in the central part along the axial direction with a length about 5mm. The damage value at the stop point of the simulation process is 0.176.

The results obtained under loading path B is shown in Fig. 6.14. With the loading path B, a bursting can be found in both experimental result and simulated result. The busting point is also located in the central part along the axial direction. The damage value at the stop point of the simulation process is 0.193.

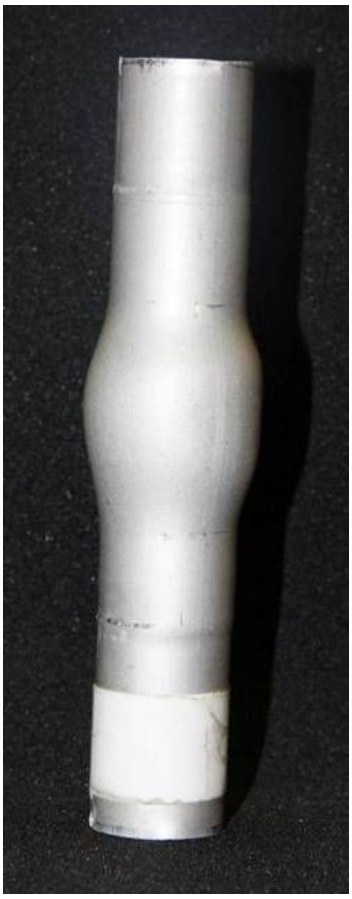

Experiment
(a)

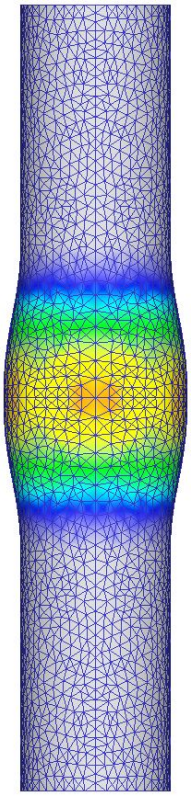

Simulation
(b)

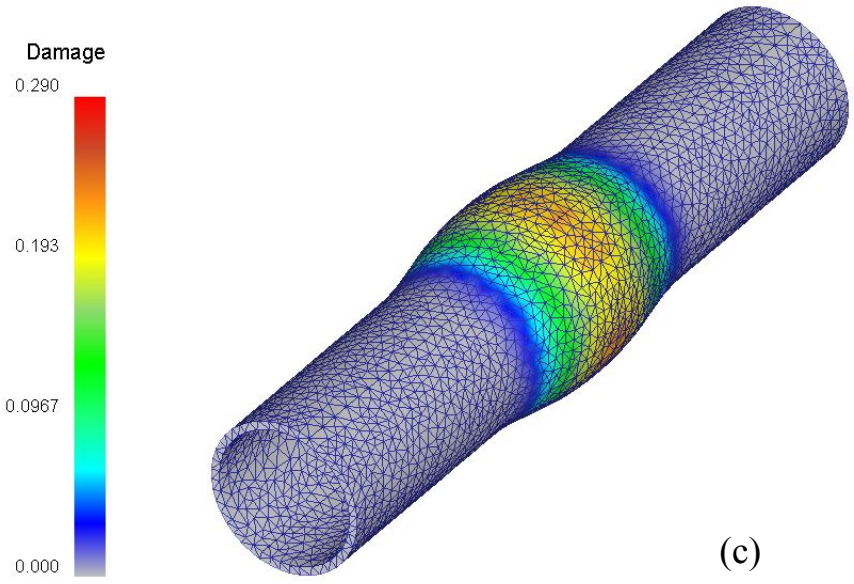

(c)

Fig 6.13 failure tubular component in hydroforming process on loading path A

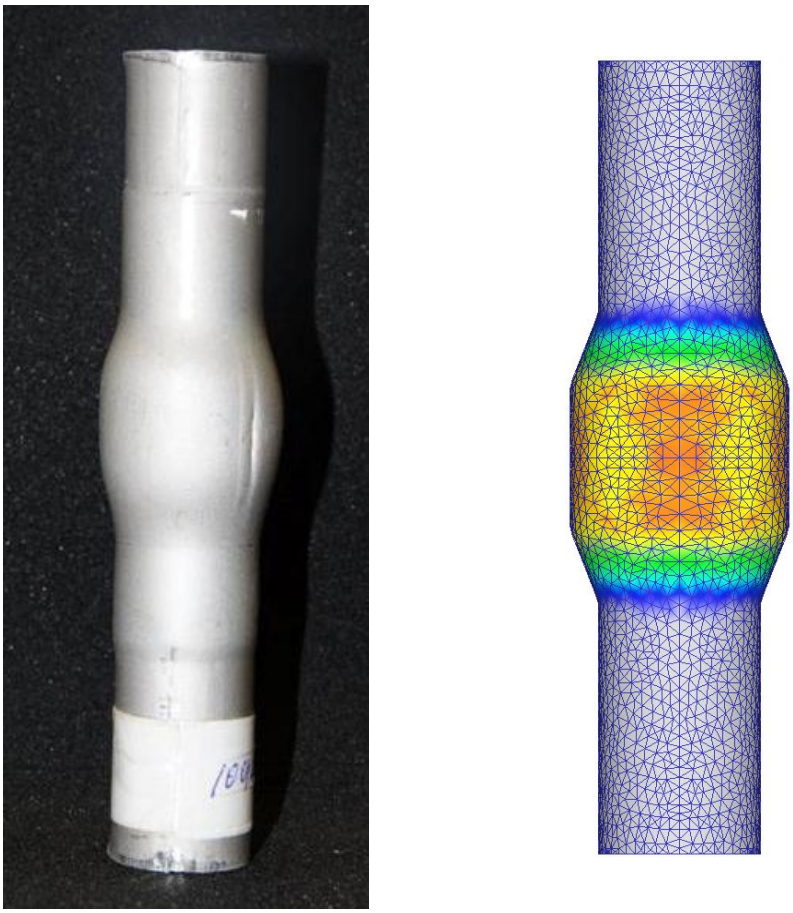

Experiment (a)

Simulation (b)

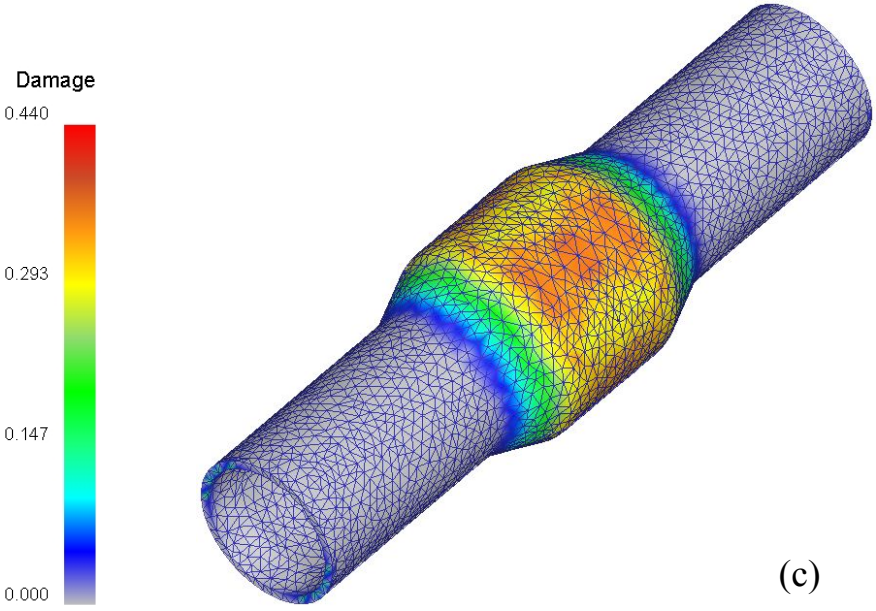

(c)

Fig 6.14 failure tubular component in hydroforming process on loading path B

Another loading path is also used in the simulation, whose result is shown in Fig. 6.15. The similar shape can be found from the comparison. Meanwhile deformation on the central part is bigger than those ones in the Fig. 6.13 and Fig 6.14, which shown that the axial feeding can elevate the endurance stress on the components. Bursting phenomena can be found in both of the experimental results and the simulated result. The busting point is also located in the central region along the axial direction. The damage value at the stop point of the simulation process is 0.384.

The fracture point of the simulated results and the hydroformed results from experiments are all located at the middle region of the tubes where the largest deformation occurred. The fracture is along axial direction, which means that the hoop direction is the major loading direction. The maximum damage value from the simulated result is about 0.3 which indicate that the AA 6063 tubes may be not failure even the damage of the material is far below the value of 1.

Experiment (a)

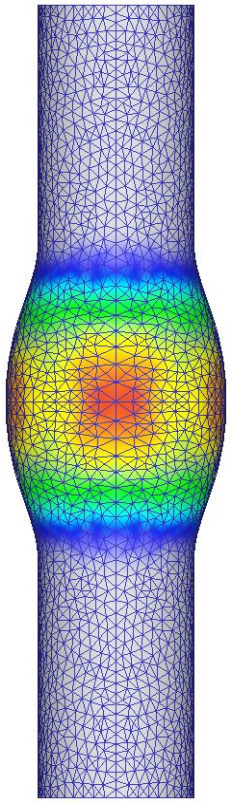

Simulation (b)

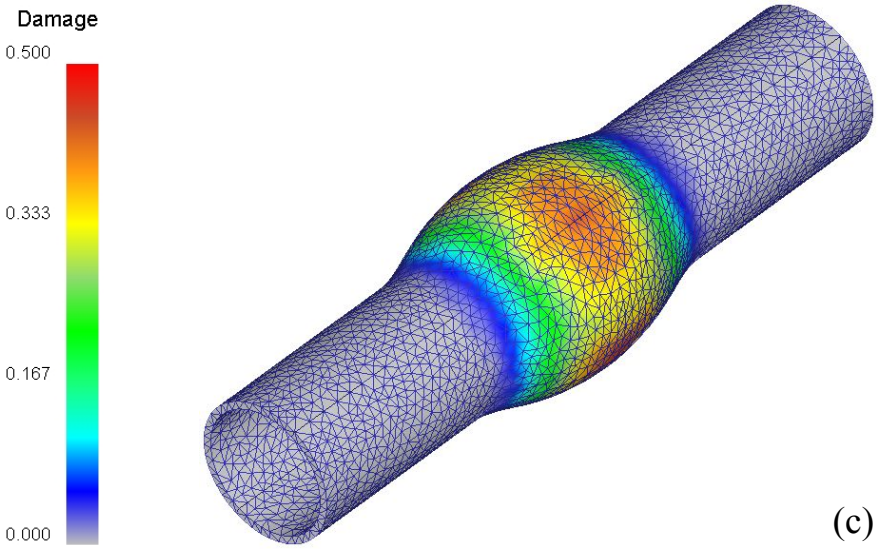

(c)

Fig. 6.15 Failure tubular component in hydroforming process on loading path C

The maximum diameters of the fractured tubes at their domes are 24 mm, 27mm and 34mm in path A, B and C respectively. The specimen hydroformed with loading path C which is has the largest elongation ratio in hoop direction. The maximum diameter is 7 mm larger than that of the tubes from loading path A. It is illustrated that the formability can be improved with the axial feeding. The more material driven to the die cavity, the thinning of the tubes can be compensated by the feeding material

The fracture of tubes are all initiated and extended along the axial direction. The maximum damage values are also located on the top of the tube and along axial direction. The consistency shows that the criterion and the constitution used in the present study is reasonable and effective in describing the mechanical property of AA 6063 tubes in hydroforming process.

Meanwhile the damage values at the localized necking points are varied from 0.15 to 0.40. The damage value in loading path A is the smallest, on the contrary, the biggest value is found in loading path C. The maximum damage value in the tube when localized necking occurs is nearly 0.4, it means that the degradation of tubes from part C is more serious than that of tubes from loading path A. It can be found that less axial feeding leads to a smaller failure damage value. The less axial feeding displacement

drives less material to compensate the thinning of the tube walls, and the material thickness will become thinning in a larger ratio. The stress in the major strain direction will also increase in a larger ratio. As the proposed criterion is a combination failure condition consisting all the stress, strain ratio and damage parameters, therefore, when the stress and strain ratio is changed, the damage value on the forming limit is changed correspondingly.

Some other factors will also influence the simulation results such as friction, lubrication, et al. The optimized set values used in the simulation should be further investigated in the future with which the accuracy of the simulation can be developed.

Chapter 7 Conclusions and Future works

7.1 Conclusions

In this study, a damage coupled shear criterion has been presented to predict the localized necking of aluminum AA 6063 tubes in hydroforming process. The shear criterion (BW Criterion) has been extended to be capable of predicting both the LHS and the RHS of the FLDs in the strain diagram based on zero extension assumption. The shear failure criterion is induced without the assumption of proportional loading path which leads it to be available in the research of varies engineering sheet metal processes without limitation of proportional loading. As tubular components processed in hydroforming process usually endured complicated loading path, the proposed criterion is suitable in studying practical engineering problem of it, such as determination of the deformation range, design of loading parameter and the selection of material.

Degradation is assumed to exist in AA 6063 tubes during hydroforming process which is usually termed as damage. In order to take the damage into consideration, an anisotropic damage theory has been coupled into the extended shear failure criterion. The damage coupled shear failure criterion has been deduced for determining forming limit strain of AA 6063 tubes in the hydroforming process. Varies defects exist in the

AA6063 tubes, they generally initiate in different produce stages. When take damage into consideration, the influences of these defects on the material property can be valued with which relate formability prediction can be more reliable

Material properties for the AA 6063 tube were deduced from the data obtained from uniaxial tensile test. The Young's modulus and the yield stress of AA 6063 were 210 MPa and 63.29 GPa, respectively. The experiment data were fitted by a power curve. The strain hardening law and the constant of component *n* are deduced as:

$$T(p) = 690(p + 0.0021)^{0.14}.$$

Anisotropic plasticity parameters are obtained from the uniaxial tensile test with the pause points. The parameters are derived from the plastic deformation appeared in the width direction and the thickness direction. The value of R_0 , R_{45} and R_{90} is 0.91, 0.81, and 0.71, respectively. From these values, the anisotropic parameters are obtained. G, H, F and N is 0.4386, 0.5614, 0.3018 and 3.4027, respectively. Damage parameters of AA 6063 tubes are tested using loading-unloading experiment. Damage variables are calculated from the variation of Young's modulus. An effective Young's modulus-yield stress relation has regressed from the experimental data,

$$\overline{E} = 63.093e^{-0.4183\varepsilon} \times 10^9$$

Taking strain as the identification of the material loading stage, effective Young's modulus-strain relation is obtained

$$\overline{E} = 63.093e^{-0.4183\varepsilon} \times 10^9$$

A new analytical method is proposed to obtain the damage evolution rule of the material as follows

$$C(Z) = \frac{2}{E(\sqrt{2}-Z)^3}\left\{4.99\times10^{10} - 2\times10^9 \ln\left[(1-\frac{\sqrt{2}}{2}Z)^3 E\right]\right\}^2 - C_0$$

Formability of AA 6063 has been tested from tube hydroforming process. The forming limit values of the tube are measured with the deformed circular grid system after hydroforming. The obtained results provide a solid assistant for the hydroforming tooling and process design. AA 6063 tube hydroforming have been conducted using 3 loading paths, all the fractures in these experiments are located at the top of the bulging dome areas. The maximum diameters of the hydroformed parts are 24 mm, 27 mm and 34 mm, respectively. The material properties and damage parameters observed in the present study can be used as references in related academic research and engineering works on AA6063 tubes.

FROTRAN program has been coded to calculate the FLDs using damage coupled shear criterion. The FLDs of AA 6063 tube has been computed based on damage coupled shear criterion by using the tested material properties derived from the test and damage

parameters. FEM numerical simulation has been conducted to simulate the localized necking and fracture of tubes in the hydroforming process. A user-defined material subroutine has been developed. The failure definition in the subroutine is the proposed damage coupled shear criterion. The material properties and damage rules of AA 6063 tubes have been incorporated into the subroutine. The new developed criterion is embedded into the commercial finite element code ABAQUS through its subroutine interface. Axisymmetric bulging experiments have been simulated using the software package with the developed subroutine. Three different loading paths as the same as those in the bulging experiments are used in the simulation. The developed program can be used in calculating FLC of other materials when incorporating related parameters of material property. The stress update subroutine also can be embedded in other programs to express the anisotropic damage constitutive relationship.

Three kinds of experimental FLDs had been compared with the computed FLDs. The experimental FLDs include FLDs of AA 6063 tube which has been measured by ourselves and the published FLDs data of AA 6063-T4 and AA 6063-W (Adam R. 2007). The comparison results shown that the proposed forming limit criterion is considerable satisfied with the experimental results of AA 6063 and AA 6063-W tubes. However, the values of the predicted forming limit strain may be overestimated when

using the proposed shear criterion to predict AA 6063-T4. The comparisons between experimental FLDs and computed FLDs show that the damage coupled shear criterion can be used to estimate the limit strain of the hydroforming products before designing tube hydroforming process and related components. Simulated results obtained from FEM software package have also been compared with the real hydroforming components that have be obtained with three different loading paths. The fracture or localized necking points of the simulated results locate at the same region as those ones from hydroformed components. The results of validation for predicted FLDs indicate that the proposed failure criterion is reliable in forming limit prediction and can be an effective assistance in related process design.

The main contribution of the study include the following:

First, the study has contributed a significant improvement in the use of the shear criterion to predict FLD in both right hand and left hand xx.

Second, the study took the shear criterion into consideration in relation to damage evolution for quantitative failure analysis.

7.2 Future works

In order to improve the criterion, following works are suggested to be conducted in the future.

The key issue in using the shear criterion is to determine the critical shear stress of the material. The critical shear stress as a material constant is difficult to be measured from experiments. The initially method was proposed by Bressan and Williams (Bressan and Williams 1983), who suggested to deduce the critical shear stress from uniaxial tensile test or biaxial tests. The alternative method was proposed by Alsos (Alsos et al. 2008) and our research group, which was to calibrate the criterion at the plane strain state condition, however, it was only be effective in using different criteria for LHS and RHS. Some more advanced technical effort might be performed to determine the values using tensile test.

The ultimate purpose of the proposed study is to introduce it into tube hydroforming applications. As more complex loading paths exist in the engineering, the theory should be validated for various kinds of loading conditions. More simulation works should be done on hydroforming process with un-proportional loading paths, complex die set and

different metal materials. More factors such as lubrication, loading rate should also be studied in the simulation on their influences.

Warm hydroforming of aluminum alloy and other light metals can provide many advantages compared with the conventional hydroforming process. In order to extend the criterion to the warm hydroforming process, the material properties and the damage parameters should be precisely determined at the elevated temperatures. The thermal coupled constitution of the material should be studied based on certain experimental conditions. The reasonable technology of strain measurement, width and thickness calibration in the heating conditions should also be studied.

References

Aydemir A., de Vree J.H.P., Brekelmans W.A.M., Geers M.G.D., Sillekens W.H., Werkhoven R. (2005). An adaptive simulation approach designed for tube hydroforming processes, J. Mater. Process. Tech., 159 (3), pp. 303 – 310

Kulkarni A., Biswas P., Narasimhan R., Luo A.A., Mishra R.K., Stoughton T.B. Sachdev A.K.(2004). An experimental and numerical study of necking initiation in aluminium alloy tubes during hydroforming, Int. J. Mech. Sci., 46 (12), pp. 1727 – 1746

Adam R., G. S. a. M. I. (2007). Optimizationi of material properties and process parameters for tube hydroforming of aluminum extrusion. Journal of Engineering Materials and Technology-Transactions of the Asme, 129, 233-241.

Alsos, H. S., O. S. Hopperstad, R. Toernqvist & J. Amdahl (2008). Analytical and numerical analysis of sheet metal instability using a stress based criterion. International Journal of Solids and Structures, 45, 2042-2055.

Altan, T., T. Sokolowski, K. Gerke & M. Ahmetoglu (2000). Evaluation of tube formability and material characteristics: hydraulic bulge testing of tubes. Journal of Materials Processing Technology, 98, 34-40.

Asnafi, N. & A. Skogsgårdh (2000). Theoretical and experimental analysis of stroke-controlled tube hydroforming. Materials Science and Engineering: A, 279, 95-110.

Barata Da Rocha, A. (1989). Theoretical Forming Limit Diagrams of Anisotropic Sheets:Linear and Non-linear Strain Paths, In: Wagoner, R.H., Chan, K.S. and Keeler, S.P.(eds), pp. 183 – 202, Forming Limit Diagrams: Concepts, Methods and Applications,Warrendale, PA, USA.

Barata Da Rocha, A., Barlat, F. and Jalinier, J.M. (1985). Prediction of the Forming LimitDiagrams of Anisotropic Sheets in Linear and Non-linear Loading, Mat. Sci. Engr., 68:151 – 164.

Beaudoin, A.J., Koya, T., Smith, P.E. and Wiese, J.W. (1995). Experiences in the Use of anEvolutionary Damage Model with LS-DYNA3D, SAE Tech. Paper No. 950915.

Bigoni, D. and Zaccaria, D. (1994). On the Eigenvalues of the Acoustic Tensor in Elastoplasticity, Eur. J. Mech., A/Solids, 13: 621 – 638.

Borre, G. and Maier, G. (1989). On Linear Versus Nonlinear Flow Rules in Strain LocalizationAnalysis, Meccanica, 24: 36 – 41.

Benallal, A. & C. Comi (1996). Localization analysis via a geometrical method. International Journal of Solids and Structures, 33, 99-119.

Bontcheva, N. (1994). Plastic Localization in Anisotropically Hardening Damaged Materials. European Journal of Mechanics a-Solids, 13, 751-761.

Bourget, J. P., M. Fafard, H. R. Shakeri & T. Côté (2009). Optimization of heat treatment in cold-drawn 6063 aluminium tubes. Journal of Materials Processing Technology, 209, 5035-5041.

Bressan, J. D. & J. A. Williams (1983). The Use of a Shear Instability Criterion to Predict Local Necking in Sheet-Metal Deformation. International Journal of Mechanical Sciences, 25, 155-168.

Chaboche, J.L. (1989). Constitutive equations for cyclic plasticity and cyclic viscoplasticity, Int. J. Plasticity.5, 247–302.

Chan, L.C., Cheng, C.H., Jie, M. and Chow, C.L. (2005). Damage Based Formability Analysis for TWBs, Int. J. Damage Mech., 14: 83 – 96.

Considere (1885). Ann Ponts et Chaussees, 9, 574.

Chan, L. C., J. Lin & L. Wang (2010). Prediction of forming limit diagrams based on shear failure criterion. International Journal of Solids and Structures, 47, 2855-2865.

Chen, X.F. and Chow, C.L. (1995). On Damage Strain Energy Release Rate Y, Int. J. Damage Mech., 4: 251 – 263.

Chow, C. L. & M. Jie (2004). Forming limits of AL 6022 sheets with material damage consideration - theory and experimental validation. International Journal of Mechanical Sciences, 46, 99-122.

Chow, C. L. & X. J. Yang (2002). Bursting for fixed tubular and restrained hydroforming. Journal of Materials Processing Technology, 130, 107-114.

Chow, C. L. a. L., T.J. (1989). On Evolution Laws of Anisotropic Damage. Eng. Fract Mech., 34, 679–701.

Chow, C.L., Yu, L.G. and Demeri, M.Y. (1996). Prediction of Forming Limit Diagram with Damage Analysis, SAE Tech. Paper No. 960598.

Chow, C.L., Yu, L.G. and Demeri, M.Y. (1997). A Unified Damage Approach for Predicting Forming Limit Diagrams, J. Eng. Mater. Tech., 119: 346 – 353.

Chow, C.L., Yu, L.G., Rai, W.H. and Demeri, M.Y. (2001a). Prediction of Forming Limit Diagrams for AL6111-T4 Under Non-proportional Loading, Int. J. Mech. Sci., 43:471 – 486.

Dutkiewicz, J. & L. Litynska (2002). The effect of plastic deformation on structure and properties of chosen 6000 series aluminium alloys. Materials Science and Engineering: A, 324, 239-243.

Corona E. (2004) A simple analysis for bend-stretch forming of aluminum extrusions, Int. J. Mech. Sci., 46 (2004), pp. 433 – 448

Lin F.C., Kwan C.T. (2004). Application of abductive network and FEM to predict an acceptable product on T-shape tube hydroforming process, Comput. Struct., 82 (15 – 16), pp. 1189 – 1200

Gemeamer, M. (1946). Strength and Ductility. Trans. ASM.

Goodwin, G. M. (1968). Application of strain analysis to sheet metal forming problems in press shop. SAE paper, No. 680093.

Graf, A. & W. Hosford (1993). Effect of Changing Strain Paths on Forming Limit Diagrams of Al 2008-T4. Metallurgical Transactions a-Physical Metallurgy and Materials Science, 24, 2503-2512.

Guan, Y., F. Pourboghrat and W.-R. Yu (2006). "Fourier series based finite element analysis of tube hydroforming - An axisymmetric model." Engineering Computations 23(7-8): 697-728.

Hill, R. (1952). On discontinuous plastic states with special reference to localized necking in thin sheets. journal of the mechanics and physcs of solids, 1, 19-30.

Hill, R. (2001). On the mechanics of localized necking in anisotropic sheet metals. Journal of the Mechanics and Physics of Solids, 49, 2055-2070.

Hosford, W.F. (1979). On Yield Loci of Anisotropic Cubic Metals, In: 7th North Amer. Metalworking Res. Conf. Proc., SME, Dearborn, MI.

Hosford, W.F. and Duncan, J.L. (1999). Sheet Metal Forming: A Review, JOM, 51(11): 39 – 44.

Hu, J., Jonas, J.J., Zhou, Y. and Ishikawa, T. (1998). Influence of Damage and TextureEvolution on Limit Strain in Biaxially Stretched Aluminum Alloy Sheets, Mater. Sci.Eng., A251: 243 – 250.

Huang, T. and Li, G.C. (1996). Numerical Analyses for the Material Bifurcation in Plane SheetUnder Tension, Eng. Fract. Mech., 55: 223 – 234.

Hult, J. (1979). Continuum Damage Mechanics – Capabilities Limitations and Promises, In:Mechanics of Deformation and Fracture, Pergamon, Oxford, pp. 233 – 347.

Kim J., Kang B.S., Choi H.H. (2002). Numerical analysis and design for tube hydroforming process by rigid-plastic finite element method, Trans. NAMRI/SME, 30, pp. 127 – 134

Kim J., Kang S.J., Kang B.S. (2003). A prediction of bursting failure in tube hydroforming processes based on ductile fracture criterion, Int. J. Adv. Manuf. Technol., 22 (5 – 6), pp. 357 – 362

Kim J., Kang B.S., Hwang S.M., Park H.J. (2004). Numerical prediction of bursting failure in tube hydroforming by the FEM considering plastic anisotropy, J. Mater. Process. Tech., 153 – 54 (Special Issue Part 1), pp. 544 – 549

Kim J., Kang B.S. (2004). Analytical approach to bursting failure prediction in tube hydroforming based on plastic instability, Adv. Eng. Plast. Appl., Parts 1 and 2—Key Eng. Mater., 274 – 276, pp. 601 – 606

Yoon J.W., Chung K., Pourboghrat F., Barlat F. (2006). Design optimization of extruded preform for hydroforming processes based on ideal forming design theory, Int. J. Mech. Sci., 48, pp. 1416 – 1428

Johnson K.I., Nguyen B.N., Davies R.W., Grant G.J., Khaleel M.A. (2004). Numerical process control method for circular-tube hydroforming prediction, Int. J. Plasticity, 20 (6), pp. 1111 – 1137

Fann K.J., Hsiao P.Y. (2003). Optimization of loading conditions for tube hydroforming, J. Mater. Process. Tech., pp. 520 – 524

Kang, B. S., S. J. Kang & H. K. Kim (2005). Tube size effect on hydroforming formability. Journal of Materials Processing Technology, 160, 24-33.

Kang, Y., Wang, X., Kihara, J. and Aizawa, T. (1990). Construction of the Forming Limit Diagram on the Basis of the Surface and Internal Damage of Sheet Metal. Adv. Tech. Plast, 3, 1251-1256.

Keeler (1965). Determination of forming limits in automotive stampings. Sheet Metal Forming Technology, 42, 683-691.

Keeler, S. P. (1963). Application of Strain Analysis on Sheet Metal Forming Problems in The Press Shop. Trans. ASM., 25.

Keeler, S. P. (1968). Circular grid system - A valuable aid for evaluating sheet metal formability. SAE Technical Paper, No. 680092.

Keigler, M., H. Bauer, D. Harrison & A. K. M. De Silva (2005). Enhancing the formability of aluminium components via temperature controlled hydroforming. Journal of Materials Processing Technology, 167, 363-370.

Kim, S. & Y. Kim (2002). Analytical study for tube hydroforming. Journal of Materials Processing Technology, 128, 232-239.

Koc, B. C. (1999). Development of design guidelines for part, tooling and process in the tube hydroforming technology.

Koc, M. & T. Altan (2001). An overall review of the tube hydroforming (THF) technology. Journal of Materials Processing Technology, 108, 384-393.

Koc, M. & T. Altan (2002). Prediction of forming limits and parameters in the tube hydroforming process. International Journal of Machine Tools & Manufacture, 42, 123-138.

Kulkarni, A., P. Biswas, R. Narasimhan, A. A. Luo, R. K. Mishra, T. B. Stoughton & A. K. Sachdev (2004). An experimental and numerical study of necking initiation in aluminium alloy tubes during hydroforming. International Journal of Mechanical Sciences, 46, 1727-1746.

Wu L., Yu Y.(1996) Computer Simulations of Forming Automotive Structural Parts by Hydroforming Process 3rd International Conference: Numerical Simulation of 3D Sheet Metal Forming Processes — Verification of Simulations with Experiments, Dearborn, Michigan, pp. 324 – 329

Lang, L. H., Wang Z.R., Kang D.C., Yuan S.J., Zhang S.H., J. Danckert & K. B. Nielsen (2004a). Hydroforming highlights: sheet hydroforming and tube hydroforming. Journal of Materials Processing Technology, 151, 165-177.

Lang, L. H., S. J. Yuan, X. S. Wang, Z. R. Wang, Z. Fu, J. Danckert & K. B. Nielsen (2004b). A study on numerical simulation of hydroforming of aluminum alloy tube. Journal of Materials Processing Technology, 146, 377-388.

Lang, L. H., S. J. Yuan, Z. R. Wang, X. S. Wang, J. Danckert & K. B. Nielsen (2004c). Experimental and numerical investigation into useful wrinkling during aluminium alloy internal high-pressure forming. Proceedings of the Institution of Mechanical Engineers Part B-Journal of Engineering Manufacture, 218, 43-49.

Lee, S., Y. H. Chen & J. Y. Wang (2002). Isothermal sheet formability of magnesium alloy AZ31 and AZ61. Journal of Materials Processing Technology, 124, 19-24.

Lemaitre, J. and J.L. Chaboche (1990). Mechanics of Solids Materials, Cambridge University Press.

Lemaitre, J., Desmorat R, Sauzay, M. (2000). Anisotropic damage law of evolution. Eur, J. Mech. Solids, 19, 187-208.

Liu, S.D., Mueleman, D., Thompson, K.(1998). Analytical and experimental examination of tubular hydroforming limits. SAE Technical Paper #980449, pp. 139 – 150.

Lu, Z.-H. (1994). Instability analysis in sheet metal forming processes. PhD thesis Ann Arbor, Mich. U.M.I.

M. Imaninejad, G. Subhash, A. Loukus (2004). Influence of end-conditions during tube hydroforming of aluminum extrusions, Int. J. Mech. Sci., 46 (8), pp. 1195 – 1212

Marciniak, Z. a. K., K. (1967). Limit strains in the processes of stretch-forming sheet metal. International Journal of Mechanical Sciences, 9, 609–620

Ray P., Mac Donald B.J. (2004).Determination of the optimal load path for tube hydroforming processes using a fuzzy load control algorithm and finite element analysis, Finite Elements Anal. Des., 41 (2), pp. 173 – 192

Painter, M. J. a. P., R. (1974). J. Phys. D: Appl, Phys., 992.

Peng, K. (1985). The plastic instability and forming limits of AK steel sheets. Sheet Metal Industries, July, 390-392.

Peng, K., Tan, H. and Guo, Z. (1987). Some new results in experimental study of FLD. Sheet Metal Industries, 28-29.

Hsu Q.C. (2003). Theoretical and experimental study on the hydroforming of bifurcation tube, J. Mater. Process. Tech., 142 (2), pp. 367 – 373

Ray, P. & Mac Donald B.J. (2005). Experimental study and finite element analysis of simple X- and T-branch tube hydroforming processes. International Journal of Mechanical Sciences, 47, 1498-1518.

Kaya S., Gorospe I., Altan T. (2002). Preforming and expansion of an aluminum alloy in tube hydroforming — comparison of FEA predictions with existing experimental data. Trans. NAMRI/SME, 30, pp. 119 – 126

Srinivasan, T.M., Shaw, J.R., Thompson, K. (1998). Tubular hydroforming: correlation of experimental and simulation results. SAE Technical Paper #980448, pp. 131 – 137.

Schreyer, H. L. & M. K. Neilsen (1996). Discontinuous bifurcation states for associated smooth elasticity and damage with isotropic elasticity. International Journal of Solids and Structures, 33, 3239-3256.

Subhash, G., M. Imaninejad & A. Loukus (2005). Loading path optimization of tube hydroforming process. International Journal of Machine Tools & Manufacture, 45, 1504-1514.

Swift, H. W. (1952). Plastic Instability under Plane Stress. Journal of the Mechanics and Physics of Solids, 1, 1-18.

Hama T., Asakawa M., Makinouchi A. (2004). Investigation of factors which cause breakage during the hydroforming of an automotive part, J. Mater. Process. Tech., 150 (1 – 2), pp. 10 – 17

Hama T., Asakawa M., Fukiharu H., Makinouchi A. (2004b). Simulation of hammering hydroforming by static explicit FEM, Iron Steel Institute Japan, 44 (1), pp. 123 – 128

Hama T., Asakawa M., Fuchizawa S., Makinouchi A. (2003). Analysis of hydrostatic tube bulging with cylindrical die using static explicit FEM, Mater. Trans., 44 (5), pp. 940 – 945

Papelnjak T. (2004). Numerical analyses of tube hydroforming by high internal pressure, Strojniski Vestnik-J. Mech. Eng., 50 (1), pp. 31 – 43

Vukota, B. (2004). Sheet metal forming processes and die's design. ISBN: 0-8311-3182-9

Xia, Z. C. (2001). Failure analysis of tubular hydroforming. Journal of Engineering Materials and Technology-Transactions of the Asme, 123, 423-429.

Aue-U-Lan Y., Ngaile G., Altan T. (2004). Optimizing tube hydroforming using process simulation and experimental verification, J. Mater. Process. Tech., 146 (1), pp. 137 – 143

Hwang Y.M., Altan T. (2004). Process fusion: tube hydroforming and crushing in a square die, J. Eng. Manuf., 218 (2), pp. 169 – 174

Hwang Y.M., Altan T. (2003). Finite element analysis of tube hydroforming processes in a rectangular die, Finite Element Anal. Des., 39 (11), pp. 1071 – 1082

Marciniak Z., Duncan J.L., Hu S.J. (2002). Mechanics of sheet metal forming. ISBN: 978-0-7506-5300-8

Appendix: Subroutine of $\overline{\boldsymbol{C}}^{ep}$

The main part of the VUMAT subroutine is the derivation of $\overline{\boldsymbol{C}}^{ep}$, the FORTRAN code of it is as follows:

```
subroutine cepMatrix(dcdz, alfa,nu, F,G,H,N,D1,D2,zero, ezero,dtdp,
mu,strainInc1,strainInc2,strainInc4, s
igeqbar,csig1,csig2,csig3,cep,beta,mre,are)
!******************************************** !
! declaration part
!******************************************** !
implicit none
! declare the variable used in the main program
real :: nu, F,G,H,N,D1,D2,D3,zero, ezero,dtdp, mu
real :: deld1,deld2,strainInc1,strainInc2,strainInc4,m, sigeqbar
real :: psig1,psig2,psig3,sig1,sig2,sig3
!*********************************************
! declare the variable used in the subroutine
real, dimension(3,3):: mre
real, dimension(3,3)::III, cep, II, are, deld, cepbar, one, ce, cere
real, dimension(3,3)::dmddt1,dmddt2,dmddt3, ii1,ii2,ii3,ii4,dfddy
real, dimension(3,3)::a, dfddyt, dyddt, matrixI, dfddsigt,sig,alfa1,alfa2,alfa3
real alfa, beta, dcdz, cefactor, IIIfactor,III1,III2,III3, yeq, y1, y2, y3,csig1,csig2,csig3,i,j
!******************************************** !
! subroutine program part
!*************************************************************************
! calculate matrix cep
sig1=csig1
sig2=csig2

sig3=csig3

! obtain ce
cefactor=ezero/(1-nu**2)
```

```
ce(1,1)=cefactor
ce(2,2)=cefactor
ce(3,3)=cefactor*(1-nu)/2
ce(1,2)=cefactor*nu
ce(2,1)=cefactor*nu
ce(1,3)=0
ce(3,1)=0
ce(2,3)=0
ce(3,2)=0
! obtain III
! obtain sieqbar from main program
IIIfactor=(ezero**2)/(4*sigeqbar**2*(1-nu**2)**2)
sig1=csig1
sig2=csig2
sig3=csig3
III1=(G+H)*sig1/(1-D1)+nu*(F+H)*sig2/(1-D2)-H*(sig2/(1-D2)+nu*sig1/(1-D1))
III2=nu*(G+H)*sig1/(1-D1)+(F+H)*sig2/(1-D2)-H*(nu*sig2/(1-D2)+sig1/(1-D1))
III3=N*(1-nu)*sig3/((1-D1)*(1-D2))**0.5
III(1,1)= IIIfactor*III1**2
III(2,2)= IIIfactor*III2**2
III(3,3)= IIIfactor*III3**2
III(1,2)= IIIfactor*III1*III2
III(2,1)= IIIfactor*III1*III2
III(1,3)= IIIfactor*III1*III3
III(3,1)= IIIfactor*III1*III3
III(2,3)= IIIfactor*III2*III3
III(3,2)= IIIfactor*III2*III3
! obtain beta from subroutine pInc
psig1=csig1
psig2=csig2
psig3=csig3
call pInc(sigeqbar,nu,
F,G,H,N,D1,D2,psig1,psig2,psig3,ezero,dtdp,beta,strainInc1,strainInc2,strainInc4,
beta)
! obtain cep
cep=ce-beta*III
! calculate matrix II
! obtain mre
mre(1,1)=1-D1
```

```
mre(2,2)=1-D2
mre(3,3)=((1-D1)*(1-D2))**0.5
mre(1,2)=0
mre(2,1)=0
mre(1,3)=0
mre(3,1)=0
mre(2,3)=0
mre(3,2)=0

! obtain dfddy

y1=-((1-d2)*sig1**2-mu*(1-d1)*sig1*sig2+(1+mu)*(1-d1)*sig3**2)/(ezero*(1-d2)*(1-d1)**3)
y2=(mu*(1-d2)*sig1*sig2-(1-d1)*sig2**2-(1+mu)*(1-d2)*sig3**2)/(ezero*(1-d1)*(1-d2)**3)
y3=-(((1-d2)*sig1+(1-d1)*sig2)*sig3)/(ezero*(1-d2)**2*(1-d1)**3)
yeq=((y1**2+y2**2)/2+mu*y1*y2+(1-mu)*y3**2)**0.5
dfddy(1,1)=(y1+mu*y2)/(2*yeq)
dfddy(2,1)=(y2+mu*y1)/(2*yeq)
dfddy(3,1)=(2*y3*(1-mu))/(2*yeq)
! obtain cere
cere(1,1)=1/ezero
cere(2,2)=1/ezero
cere(3,3)=-nu/ezero
cere(1,2)=-nu/ezero
cere(2,1)=2*(1+nu)/ezero
cere(1,3)=0
cere(3,1)=0
cere(2,3)=0
cere(3,2)=0
! define dmddt
do i=1,3
do j=1,3
dmddt1(i,j)=0
dmddt2(i,j)=0
dmddt3(i,j)=0
end do
end do
dmddt1(1,1)=1/(1-D1)**2
dmddt1(3,3)=1/((2*(1-D1)**1.5)*((1-D2)**0.5))
dmddt3(2,2)=1/(1-D2)**2
dmddt3(3,3)=1/((2*(1-D1)**0.5)*((1-D2)**1.5))
```

```
dmddt3(1,3)=1/((1-D1)*(1-D2))
dmddt3(3,2)=1/((2*(1-D1)**0.5)*((1-D2)**1.5))
ii1=matmul(matmul(matmul(cep,mre),dmddt1),dfddy)
ii2=matmul(matmul(matmul(cep,mre),dmddt2),dfddy)
ii3=matmul(matmul(matmul(cep,mre),dmddt3),dfddy)
do i=1,3
do j=1,3
ii4(i,j)=0
end do
end do
ii4(1,1)=ii1(1,1)
ii4(2,1)=ii1(2,1)
ii4(3,1)=ii1(3,1)
ii4(1,2)=ii1(1,1)
ii4(2,2)=ii1(2,1)
ii4(3,2)=ii1(3,1)
ii4(1,3)=ii1(1,1)
ii4(2,3)=ii1(2,1)

ii4(3,3)=ii1(3,1)

II=-matmul(ii4,cere)
! calculate matrix A**(-1)
! define one
do i=1,3
do j=1,3
one(i,j)=0
end do
end do
one(1,1)=1
one(2,2)=1
one(3,3)=1
dfddyt(1,1)=(y1+mu*y2)/(2*yeq)
dfddyt(1,2)=(y2+mu*y1)/(2*yeq)
dfddyt(1,3)=(2*y3*(1-mu))/(2*yeq)
dyddt(1,1)=-(3*(1-D2)*sig1**2-2*nu*(1-D1)*sig1*sig2+2*(1-nu)*(1-D1)*sig3**2)/(ezero*(1-D1)*
**4*(1-D2))
dyddt(1,2)=(nu*sig1*sig2-(1+nu)*sig3**2)/(ezero*(1-D1)**2*(1-D2)**2)
dyddt(1,3)=-sig3*(2*sig1*(1-D2)+sig2*(1-D1))/(ezero*(1-D1)**3*(1-D2)**2)
dyddt(2,1)=(nu*sig1*sig2-(1+nu)*sig3**2)/(ezero*(1-D1)**2*(1-D2)**2)
```

```
dyddt(2,2)=-(3*(1-D2)*sig1**2-2*nu*(1-D1)*sig1*sig2+2*(1-nu)*(1-D1)*sig3**2)/(ezero*(1-D1)*(
1-D2)**4)
dyddt(2,3)=-sig3*(sig1*(1-D2)+2*sig2*(1-D1))/(ezero*(1-D1)**2*(1-D2)**3)
dyddt(3,1)=-sig3*(2*sig1*(1-D2)+sig2*(1-D1))/(ezero*(1-D1)**3*(1-D2)**2)
dyddt(3,2)=-sig3*(sig1*(1-D2)+2*sig2*(1-D1))/(ezero*(1-D1)**2*(1-D2)**3)
dyddt(3,3)=-(sig1**2*(1-D2)+sig1*sig2*(1-nu)*(1-D1)*(1-D2)+(1-D1)*(sig2**2*(1-D1)+(3+nu)*(
1-D2)*sig3**2))
/(2*ezero*(1-D1)**3*(1-D2)**3)
alfa1=matmul(matmul(dfddyt,dyddt),dfddy)
! calculate alfa
alfa=1/(dcdz+alfa1(1,1))
matrixI(1,1)=(-1/yeq)*(y1+mu*y2)/(1-D1)
matrixI(2,2)=(-1/yeq)*(y2+mu*y1)/(1-D2)
matrixI(3,3)=(-1/yeq)*(y2+mu*y1)/(2*(1-D2))
matrixI(1,3)=(-1/yeq)*2*y3*(1-mu)/((1-D1)**0.5*(1-D2)**0.5)
matrixI(3,1)=(-1/yeq)*y3*(1-mu)/((1-D1)**0.5*(1-D2)**0.5)
matrixI(3,2)=(-1/yeq)*y3*(1-mu)/((1-D1)**0.5*(1-D2)**0.5)
do i=1,3
do j=1,3
sig(i,j)=0
end do
end do
sig(1,1)=sig1
sig(2,1)=sig2
sig(3,1)=sig3

do i=1,3

do j=1,3
dfddsigt(i,j)=0
end do
end do
sig(1,1)=sig1
sig(1,2)=sig2
sig(1,3)=sig3
!**********matrix a
a=one+alfa*matmul(matmul((matrixI+II),sig),dfddsigt)
!**********reverse matrix a
L=1
```

```
n=3

DO 100 K=1,N
D=0.0
DO 10 I=K,N
DO 10 J=K,N
IF (ABS(A(I,J)).GT.D) THEN
D=ABS(A(I,J))
IS(K)=I
JS(K)=J
END IF
10 CONTINUE
IF (D+1.0.EQ.1.0) THEN
L=0
WRITE(*,20)
END IF
20 FORMAT(1X,'ERR**NOT INV')
DO 30 J=1,N
T=A(K,J)
A(K,J)=A(IS(K),J)
A(IS(K),J)=T
30 CONTINUE
DO 40 I=1,N
T=A(I,K)
A(I,K)=A(I,JS(K))
A(I,JS(K))=T
40 CONTINUE
A(K,K)=1/A(K,K)
DO 50 J=1,N
IF (J.NE.K) THEN
A(K,J)=A(K,J)*A(K,K)
END IF
50 CONTINUE
DO 70 I=1,N
IF (I.NE.K) THEN
DO 60 J=1,N
IF (J.NE.K) THEN
A(I,J)=A(I,J)-A(I,K)*A(K,J)
END IF
```

```
60 CONTINUE
END IF
70 CONTINUE
DO 80 I=1,N
IF (I.NE.K) THEN
A(I,K)=-A(I,K)*A(K,K)
END IF
80 CONTINUE
100 CONTINUE
DO 130 K=N,1,-1
DO 110 J=1,N
T=A(K,J)
A(K,J)=A(JS(K),J)
A(JS(K),J)=T
110 CONTINUE
DO 120 I=1,N
T=A(I,K)
A(I,K)=A(I,IS(K))
A(I,IS(K))=T
120 CONTINUE
130 CONTINUE

are=a

END
```